Ensovibep, a novel trispecific DARPin candidate that protects against SARS-CoV-2 variants

Sylvia Rothenberger[1,2,*], Daniel L. Hurdiss[4,5,*], Marcel Walser[3,*], Francesca Malvezzi[3,*], Jennifer Mayor[1,2], Sarah Ryter[1], Hector Moreno[2], Nicole Liechti[1], Andreas Bosshart[3], Chloe Iss[3], Valérie Calabro[3], Andreas Cornelius[3], Tanja Hospodarsch[3], Alexandra Neculcea[3], Thamar Looser[3], Anja Schlegel[3], Simon Fontaine[3], Denis Villemagne[3], Maria Paladino[3], Yvonne Kaufmann[3], Doris Schaible[3], Iris Schlegel[3], Dieter Schiegg[3], Christof Zitt[3], Gabriel Sigrist[3], Marcel Straumann[3], Julia Wolter[3], Marco Comby[3], Julia M. Adler[9], Kathrin Eschke[9], Mariana Nascimento[9], Azza Abdelgawad[9], Achim D. Gruber[10], Judith Bushe[10], Olivia Kershaw[10], Heyrhyoung Lyoo[4], Chunyan Wang[4], Wentao Li[4], Ieva Drulyte[6], Wenjuan Du[4], H. Kaspar Binz[7], Rachel Herrup[8], Sabrina Lusvarghi[8], Sabari Nath Neerukonda[8], Russell Vassell[8], Wei Wang[8], Susanne Mangold[3], Christian Reichen[3], Filip Radom[3], Charles G. Knutson[11], Kamal K. Balavenkatraman[12], Krishnan Ramanathan[13], Seth Lewis[3], Randall Watson[3], Micha A. Haeuptle[3], Alexander Zürcher[3], Keith M. Dawson[3], Daniel Steiner[3], Carol D. Weiss[8], Patrick Amstutz[3], Frank J.M. van Kuppeveld[4], Michael T. Stumpp[3,14,**], Berend-Jan Bosch[4,**], Olivier Engler[1,**], Jakob Trimpert[9,**]

* These first authors contributed equally to this work

** These senior authors contributed equally to this work

[1]Spiez Laboratory, Austrasse, 3700 Spiez, Switzerland

[2]Institute of Microbiology, University Hospital Center and University of Lausanne, Rue du Bugnon 48, 1011 Lausanne, Switzerland

[3]Molecular Partners AG, Wagistrasse 14, 8952 Zurich-Schlieren, Switzerland

[4]Department Biomolecular Health Sciences, Division Infectious Diseases & Immunology - Virology section, Faculty of Veterinary Medicine, Utrecht University, 3584 CL, Utrecht, The Netherlands.

[5]Cryo-Electron Microscopy, Bijvoet Center for Biomolecular Research, Department of Chemistry, Faculty of Science, Utrecht University, Padualaan 8, 3584 CH Utrecht, The Netherlands

[6]Materials and Structural Analysis, Thermo Fisher Scientific, Eindhoven, 5651 GG, The Netherlands.

[7]Binz Biotech Consulting, Lüssirainstrasse 52, 6300 Zug

[8]Laboratory of Immunoregulation, Division of Viral Products, Center for Biologics Evaluation and Research, U.S. Food and Drug Administration, Silver Spring, Maryland, USA

[9]Freie Universität Berlin, Institut für Virologie, Robert-von Ostertag-Straße 7-13, 14163 Berlin, Germany

[10]Freie Universität Berlin, Institut für Tierpathologie, Robert-von Ostertag-Straße 15, 14163 Berlin, Germany

[11]Novartis Institutes for BioMedical Research, PK Sciences, Cambridge, MA, USA

[12]Novartis Institutes for BioMedical Research, Preclinical Safety, Basel, Switzerland

[13]Novartis Pharma AG, Basel, Switzerland

[14]To whom correspondence should be addressed:
Michael T. Stumpp
+41 44 755 77 00
info@molecularpartners.com

Keywords: SARS-CoV-2, COVID-19, coronavirus, mutations, emerging variants, antiviral therapy, ensovibep, MP0420, DARPin drug, ankyrin repeat protein, DARPin, multispecific, K417N, K417T, L452R E484K, N501Y, B.1.1.7, B.1.1.529, B.1.351, P.1, B.1.429, B.1.526, B.1.617, B.1.618, B.1.621, AY.1, alpha, beta, gamma, delta, mu, omicron, Roborovski dwarf hamster

Conflict of interests: authors from Molecular Partners own performance share units and/or stock of the company. H.K.B. owns stock of the company. I.D. is an employee of Thermo Fisher Scientific. C.G.K.; K.K.B. and K.R. are employees of Novartis. The other authors declare no competing interests.

Abstract

SARS-CoV-2 has infected millions of people globally and continues to undergo evolution. Emerging variants can be partially resistant to vaccine induced and therapeutic antibodies, emphasizing the urgent need for accessible, broad-spectrum therapeutics. Here, we report a comprehensive study of ensovibep, the first trispecific clinical DARPin candidate, that can simultaneously engage all three units of the spike protein trimer to potently inhibit ACE2 interaction, as revealed by structural analyses. The cooperative binding of the individual modules enables ensovibep to retain inhibitory potency against all frequent SARS-CoV-2 variants, including Omicron, as of December 2021. Moreover, viral passaging experiments show that ensovibep, when used as a single agent, can prevent development of escape mutations comparably to a cocktail of monoclonal antibodies (mAb). Finally, we demonstrate that the very high in vitro antiviral potency also translates into significant therapeutic protection and reduction of pathogenesis in Roborovski dwarf hamsters infected with either the SARS-CoV-2 wild-type or the Alpha variant. In this model, ensovibep prevents fatality and provides substantial protection equivalent to the standard of care mAb cocktail. These results support further clinical evaluation and indicate that ensovibep could be a valuable alternative to mAb cocktails and other treatments for COVID-19.

Introduction

The extent of the COVID-19 pandemic allowed SARS-CoV-2 to quickly undergo adaptive evolution. The main mutations localize to the spike protein, a metastable prefusion trimer on the viral membrane that mediates virus entry into the host cell. The spike protein comprises multiple functional subunits: S1, which includes the N-terminal domain (NTD) and the receptor binding domain (RBD), responsible for interaction with the angiotensin-converting enzyme 2 (ACE2) host receptor[1-4], and the S2 subunit, which is responsible for virus-host cell membrane fusion via extensive, irreversible conformational changes[5-8]. In the first months of the pandemic, a single mutation, D614G, located in the S2 domain, became prevalent. This mutation impairs premature conformational change of the spike protein, thus increasing the number of infectious viral particles and therefore overall viral infectivity[9]. By November 2021, more viral lineages have been identified and designated as Variants of Interest (VOIs) or Variants of Concern (VOCs) based on their associated increased risk to public health. These were first isolated in the UK (Alpha, B.1.1.7 lineage), South Africa (Beta, B.1.351), Brazil (Gamma, P.1), South California (Epsilon, B.1.429), Nigeria (Eta, B.1.525), New York, (Iota, B.1.526), Peru (Lambda, C.37), Japan (R.1), India (Kappa, B.1.617.1 and Delta, B.1.617.2), Uganda (A.23.1), and, more recently, in Colombia (Mu, B.1.621), the UK (Delta Plus, AY.1), as well as Africa (Omicron, B.1.1.529) [10-22].

Many of these variants harbor mutations in the RBD domain of the spike protein, mainly in the ACE2 binding site (K417T/N, N439K, L452R, E484K/Q, N501Y). Since this region is also highly immunogenic, these mutations have been linked to a dual effect: either increasing the affinity to the human ACE2 receptor (N439K, N501Y) and therefore transmissibility, and/or facilitating immune escape of the virus (K417T/N, L452R, E484K/Q)[10,11,15-17,23-25]. In particular, the E484K substitution has been shown to play a key role in attenuating the potency gain and resistance to the majority of antibodies, according to a study analyzing clinical-stage therapeutic antibodies[12].

Fighting the COVID-19 pandemic requires a coordinated global effort to maximize the benefits of vaccinations and therapeutics[1]. The presence of an unvaccinated portion of the population and the evolution of escape mutants highlights the medical need for globally accessible therapeutics[26]. Neutralizing mAbs are a critically important therapeutic approach against COVID-19. To circumvent their loss of potency due to viral mutational escape, antibody cocktails were generated to provide increased protection against variants[27-29].

We have applied the DARPin platform[30], which allows fast generation and cost-effective production of biological therapeutics, to generate ensovibep, an anti-SARS-CoV-2 multispecific DARPin antiviral clinical candidate[31,32]. DARPins are an emerging class of novel therapeutics that are actively being developed in ophthalmology and oncology[33,34]. They are structurally fully differentiated from antibodies

98 and consist of a single chain of linked DARPin binding domains. In the case of ensovibep, the molecule
99 comprises two human serum albumin binding DARPin domains for systemic half-life extension[35] (H1
100 and H2) and three spike protein RBD-binding DARPin domains at the C-terminus (R1, R2 and R3). The
101 relatively small size of ensovibep (85 kDa), in conjunction with high thermal stability[31], high production
102 yields[31] and demonstrated high protection against viral escape mutations and variants makes this
103 molecule an attractive alternative to other treatments.

104 Using structural analysis, we provide an explanation for ensovibep-mediated neutralization of the SARS-
105 CoV-2 spike protein. The three distinct DARPin domains can simultaneously target the receptor binding
106 ridge on each RBD of the spike trimer, locking the spike in an open-conformation and occluding the
107 ACE2 binding site. Thanks to the cooperative binding of this novel trispecific design, ensovibep confers
108 very high protection against a panel of relevant spike mutants as well as all frequent SARS-CoV-2
109 variants identified around the globe to date. We show in a viral passaging experiment that the
110 protection provided by ensovibep against development of viral escape mutants is equivalent to that of
111 a well characterized and clinically evaluated monoclonal antibody cocktail[27,36,37].

112 Following our *in vitro* characterization, we demonstrate high *in vivo* efficacy in a therapeutic Roborovski
113 dwarf hamster model of COVID-19. Here ensovibep protects against severe disease induced by either
114 wild-type or the Alpha variant SARS-CoV-2. The Roborovski dwarf hamster is highly susceptible to SARS-
115 CoV-2 infection and develops strong lung pathology, with most animals reaching a defined humane
116 endpoint within two to five days after infection[38]. In the presented study, ensovibep protects the
117 animals to an extent equivalent to a standard-of-care mAb cocktail. For both therapeutic agents, a
118 significant reduction of fulminant disease, as well as significantly reduced viral loads and attenuated
119 lung pathology was observed.

120 In brief, the trispecific design of ensovibep provides great protection against all currently known SARS-
121 CoV-2 variants with the potential to protect against emerging variants in the future. Our findings
122 strongly support the progressing clinical development of ensovibep as a potential therapeutic for
123 COVID-19.

124 # Results

125 ## Structural basis for ensovibep-mediated neutralization of the SARS-CoV-2 spike

126 Ensovibep comprises of five covalently linked DARPin domains. Three of them (R1, R2 and R3) bind the
127 RBD of SARS-CoV-2 with picomolar affinity (Supplementary Figure 1) and two of them (H1-H2) bind to
128 human serum albumin (HSA), extending the systemic half-life (Figure 1A). To understand how
129 ensovibep binds to the SARS-CoV-2 spike (S), we selected one of the three RBD-targeting DARPin
130 domains of ensovibep for cryo-EM analysis in complex with the trimeric S-ectodomain. The RBD-binding
131 domains are from the same sequence family and are thus expected to target a common epitope (Figure
132 1B). Upon incubation of the trimeric spike protein with the monovalent DARPin R2 for 15 seconds prior
133 to vitrification, 3D classification revealed that 65% of the S-ectodomains were in the closed
134 conformation, 20% had two RBDs in the open conformation and 15% had all three RBDs in the open
135 conformation (Supplementary Figure 2A, B). For the open RBD classes, additional density, consistent
136 with the size of the monovalent DARPin molecule, was present on the RBD receptor binding ridge (RBR).
137 When the incubation time was increased to 60 seconds, 66% of S-ectodomains had three monovalent
138 DARPin molecule-bound RBDs in the open conformation (Supplementary Figure 2C). Interestingly, 18%
139 of the S-ectodomains had two DARPin-bound RBDs in the open conformation and one trapped in a
140 partially closed conformation (Supplementary Figure 2C and 3A-B). These results demonstrate that
141 monovalent DARPin domain binding prevents closure of the RBD through a previously described
142 ratcheting mechanism[39]. 3D refinement of the fully open class, from the 60 second incubated sample,
143 produced a 4.2 Å global resolution map (Figure 1C and Supplementary Figure 2D-F). Following focused
144 refinement of the RBD region, the quality of the map was sufficient to unambiguously assign the pose
145 of the monovalent DARPin domain, which binds perpendicular to the RBD receptor binding motif (RBM),
146 with its N-terminus orientated toward the spike three-fold symmetry axis (Figure 1C). The concave
147 DARPin binding surface covers the RBD and would prevent ACE2 binding through steric hindrance
148 (Figure 1D). Guided by the cryo-EM data, molecular docking experiments were performed between the
149 RBD of SARS-CoV-2 and DARPin R2.

150 The top scoring model indicated that the interface area is ~700 $Å^2$ and that key epitope residues are
151 F456, Y473, F486, N487 and Y489, which form an interface of hydrophobic interactions and hydrogen-
152 bonds with the DARPin domain (Figure 1E-F). Because the three DARPin domains share a similar
153 paratope composition and architecture, we were able to conceptually model the entire ensovibep
154 molecule bound to the fully open S-ectodomain (Figure 1G). This demonstrated that the linkers would
155 permit simultaneous binding of all three DARPin modules, allowing very high avidity of ensovibep
156 (Supplementary Figure 1), and that the half-life extension modules have sufficient space to bind HSA

157 (not shown). Taken together, these data suggest that ensovibep inhibits SARS-CoV-2 by blocking ACE2
158 binding and promoting the premature conversion of spike to the post-fusion state. This mechanism of
159 inhibition through receptor functional mimicry was observed for a number of SARS-CoV-2 neutralizing
160 antibodies[39,40].

161 **Ensovibep is highly potent against globally identified SARS-CoV-2 variants as well as the most frequent**
162 **spike protein point mutations**

163 In order to assess the neutralizing potencies of ensovibep against the initial SARS-CoV-2 (Wuhan) and
164 emerging variants, we used vesicular stomatitis virus (VSV)-based as well as lentivirus-based
165 pseudoviruses carrying the SARS-CoV-2 wild-type or mutant spike protein at their surface. In addition,
166 we tested the authentic SARS-CoV-2 variants for the Wuhan reference and for lineages B.1.1.7, B.1.351
167 and P.1. Ensovibep is able to neutralize the reference wild type strain with an IC_{50} of ~1 ng/mL, when
168 either the authentic SARS-CoV-2 or the pseudovirus is used (Figure 2A). Remarkably, the high
169 neutralization efficacy is retained in all the frequent variants circulating to date, which display a diverse
170 set of mutations over the entire length of the spike protein (Figure 2A and 2B; Supplementary Table 2;
171 Supplementary Figure 4). In particular, ensovibep can neutralize the variants of concern (VOC) and
172 variants of interest (VOI) of the lineage B.1.1.7/Alpha (69-70 del, del145, E484K, N501Y, A570D, D614G,
173 P681H, T716I, S982A, D1118H and with the addition of E484K or S494P), lineage B.1.351/Beta (L18F,
174 D80A, D215G, Del242-244, R246I, K417N, E484K, N501Y, D614G, A701V), lineage P.1/Gamma (L18F,
175 T20N, P26S, D138Y, R190S, K417T, E484K, N501Y, D614G, H655Y, T1027I, V1176F), B.1.617.2/Delta
176 (T19R, G142D, del156-157, R158G, L452R, T478K, D614G, P681R, D950N) and AY.2/Delta Plus (T19R,
177 G142D, del156-157, R158G, K417N, L452R, T478K, D614G, P681R, D950N), Lambda (C.37; G75V, T76I,
178 del246-252, D253N, L452Q, F490S, D614G, T859N), Mu (B.1.621; T95I, Y144S, Y145N, R346K, E484K,
179 N501Y, D614G, P681H, D950N) and Omicron (B.1.1.529; A67V, Δ69-70, T95I, G142D, Δ143-145, Δ211,
180 L212I, ins214EPE, G339D, S371L, S373P, S375F, K417N, N440K, G446S, S477N, T478K, E484A, Q493K/R,
181 G496S, Q498R, N501Y, Y505H, T547K, D614G, H655Y, N679K, P681H, N764K, D796Y, N856K, Q954H,
182 N969K, L981F). The neutralization potencies of ensovibep remain within 10-fold difference from the
183 reference virus (Wuhan or D614G variant) with IC_{50} values in the low single-digit ng/mL range, even
184 against those variants that have been shown to be, to a large extent, refractory to vaccine- or infection-
185 related antibody neutralization, such as Beta, Gamma, Delta, Delta Plus, and the newly evolved Omicron
186 variant.[25,41-43] When testing the neutralizing potency in a VSV-based pseudotype assay, containing more
187 than 30 substitutions of the Omicron spike protein, ensovibep maintained neutralization at low single
188 digit ng/mL IC_{50} values without loss in potency, when compared to the wild type. In contrast, many of
189 the tested clinically relevant monoclonal antibodies and antibody cocktails demonstrated a major loss
190 in neutralization (Figure 2D).

191 Using the VSV- and lentivirus-based pseudovirus neutralization assays, we also evaluated the influence
192 of single mutations on the neutralization potency of ensovibep, of the monovalent DARPin molecules
193 and of the mAbs REGN10933 and REGN10987, as a reference within the same experiment. The panel
194 included mutations present on variants of interest/concern, appearing frequently, or located within the
195 binding epitope of ensovibep. Most notably, ensovibep protected well against all point mutations
196 tested, in contrast to the single monoclonal antibodies, with the only exception of substitution F486V,
197 which affects all three monovalent DARPin RBD binders incorporated in ensovibep (Figure 2C). A major
198 impact of this mutation is not surprising, as our structural analysis and modelling identifies F486 as a
199 core interacting residue for the three related but distinct RBD binders[31] (Figure 1B,F). Consequently,
200 the mutation F486V destabilizes the binding of the entire tri-specific ensovibep molecule to the spike
201 protein. However, F486 is also a critical residue for the interaction between the RBD of SARS-CoV-2 and
202 human ACE2 and its mutation leads to a ~8.5-fold reduction of the binding affinity as well as a ~17-fold
203 reduction of the ability of ACE2 to reduce the infection of a VSV-based pseudovirus carrying the F486L
204 mutation (Supplementary Figure 6). The functional importance of F486 is reflected by a low frequency
205 of naturally occurring substitutions at this site (Figure 2C; Supplementary Table 3; Supplementary
206 Figure 4) where the selective pressure on the virus favors a phenylalanine, thus maintaining the key
207 anchoring element for ensovibep binding. A reduction of the potency of ensovibep from one-digit to
208 double-digit ng/mL IC_{50} was also observed for mutation N234Q. This residue is located outside of the
209 RBD binding region of ensovibep. This minor effect of substitution N234Q could be related to the loss
210 of the conserved glycosylation site at this position, favoring the kinetics of the down conformation of
211 the RBD domain and thus reducing binding of ensovibep as well as ACE2 to the RBD, which only bind
212 the RBD up confirmation.[44]

213 It is interesting to note that ensovibep retains potency against spike proteins carrying mutations at
214 locations where the single DARPin domains partially lose activity, such as E484K and Q493K/R. We
215 hypothesize that the cooperative binding in combination with the complementarity of the three
216 independent RBD-binding DARPin modules provides resistance to mutation escape. Taken together,
217 our analysis demonstrates that the trispecific design of ensovibep enables very high potencies against
218 spike proteins carrying the most frequently observed mutations as well as mutations known to impact
219 the binding of neutralizing antibodies.

220 *Passaging of SARS-CoV-2 under therapeutic pressure of DARPin antivirals and monoclonal antibodies*

221 Previous studies have shown that SARS-CoV-2 escape mutants may arise under selective pressure of a
222 therapy[29,45]. Using a viral passaging model, we compared the risk of mutational escape from therapeutic

223 pressure of ensovibep compared to that of its monovalent R2 module, the mAbs REGN10933 and
224 REGN10987, singly and as a 1:1 mixture, as well as the mAb S309.

225 In order to generate a stringent therapeutic pressure, a relatively high viral load of 1.5 x 10^6 pfu of an
226 authentic French SARS-CoV-2 WT isolate (with the following differences to the Wuhan wild-type spike
227 protein: V367F; E990A) was serially passaged in the presence of increasing concentrations of DARPin
228 molecules and antibodies (Figure 3A,B). Resistant escape variants were further selected by passaging
229 the supernatant of cultures showing significant virus-induced cytopathic effect (CPE) under the
230 selection pressure of the highest therapeutic concentration onto fresh cells while maintaining the
231 selective pressure of increasing concentrations of therapeutic antivirals (Supplementary Figure 5). After
232 the first incubation cycle of four days (passage 1), ensovibep, DARPin R2, REGN10933 and the antibody
233 mixture conferred protection at the same concentration of 0.4 µg/mL. S309 was less efficient, requiring
234 a higher concentration (10 µg/mL) for protection and REGN10987 was not protective up to the highest
235 tested concentration of 50 µg/mL. Under continuous selective pressure through passage 2 to 4, DARPin
236 R2 and the individual mAbs S309 and REGN10933 lost the capacity to protect cells, which manifested
237 in complete CPE up to 50 µg/mL. In contrast, ensovibep and the cocktail of two mAbs remained effective
238 and protected cells from CPE throughout the four passages (Figure 3A).

239 To identify putative escape mutations in the spike protein upon therapeutic pressure of the DARPins,
240 RNA was extracted and deep-sequenced from the supernatant of wells with the greatest selective
241 pressure showing a significant cytopathic effect in each passage (Figure 3B). Mutations were found near
242 the spike protein cleavage site (H655Y, N679_R685del, R682W, R682Q), which are likely related to
243 adaptations to the experimental cell system and thus would not account for escape mutations due to
244 the therapeutic pressure of the DARPin[36, 37], as well as a potential escape mutation, F486L, which was
245 found for the monovalent DARPin R2 but not for ensovibep, up to passaging round four. Still, supporting
246 this finding, mutations in F486 were shown to influence also the potency of ensovibep, when analyzed
247 separately.

248 ***In vivo antiviral efficacy of ensovibep in a COVID- 19 SARS-CoV-2 Roborovski dwarf hamster model***

249 To test the *in vivo* efficacy of ensovibep in treating SARS-CoV-2 infection, we employed the Roborovski
250 dwarf hamster, a species susceptible to severe COVID-19 like illness[46]. Unlike the more commonly used
251 Syrian golden hamster[47], this species is prone to develop a lethal course of disease, notably without the
252 extrapulmonary disease manifestations observed in highly susceptible transgenic mice[48]. We used this
253 particular animal model to judge the *in vivo* efficacy of ensovibep and to compare it to the REGN10933
254 & REGN10987 antibody mixture. Moreover, evaluation of the virological and histopathological outcome
255 of infection enabled comparison across a variety of important parameters of infection.

256 We first aimed to determine *in vivo* protection conferred by ensovibep against a SARS-CoV-2 wild type
257 reference strain (BetaCoV/Germany/BavPat1/2020). In an initial series of experiments, we determined
258 both dose and time dependency of treatment efficacy based on clinical and virological parameters. In
259 absence of venous access in dwarf hamsters, we choose intraperitoneal (i.p.) treatment for delivery of
260 ensovibep. It is important to note, that the course of disease in Roborovski dwarf hamsters is rapid,
261 with first animals developing severe disease and reaching termination criteria within 48 hours of
262 infection. For this reason, we considered 24 hours post-infection (p.i.) the latest possible intervention
263 time point. Both dose and time of ensovibep administration (relative to time of infection) were found
264 to positively affect the outcome of infection. Specifically, the use of ensovibep resulted in markedly
265 reduced virus loads in the respiratory tract of treated animals (Supplementary Figure 7).

266 From these initial results, we determined 10 mg/kg to be the optimal dose for ensovibep treatment
267 and in further studies compared this dose with the same dose of the REGN10933 & REGN10987 cocktail
268 using the SARS-CoV-2 alpha (B.1.1.7) variant of a more recent isolate
269 (BetaCoV/Germany/ChVir21652/2020) for infection of animals. We chose two treatment time points,
270 the first at the time of infection to mimic clinical post exposure prophylaxis and the second at 24 h p.i.
271 to mimic treatment at the onset of clinical symptoms (Figure 4A). For the post exposure prophylaxis
272 dosed directly after infection (0 h p.i.), we confirmed full protection for both treatments with notable
273 reduction of viral loads, particularly in the lungs of treated animals compared to placebo treated
274 controls at all time points (Figure 5A). There were no obvious differences between the two agents,
275 however, based on virological parameters, a slight trend towards lower viral load in the antibody
276 cocktail group was observed at 5 days p.i. (Figure 5A).

277 In contrast to the similarities in the post exposure prophylaxis setting we observed differences between
278 the groups treated 24 hours p.i. (Figure 4B, C). In this scenario, animals treated with ensovibep
279 presented with improved condition at 2 days p.i. with 0/12 of the animals reaching a defined humane
280 endpoint, while 5/12 animals were euthanized in the mAb cocktail group and 5/12 in the placebo group
281 (Figure 5B) due to reached humane endpoints. Nevertheless, 3/10 hamsters in the ensovipeb group
282 and an additional three hamsters in the placebo group reached defined endpoints at day 3 p.i., while
283 no further animals in the mAb cocktail group developed severe illness after day 3 p.i. (Figure 5B).
284 Following 24 h p.i. treatment, no significant differences in average body weights or temperatures were
285 observed in any of the treatment groups (Figure 5C, Supplementary Figure 8). This is likely a result of
286 the early termination of severely sick animals, while the healthier animals remained in the study.
287 However, examination of these parameters on day 2 p.i. revealed significant trends towards reduced
288 body weight loss in both treatment groups compared to the placebo and a similar trend towards higher
289 body temperatures in the ensovibep group compared to the other groups (Figure 5C). As body

290 temperature decrease is a very sensitive parameter of disease in this species[46], this in particular is
291 reflective of the improved condition in the ensovibep treated group at 24h p.i., when compared to the
292 antibody cocktail treated or the placebo treated animals. Virological readouts were not significantly
293 different between groups treated with ensovibep and the mAb cocktail at 24 hours post-infection. Both
294 treatments resulted in drastic reductions of viral load compared to the placebo group (Figure 5A, B).
295 This result was more pronounced at the level of replicating virus, indicating efficient neutralization of
296 cell-free virus in both treatment groups (Figure 5B). These trends were likewise reflected by the results
297 of histopathological examinations of animals treated at 24 h p.i.. While the histological outcome of
298 infection was similar between both treatment groups (Figure 6), semi-quantitative assessment of SARS-
299 CoV-2 induced lesions revealed consistently higher scores for the mAb treated group compared to
300 ensovibep. Interestingly, scores for inflammation in the mAb treated group were on average exceeding
301 the scores obtained for the placebo group. These findings need to be interpreted knowing that 5/6
302 animals in the mAb treated group which had been scheduled for termination and analysis at day 3 had
303 to be taken out of the study already on day 2 due to rapid onset of fulminant disease, which is reflected
304 by these readouts.

305 To account for possible differences in exposure, we performed pharmacokinetic analysis for both
306 treatments. These assessments identified that overall, comparable exposures were achieved in non-
307 infected hamster following i.p. administration. It was noted that, ensovibep achieved a higher maximal
308 serum concentration (Cmax) and a shorter systemic half-life compared to the mAb cocktail
309 (Supplementary Figure 9).

310 Considering the small size of the Roborovski dwarf hamster, failure of i.p. injection due to an accidental
311 injection into body compartments other than the peritoneum may occur. We thus screened for animals
312 which lacked a proper drug exposure in terminal serum samples and removed data of these animals
313 from all other analyses (Supplementary Table 4).

314 Whole genome sequencing using virus RNA recovered from lungs and upper respiratory tract was
315 performed to investigate whether SARS-CoV-2 escape mutants were selected under ensovibep
316 treatment. Viral RNA from individual animals with higher viral load compared to other animals of the
317 same treatment group was analyzed and no escape mutations affecting the ensovibep epitope located
318 in the RBD were discovered (Supplementary Table 5).

319 ## Discussion

320 Multiple strategies are urgently needed to combat the COVID-19 pandemic. Next to preventive
321 vaccination approaches and small molecules, mAbs are showing therapeutic promise, based on highly
322 potent virus inhibition and encouraging animal and clinical efficacy. However, manufacturing capacities
323 are limiting a global supply and novel emerging variants of SARS-CoV-2 are an ever-present threat, as
324 they may escape the antibodies generated during immunization or in response to therapeutics. A
325 number of alternative molecules are being developed to complement and partially overcome these
326 limitations.

327 In the present study, we provide the structural and functional analysis of ensovibep, a trispecific DARPin
328 designed as a potential alternative to antibodies and other therapeutics[32,49-53]. The structural analysis
329 provides insights into the mode of action, which enables low picomolar neutralizing activity against the
330 currently most frequent SARS-CoV-2 mutations as well as recently identified variants. We measured the
331 effect of ensovibep on a panel of single spike protein mutations which have been shown to be of
332 concern because they may be associated with increased transmissibility, disease severity, or affect
333 neutralization of some monoclonal- or polyclonal antibodies[27,54,55]. Among all mutations tested, only
334 F486 substitutions caused a strong decrease in ensovibep potency when compared to the wild-type or
335 reference virus. The effect of this mutation was also noted in the viral passaging study: sequencing of
336 mutations allowing escape from inhibition by the monovalent RBD binder (R2, incorporated in
337 ensovibep) identified F486L (Figure 3B). These findings are in line with our structural analysis (Figure
338 1F) showing that F486 is one of the key binding residues for the interaction of ensovibep with the RBD.
339 Most importantly, F486 is a critical residue for the virus itself, allowing an efficient binding to the ACE2
340 receptor and thus cell infection. Therefore, mutations of the phenylalanine at position 486 will decrease
341 the affinity between the RBD and human ACE2 receptor and lower the infectivity of the virus[17,56-58]
342 (Supplementary Figure 6). We thus expect that position F486 in the SARS-CoV-2 spike protein will
343 remain conserved to maintain efficient binding to the human ACE2 receptor or that the virus might lose
344 fitness if mutated at this position. So far, based on the global SARS-CoV-2 database sequences published
345 in the GISAID database (https://www.gisaid.org/hcov19-variants/; visited November 2021), mutations
346 in position F486 occur at very low frequencies.

347 A small reduction of neutralization potency observed for ensovibep and its single DARPin moieties for
348 viruses bearing the N234Q mutation outside of the RBD might be explained by the impact of the
349 mutation on the RBD conformational dynamics. An *in-silico* simulation study showed that this
350 conserved glycosylation site, together with N165, might be involved in the stabilization of the RBD up-
351 conformation. Since the epitope of ensovibep is exposed only in the up-conformation, a mutation in

352 one of these glycosylation sites might affect its binding equilibrium, as indicated in our neutralization
353 assays. The N234Q mutation might thus impact all protein binding scaffolds that are binding exclusively
354 to the up-conformation of the RBD. By the same token, reduced affinity of the spike protein for the
355 human ACE2 receptor was demonstrated elsewhere in *in vitro* assays[44]. Accordingly, mutations of the
356 N165 and N234 amino acids have been observed only at low frequencies (<0.02%).

357 Some mutations that are not predicted to be key interaction residues for the three distinct RBD binders
358 of ensovibep (e.g., E484K or Q493K), led to a reduction in potency for one or several of the RBD-binding
359 monovalent DARPins, while the trispecific ensovibep molecule maintained full neutralization capacity.
360 This demonstrates that the trispecific DARPin design of ensovibep, with cooperative binding of three
361 distinct paratopes (Supplementary Figure 1), permits high neutralizing potency, even in the case when
362 an individual monovalent DARPin domain exhibits decreased affinity (Figure 2A). This cooperative
363 binding of multiple paratopes is a hallmark of the trispecific nature of ensovibep and differentiates the
364 molecule from mAb candidates to allow full neutralization of highly mutated SARS-CoV-2 variants such
365 as Omicron, that are substantially different from the original virus that the mAb was selected against[59].

366 The high level of protection against viral escape mutations by ensovibep demonstrated in the virus
367 challenge studies was also clearly apparent in a viral passaging experiment. The single mAbs and the
368 monovalent DARPin binder were rapidly overcome by escape mutants whereas ensovibep maintained
369 potency to an extent comparable to a clinically validated mAb cocktails.

370 Translatability of the observed *in vitro* activity of ensovibep against SARS-CoV-2 was evaluated in a
371 COVID-19 model using the highly susceptible Roborovski dwarf hamsters. Using this *in vivo* model, we
372 confirmed the therapeutic benefit of ensovibep, which displayed comparable outcomes to a clinically
373 validated antibody cocktail (REGN10933 & REGN10987). In our comparison, we found evidence for a
374 better performance of ensovibep in a late intervention scenario with prolonged survival of animals and
375 reduced inflammation of the lungs. Potential reasons for this difference include differences in
376 pharmacokinetics where ensovibep demonstrated a higher maximal concentration compared to the
377 antibody cocktail (Supplementary Figure 9). Another possible explanation could be that ensovibep lacks
378 an Fc-fragment when compared to antibodies stimulating pro-inflammatory immune responses mostly
379 via their Fc-fragment. Regardless of this, we clearly demonstrate that ensovibep has great potential to
380 prevent disease and eliminate the virus in a highly susceptible *in vivo* model under different treatment
381 scenarios. The clinical translatability of these results is currently being investigated in the EMPATHY trial
382 for the treatment of ambulatory COVID-19 patients.

383 In conclusion, ensovibep, has been shown to have highly potent neutralization against the currently
384 most frequent SARS-CoV-2 variants due to its cooperative and complementary binding to a highly

385 conserved epitope region on the spike RBD. *In vitro* and *in vivo* single agent efficacies closely match the
386 performance of one of the best clinically validated mAb cocktails. In addition, the albumin binding
387 domains of the molecule have been demonstrated to confer a plasma half-life compatible with single
388 dose treatment. Translation of these preclinical findings into the clinic is currently under investigation
389 and if successful, the *E. coli* based-manufacturing of the agent will allow rapid and large-scale
390 production for global access to this alternative class of therapeutics as an addition to other treatment
391 approaches for COVID-19.

392 Data availability

393 The EM density maps for the SARS-CoV-2 spike ectodomain in complex with monovalent DARPin R2
394 (state 1 and state 2), have been deposited to the Electron Microscopy Data Bank under the accession
395 codes EMD-11953 and EMD-11954, respectively. The monovalent DARPin and multivalent DARPin
396 sequences, and pseudo-atomic models derived from molecular docking experiments, are available
397 here, to allow the use of the data for non-commercial purposes:
398 https://www.guidetopharmacology.org/GRAC/LigandDisplayForward?tab=structure&ligandId=11470
399

400 Acknowledgements

401 S.R. & J.M. were supported by Swiss Federal Office for Civil Protection (Grants Nr. 353008564/Stm,
402 353008218/Stm, and 353008560/Stm to Olivier Engler and Stefan Kunz).
403 D.L.H. is funded by the European Union's Horizon 2020 research and innovation program under the
404 Marie Skłodowska-Curie grant agreement (No 842333) and holds an EMBO non-stipendiary long-term
405 Fellowship (ALTF 1172-2018). Cryo-EM data processing was carried out on the Dutch national
406 e-infrastructure with the support of the SURF Cooperative.
407 The authors also thank Dr. Gert Zimmer for the gift of the recombinant VSV (Institute of Virology and
408 Immunology (IVI), CH-3147 Mittelhäusern, Switzerland, Department of Infectious Diseases and
409 Pathobiology, Vetsuisse Faculty, University of Bern, CH-3012 Bern, Switzerland).
410 The expression plasmid for the SARS-CoV-2 spike protein was kindly provided by Dr. Giulia Torriani and
411 Dr. Isabella Eckerle (Department of Medicine, University of Geneva, Switzerland).
412 We would like to thank Dr. Sylvie van der Werf for the supply of 2019-nCoV/IDF0372/2020 (National
413 Reference Centre for Respiratory Viruses hosted by Institut Pasteur (Paris, France)). Strain 2019-
414 nCoV/IDF0372/2020 was generously provided by Dr. X. Lescure and Pr. Y. Yazdanpanah from the Bichat
415 Hospital.Additionally, we would like to thank William Lee, former board member of Molecular Partners
416 - and the Virology group at Gilead Sciences for their helpful input.
417 We would like to thank the Centre for AIDS Reagents (National Institute for Biological Standards and
418 Control, Herts, UK) for providing VeroE6/TMPRSS2 cells.
419 Lentivirus pseudotype investigations were performed independently by investigators at the US Food
420 and Drug Administration, Center for Biologics Evaluation and Research as part of Therapeutics Research
421 Team for the US government COVID-19 response efforts. The work was supported by US government
422 research funds.
423

424 Funding

425 The work was funded by Molecular Partners AG, Switzerland, or as stated in the Acknowledgements.

426

427

428

429 Main Figures for

430

431 Ensovibep, a novel trispecific DARPin candidate that
432 protects against SARS-CoV-2 variants

433

434 Rothenberger et al. 2021

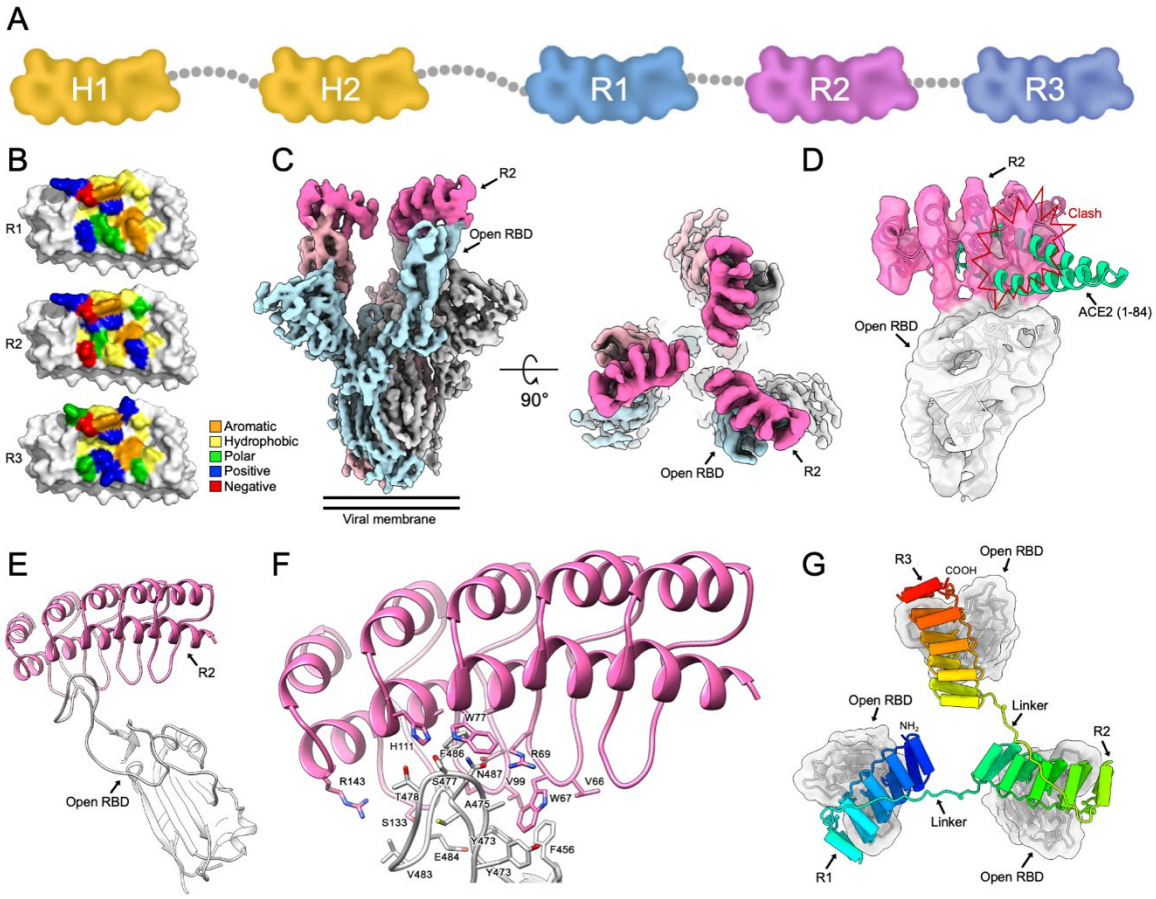

Figure 1: Structural modelling of ensovibep. *A) Schematic overview of the ensovibep construct. Protein linkers are depicted as gray dashed lines and the half-life extending human serum albumin binding monovalent DARPins (H1 and H2) are colored yellow. B) Surface representations of the three monovalent DARPin molecules binding to the RBD, with the amino acid residues in the paratope colored according to their biophysical characteristics as indicated. C) Cryo-EM density for the SARS-CoV-2 spike ectodomain in complex with the RBD-targeting monovalent DARPin R2, shown as two orthogonal views. The DARPin density is colored magenta and the three spike protomers are colored light blue, grey and pale pink. D) Zoomed in view of an RBD-bound to DARPin R2 with the cryo-EM density shown semi-transparent. The atomic coordinates for the fitted open RBD (PDB ID: 6XCN) and the DARPin model are overlaid. The atomic coordinates for residues 1-84 of the RBD-bound ACE2 (PDB ID: 6M0J), colored green, is superimposed. E) Pseudo-atomic model of the monovalent DARPin R2 in complex with the RBD, colored pink and grey, respectively. F) Zoomed in view of the interface between monovalent DARPin R2 and RBD. G) Proposed model of the three covalently linked RBD-targeting monovalent DARPin molecules of ensovibep bound to the trimeric spike protein RBD domains. The three DARPin domains are shown in a rainbow color scheme from the N terminus (blue) to the C terminus (red).*

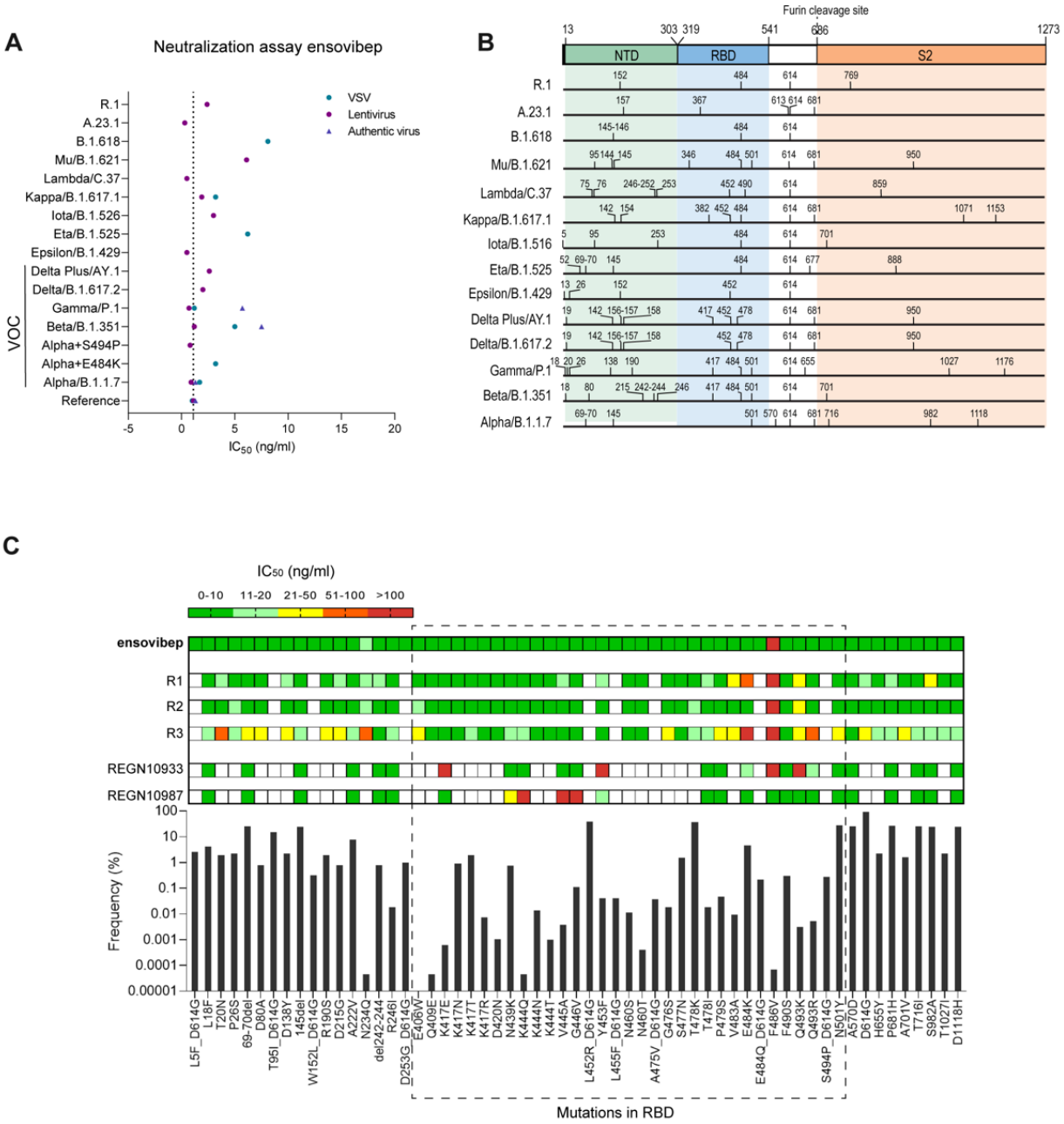
A
Neutralization assay ensovibep
VSV
Lentivirus
Authentic virus
R.1
A.23.1
B.1.618
Mu/B.1.621
Lambda/C.37
Kappa/B.1.617.1
Iota/B.1.526
Eta/B.1.525
Epsilon/B.1.429
Delta Plus/AY.1
Delta/B.1.617.2
Gamma/P.1
Beta/B.1.351
Alpha+S494P
Alpha+E484K
Alpha/B.1.1.7
Reference
VOC
IC50 (ng/ml)
B
Furin cleavage site
NTD
RBD
S2
C
IC50 (ng/ml)
0-10
11-20
21-50
51-100
>100
ensovibep
R1
R2
R3
REGN10933
REGN10987
Frequency (%)
Mutations in RBD

453

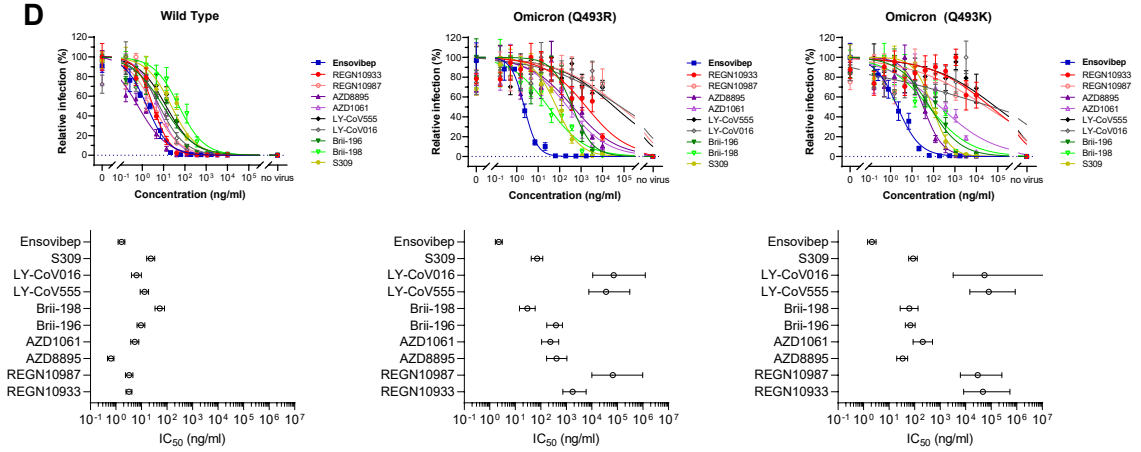

Table 2: Neutralization of ensovibep and a panel of monoclonal antibodies in two VSV-pseudotype assays (including Q493R or Q493K) containing the Omicron variant spike protein with >30 substitutions.					
	Wild Type	**Omicron (Q493R)[1]**		**Omicron (Q493K)[2]**	
Compound	IC_{50} (ng/mL)	IC_{50} (ng/mL)	fold change to wt	IC_{50} (ng/mL)	fold change to wt
ensovibep	1.6	2.2	1.4	2.1	1.3
REGN10933	3.2	>1000	>100	>1000	>100
REGN10987	3.3	>1000	>100	>1000	>100
LY-CoV555	13	>1000	>100	>1000	>100
LY-CoV016	6.4	>1000	>100	>1000	>100
S309	23	72	3.1	87	3.8
AZD8895	0.6	415	>100	34	56
AZD1061	5.5	237	43	207	38
Brii-196	9.5	392	41	68	7.1
Brii-198	52	30	0.6	62	1.2

IC_{50}: *green: <10 ng/mL; orange: 10-100 ng/mL; dark orange: 100-1000 ng/mL; red: >1000 ng/mL*
fold change to wt: *green: <10-fold; orange: 10-100-fold; red: >100-fold*

[1] Set of mutations: A67V, Δ69-70, T95I, G142D, Δ143-145, Δ211, L212I, ins214EPE, G339D, S371L, S373P, S375F, K417N, N440K, G446S, S477N, T478K, E484A, Q493R, G496S, Q498R, N501Y, Y505H, T547K, D614G, H655Y, N679K, P681H, N764K, D796Y, N856K, N969K, L981F.
[2] Set of mutations: A67V, Δ69-70, T95I, G142D, Δ143-145, Δ211, L212I, ins214EPE, G339D, S371L, S373P, S375F, K417N, N440K, G446S, S477N, T478K, E484A, Q493K, G496S, Q498R, N501Y, Y505H, T547K, D614G, H655Y, N679K, P681H, N764K, D796Y, N856K, Q954H, N969K, L981F.

Figure 2: *A) Graph reporting IC_{50} values (ng/mL) for ensovibep measured in neutralization assays performed with lentivirus-, VSV-based pseudoviruses or authentic viruses for the variants indicated. Reference variant is the Wuhan strain for VSV-based pseudovirus, a D614G variant for the lentivirus-based pseudovirus or a patient isolate from the early pandemic for the authentic virus. B) Schematic representation of the residues modified in the SARS-CoV-2 spike protein for the different variants tested compared to the Wuhan strain. C) Graph with global frequencies of point mutations in the spike protein of SARS-CoV-2 according to the GISAID database (as of October 2021) including a heat map table with IC_{50} values for ensovibep, R1, R2, R3, REGN10933, REGN10987 for all point mutations tested (VSV/Lentivirus-based pseudovirus assays). Dashed box: mutations in RBD. D) Titration curves and IC_{50} values for VSV-pseudotype neutralization assays with wild-type and two different Omicron variant spike proteins containing either an arginine or a lysine in position Q493. Ensovibep was tested together with a panel of clinically validated monoclonal antibodies. The table provides the numeric IC_{50} values as well as the fold change towards the wild-type values.*

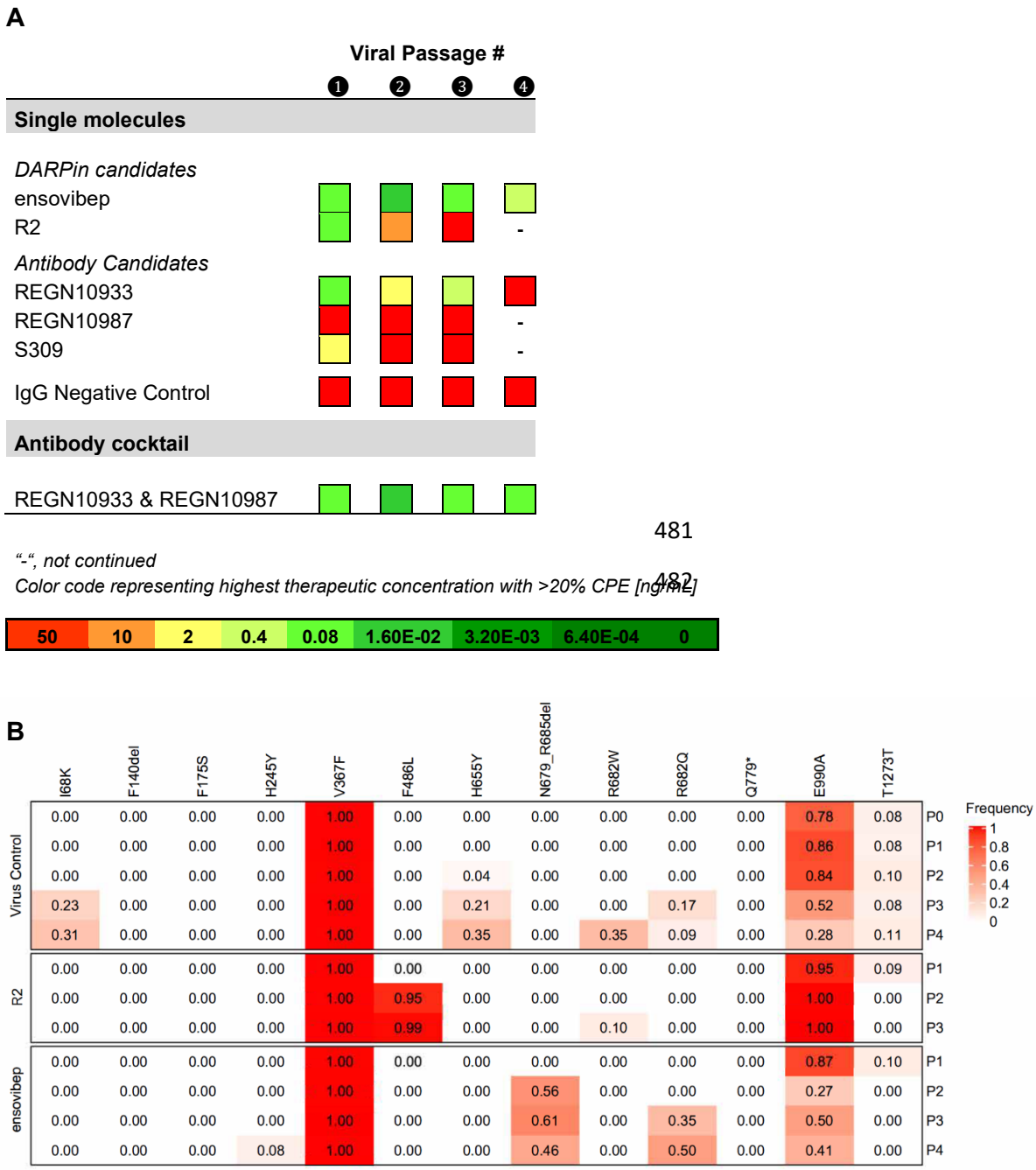

Figure 3: Protection against SARS-CoV-2 escape mutations generated over four viral passages.

A) Tabular representation of the cytopathic effects induced by SARS-CoV-2 cultured in the presence of increasing concentrations of mono-valent DARPin binder R2, multi-specific DARPin antiviral ensovibep and the antibody antivirals REGN10933, REGN10987 and S309 or a cocktail of REGN10933 and REGN10987 through passage 1 to 4. Color code represents the highest concentration showing ≥20% CPE, for which the culture supernatants was passaged to the next round and deep sequenced for the identification of potential escape mutations. B) Identification of escape mutations in viral passages using deep sequencing.

502 *SARS-CoV-2 virus was serially passaged with the mono-valent DARPin binder R2 and*
503 *ensovibep. To identify putative escape mutations in the spike protein, RNA was extracted and*
504 *sequenced from supernatant of wells with the greatest selective pressure showing a significant*
505 *cytopathic effect. All variants in the spike protein relative to the reference genome*
506 *(NC_045512.2) are shown. Passage 0 of the virus control corresponds to the inoculum used*
507 *for all experiments. The color of the fields is proportional to the fraction of the reads containing*
508 *the respective variant (red= 1.0 white=0.0).*

509 **A**

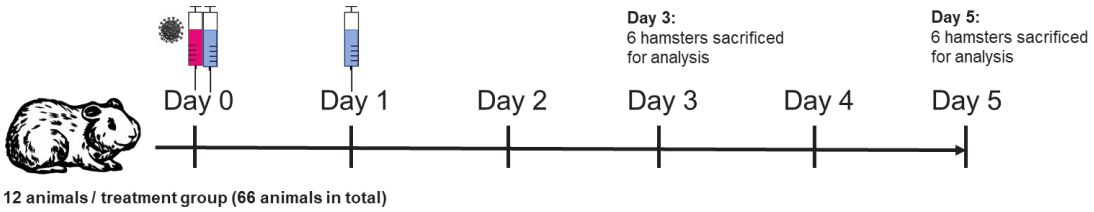

510

511

512 **B**

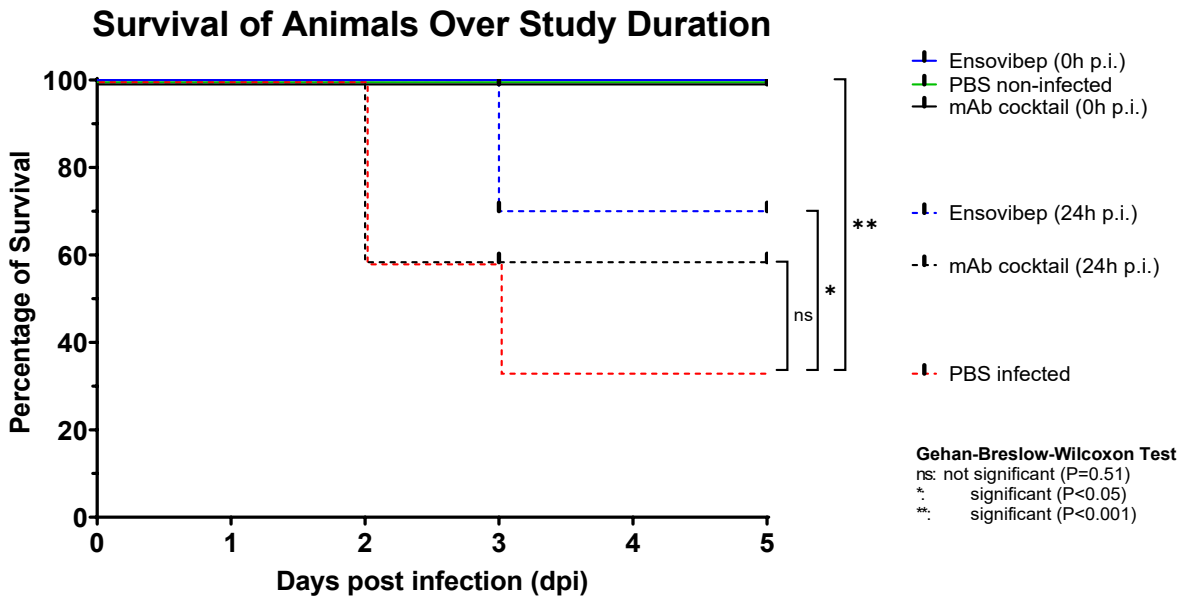

513

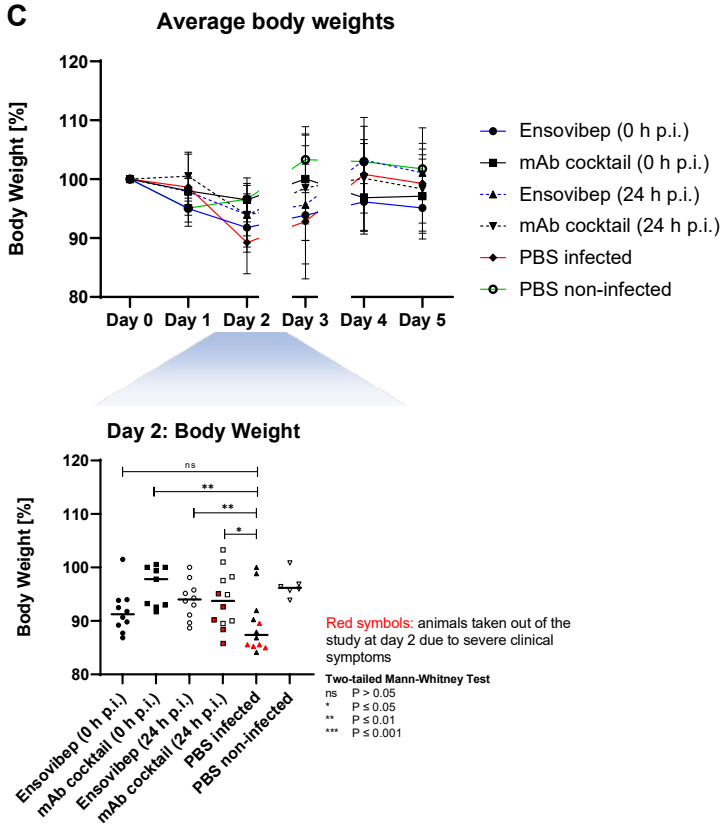
C
Average body weights
Body Weight [%]
120
110
100
90
80
Day 0
Day 1
Day 2
Day 3
Day 4
Day 5
Ensovibep (0 h p.i.)
mAb cocktail (0 h p.i.)
Ensovibep (24 h p.i.)
mAb cocktail (24 h p.i.)
PBS infected
PBS non-infected
Day 2: Body Weight
ns
**
**
*
Red symbols: animals taken out of the study at day 2 due to severe clinical symptoms
Two-tailed Mann-Whitney Test
ns P > 0.05
* P ≤ 0.05
** P ≤ 0.01
*** P ≤ 0.001

514

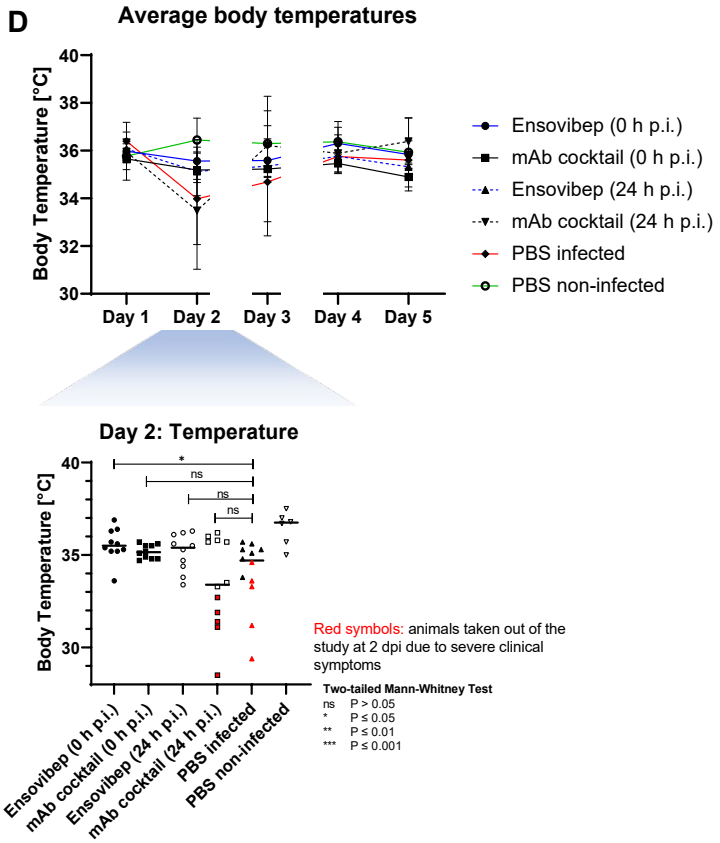
D
Average body temperatures
Body Temperature [°C]
40
38
36
34
32
30
Day 1
Day 2
Day 3
Day 4
Day 5
Ensovibep (0 h p.i.)
mAb cocktail (0 h p.i.)
Ensovibep (24 h p.i.)
mAb cocktail (24 h p.i.)
PBS infected
PBS non-infected
Day 2: Temperature
*
ns
ns
ns
Red symbols: animals taken out of the study at 2 dpi due to severe clinical symptoms
Two-tailed Mann-Whitney Test
ns P > 0.05
* P ≤ 0.05
** P ≤ 0.01
*** P ≤ 0.001

515

516 ***Figure 4:*** *A) Design of the Roborovski dwarf hamster study. Animals were infected on day 0*
517 *with 10^5 pfu of SARS-CoV-2 alpha (B.1.1.7) variant. Treatment was administered either*
518 *directly following infection (0 h p.i.) or one day post infection (24 h p.i). For each treatment*
519 *group, twelve animals were injected i.p. with either 10 mg/kg of ensovibep, 10 mg/kg*
520 *monoclonal antibody cocktail (5 mg/kg REGN10933 & 5 mg/kg REGN10987), or PBS*
521 *(placebo). Additionally, a group of six non-infected and non-treated control animals were*
522 *included as comparators for the infected and treated groups. Daily measurement of body*
523 *weight and temperatures as well observation of vital symptoms was undertaken. Animals were*
524 *sacrificed on day 3 or 5 p.i. or immediately once an individual reached a defined humane*
525 *endpoint. B) Survival of animals for 5 days p.i.. Animals that had to be euthanized according*
526 *to defined humane endpoints were considered as non-survived. B) Body weight and C) body*
527 *temperatures throughout the study duration. Individual data points show mean +/- SD of the*
528 *following number of animals analyzed per treatment group at (0/1/2/3/4/5) days p.i.: Esovibep*
529 *0h: n=10/10/10/10/5/5; mAb cocktail 0h: n=9/9/9/9/5/5; Esovibep 24h: n=10/10/10/10/5/5;*
530 *mAb cocktail 24h: n=12/12/12/7/6/6; Placebo, infected: n=12/12/12/7/4/4; Placebo, non-*
531 *infected: n=6/6/6/6/6/6. The rational for excluding animals is the identification of animals with*
532 *low drug exposure, likely due to a failure of i.p. injections. These animals were excluded from*
533 *all analyses. Lines connecting dots are interrupted for any change in animal numbers between*
534 *consecutive days.*

535 *Since a considerable number of animals in the mAb cocktail and placebo groups reached*
536 *defined humane endpoints by day 2 p.i., This day is zoomed in and values are presented for*
537 *each individual animal with red symbols marking animals that had to be euthanized.*

538 **A**

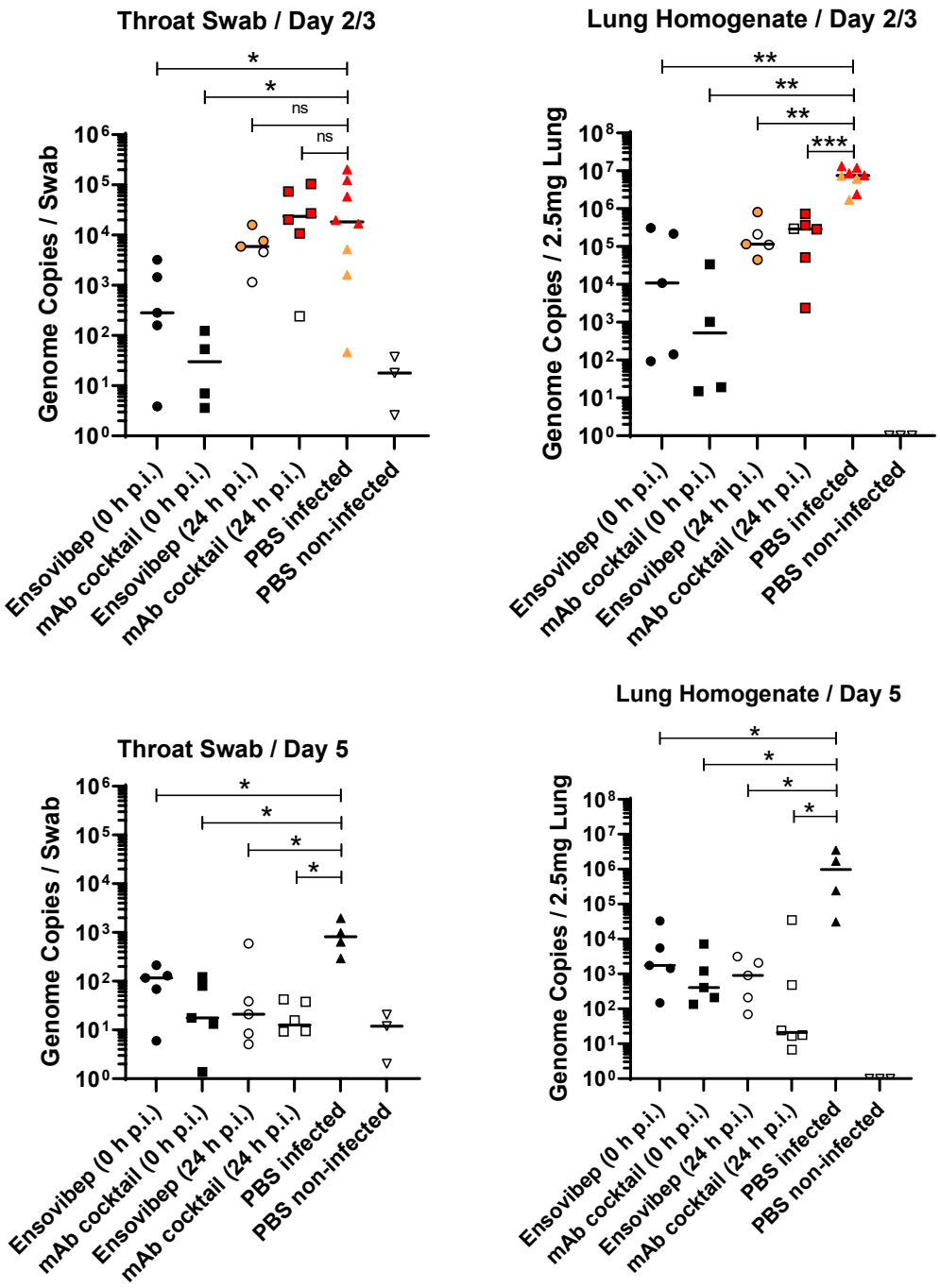
Throat Swab / Day 2/3
Genome Copies / Swab
Lung Homogenate / Day 2/3
Genome Copies / 2.5mg Lung
Throat Swab / Day 5
Genome Copies / Swab
Lung Homogenate / Day 5
Genome Copies / 2.5mg Lung
Ensovibep (0 h p.i.)
mAb cocktail (0 h p.i.)
Ensovibep (24 h p.i.)
mAb cocktail (24 h p.i.)
PBS infected
PBS non-infected
ns

539

540 **B**

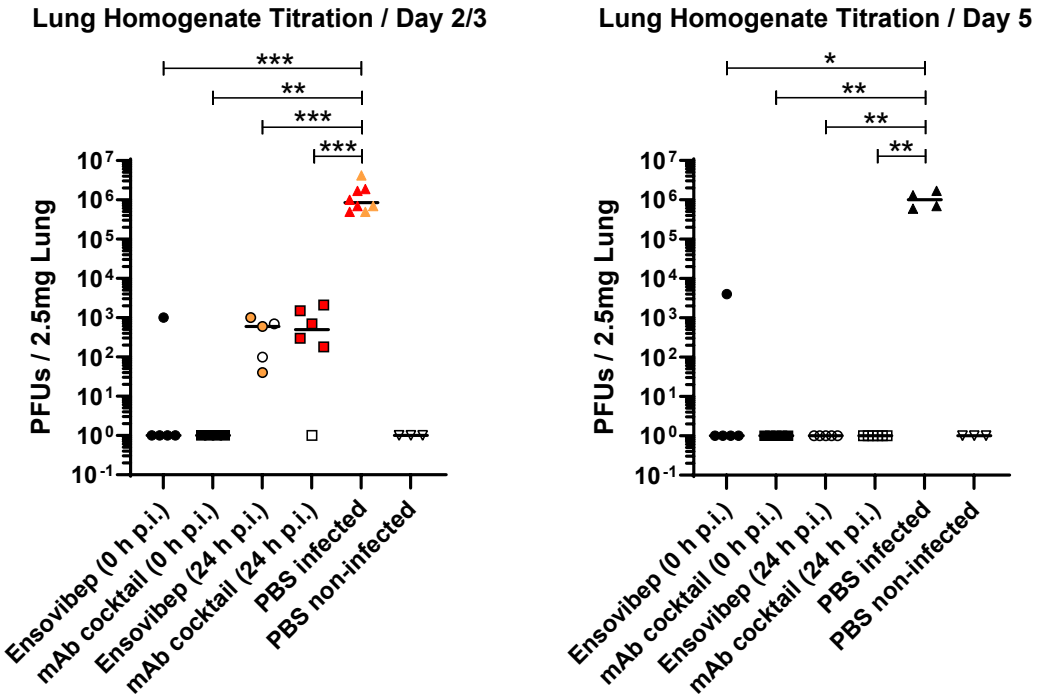

541

542 ***Figure 5:*** *A) qPCR analysis of virus gRNA copy numbers in oropharyngeal swabs and lung*
543 *homogenates at day 2/3 or day 5 p.i. B) Titration of replication competent virus from lung*
544 *homogenates as plaque assay on Vero E6 cells at day 2/3 or day 5 post infection. Red*
545 *symbols: animals taken out of the study at day 2 due to severe clinical symptoms. Orange*
546 *symbols: animals taken out of the study at day 3 due to severe clinical symptoms. Two-tailed*
547 *Mann-Whitney Test: ns P > 0.05; * P ≤ 0.05; ** P ≤ 0.01; *** P ≤ 0.001.*

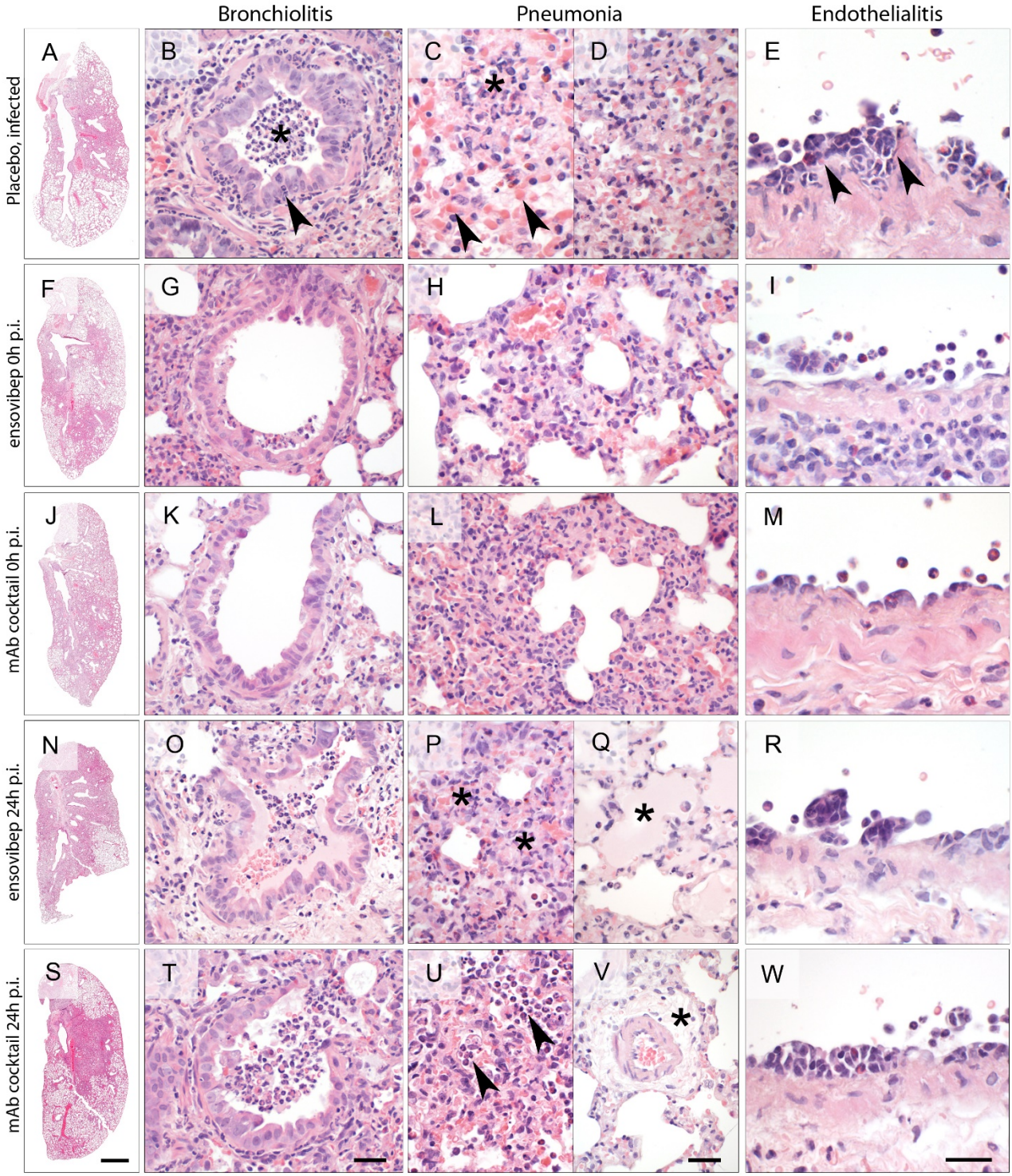
Bronchiolitis
Pneumonia
Endothelialitis
Placebo, infected
ensovibep 0h p.i.
mAb cocktail 0h p.i.
ensovibep 24h p.i.
mAb cocktail 24h p.i.
A
B
C
D
E
F
G
H
I
J
K
L
M
N
O
P
Q
R
S
T
U
V
W

548

X

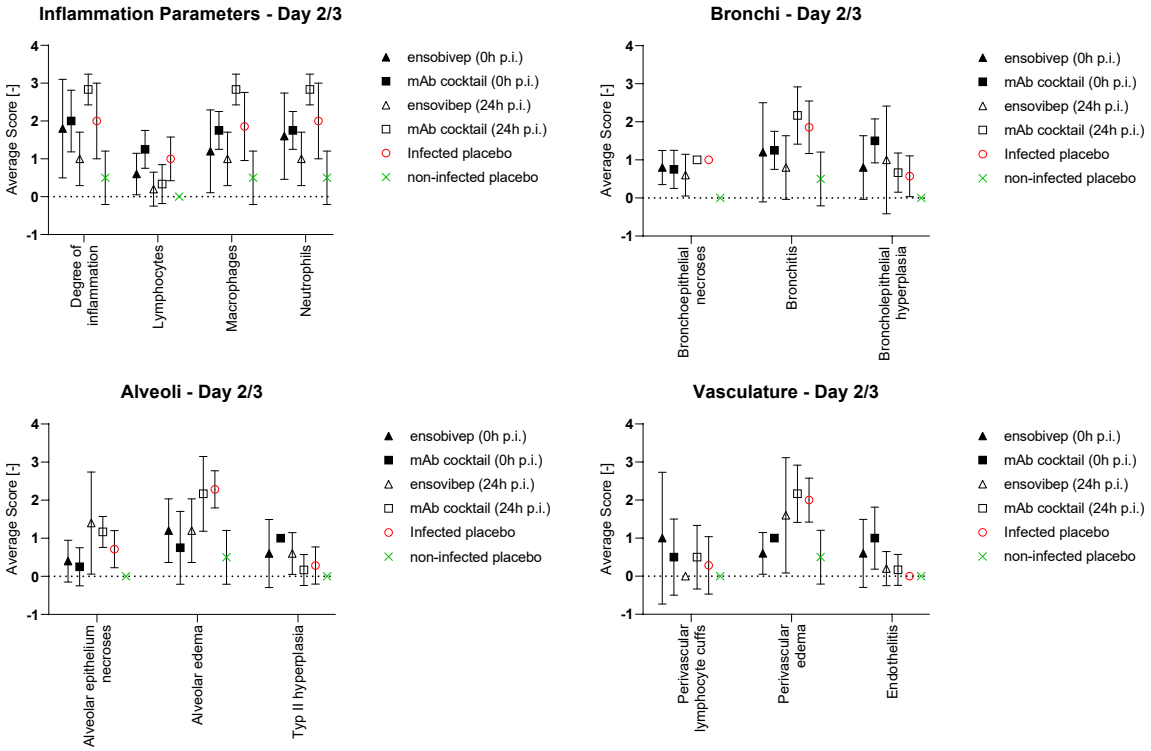
Inflammation Parameters - Day 2/3
Bronchi - Day 2/3
Alveoli - Day 2/3
Vasculature - Day 2/3
Average Score [-]
ensobivep (0h p.i.)
mAb cocktail (0h p.i.)
ensovibep (24h p.i.)
mAb cocktail (24h p.i.)
Infected placebo
non-infected placebo
Degree of inflammation
Lymphocytes
Macrophages
Neutrophils
Bronchoepithelial necroses
Bronchitis
Bronchoepithelial hyperplasia
Alveolar epithelium necroses
Alveolar edema
Typ II hyperplasia
Perivascular lymphocyte cuffs
Perivascular edema
Endothelitis

Y

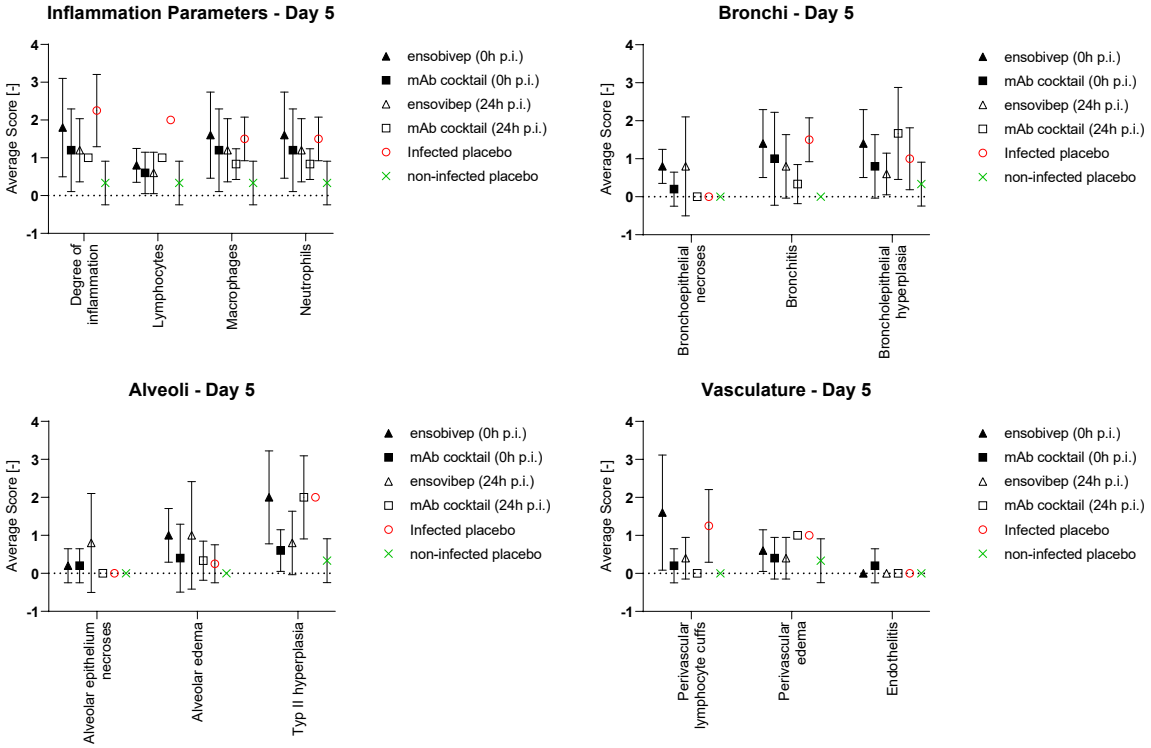
Inflammation Parameters - Day 5
Bronchi - Day 5
Alveoli - Day 5
Vasculature - Day 5
Average Score [-]
ensobivep (0h p.i.)
mAb cocktail (0h p.i.)
ensovibep (24h p.i.)
mAb cocktail (24h p.i.)
Infected placebo
non-infected placebo
Degree of inflammation
Lymphocytes
Macrophages
Neutrophils
Bronchoepithelial necroses
Bronchitis
Bronchoepithelial hyperplasia
Alveolar epithelium necroses
Alveolar edema
Typ II hyperplasia
Perivascular lymphocyte cuffs
Perivascular edema
Endothelitis

553 ***Figure 6:*** *A-W. Lung histopathology of Roborovski dwarf hamsters at 2 or 3 days p.i. with*
554 *SARS-CoV-2, hematoxylin and eosin stain. (A-E) Lungs of untreated hamsters at 3 days p.i.*
555 *developed marked inflammation with lesion patterns as described earlier. (A) Whole slide scan*
556 *revealing consolidation of approximately 60% of the left lung. (B) Untreated hamsters had*
557 *moderate necro-suppurative and hyperplastic bronchiolitis with intraluminal accumulation of*
558 *neutrophils and cellular debris (asterisk) as well as neutrophils transmigrating through the*
559 *bronchial epithelium into the lumen (arrowhead). The lung parenchyma presented with a*
560 *patchy distribution of acute necrosis (C, asterisk) with microvascular thrombosis (arrowheads)*
561 *or (D) with areas of dense infiltration by macrophages and neutrophils. (E) Pulmonary blood*
562 *vessels had mild to moderate endothelialitis. (F-I) In contrast, lungs of hamsters treated with*
563 *ensovibep on the day of infection developed (F) slightly less consolidation of their lungs. (G)*
564 *Bronchiolitis was milder with less inflammatory cell infiltrate compared to the untreated group.*
565 *Neutrophils were mostly absent. (H) Alveolar walls were only moderately expanded by*
566 *neutrophils and macrophages with less alveolar edema and hemorrhage compared to*
567 *untreated hamsters. (I) Endothelialitis was virtually absent with marginating neutrophils as only*
568 *immune cells interacting with the vascular lining. (J-M) Hamsters treated with the antibody*
569 *cocktail at the day of infection developed lesions that were similar to those as described for*
570 *the ensovibep treated group.*

571 *(N-W) In contrast, lungs of hamsters treated at 1 dpi had lesions similar to the untreated*
572 *hamsters at that time, regardless of their treatments. (O, T): Both treatment groups developed*
573 *moderate bronchiolitis similar to the untreated group. (P, U): Lung parenchyma were*
574 *characterized by interstitial (asterisks) and alveolar (arrowheads) infiltration with neutrophils*
575 *and macrophages with variable necrosis of alveolar epithelial cells. Additional lesions in both*
576 *treatment groups included (Q) moderate to marked alveolar edema (asterisk), here shown for*
577 *the ensovibep group, and (V) moderate interstitial edema (asterisk), here shown for the*
578 *antibody group. (R, W): Both treatment groups developed moderate endothelialitis with*
579 *monomorphonuclear infiltrates underneath detached endothelial cells, similar to the untreated*
580 *group.*

581 *Scale bars: A, F, J, N, S = 1 mm; B, G, K, O, T = 50 µm; C, D, H, L, P, Q, U, V = 20 µm; E, I,*
582 *M, R, W = 20 µm*

583 *Histopathologic lesions were scored semi-quantitatively and scores plotted as graphs for*
584 *histologic signs of general inflammation and histologic parameters of bronchiolar, alveolar and*
585 *vascular lesions at day 2/3 p.i (X) or day 5 p.i. (Y).*

586

587

588

589

590

591

592

593

594

595

596 Supplementary Materials for

597

598 Ensovibep, a novel trispecific DARPin candidate that

599 protects against SARS-CoV-2 variants

600

601 Rothenberger et al. 2021

602 # Materials and Methods

603 *Generation of His-tagged monovalent RBD binders and ensovibep*

604 DARPin constructs selected and cloned as described in Walser et al.[31] were transformed in *E.coli* BL21
605 cells, plated on LB-agar (containing 1% glucose and 50 µg/mL ampicillin) and then incubated overnight
606 at 37°C. A single colony was picked into TB medium (containing 1% glucose and 50 µg/mL ampicillin)
607 and incubated overnight at 37°C, shaking at 230 rpm. Fresh TB medium (containing 50 µg/mL ampicillin)
608 was inoculated with 1:20 of overnight culture and incubated at 37°C at 230 rpm. At OD600 = 1.1 the
609 culture was induced by addition of IPTG (0.5 mM final concentration) and incubated further for 5 h at
610 37°C and 230 rpm. Harvest was done by centrifugation (10 min, 5000 x g). After cell disruption by
611 sonication, primary recovery was done by heat treatment for 30 min at 62.5°C and subsequent
612 centrifugation (15 min, 12000 x g). 20 mM Imidazole and 1% Triton X-100 was added to the supernatant
613 and the 0.22 µm filtered supernatant was further purified by immobilized metal affinity
614 chromatography (IMAC) (HisTrap FF crude, Cytiva, Sweden) using the N-terminal His-tag and including
615 a wash step with 1% Triton X-100 and a step elution with 250 mM Imidazole. In a subsequent step, the
616 elution fraction of the IMAC step was applied on a size exclusion chromatography (Superdex 200, Cytiva,
617 Sweden) and fractions of interest were pooled and concentrated. Finally, the concentrated sample was
618 filtered through a 0.22 µm Mustang E filter for Endotoxin removal and sterile filtration and quality
619 controlled.

620 *Cryo-electron microscopy*

621 4 µl of purified S-ectodomain (9 µM) was mixed with 1 µl of 50 µM mono-DARPin R2, and incubated for
622 15 seconds at room temperature. 3 µl of sample was then dispensed on Quantifoil R1.2/1.3 200-mesh
623 grids (Quantifoil Micro Tools GmbH) that had been freshly glow discharged for 30 s at 20 mA. Grids
624 were blotted using blot force +2, for 5 s using Whatman No. 1 filter paper and immediately plunge-
625 frozen into liquid ethane cooled by liquid nitrogen using a Vitrobot Mark IV plunger (Thermo Fisher
626 Scientific) equilibrated to ~95% relative humidity, 4°C. Movies of frozen-hydrated specimens were
627 collected using Glacios Cryo-TEM (Thermo Fisher Scientific) operating at 200 keV and equipped with a
628 Falcon 4 Direct Electron Detector (Thermo Fisher Scientific). For additional analysis of monovalent
629 DARPin R2, 4 µl of purified S-ectodomain (18 µM) was mixed with 1 µl of 100 µM DARPin, and incubated
630 for 60 s at room temperature. Grids were prepared as described above, and movies were collected
631 using a Titan Krios Cryo-TEM (Thermo Fisher Scientific) operating at 300 keV and equipped with a Falcon
632 4 Direct Electron Detector (Thermo Fisher Scientific). All cryo-EM data were acquired using the EPU 2
633 software (Thermo Fisher Scientific) with a 30-degree stage tilt to account for preferred orientation of

634 the samples. Movies were collected in electron counting mode at 92,000x (Glacios) or 75,000x (Titan
635 Krios), corresponding to a pixel size of 1.1 Å/pix or 1.045 Å/pix over a defocus range of -1.25 to -2.5 µm.

636 *Image processing*

637 Movie stacks were manually inspected and then imported in Relion version 3.1[60]. Drift and gain
638 correction were performed with MotionCor2[61], and GCTF[62] was used to estimate the contrast transfer
639 function for each movie. Particles were automatically picked using the Laplacian-of-Gaussian (LoG)
640 algorithm and then Fourier binned (2 x 2) particles were extracted in a 160-pixel box. The extracted
641 particles were subjected to two rounds of 2D classification, ignoring CTFs until the first peak. Using the
642 'molmap' command in UCSF chimera[63], a SARS-CoV-2 spike structure (PDB ID: 6VSB)[64] was used to
643 generate a 50Å resolution starting model for 3D classification. Particles selected from 2D classification
644 were subject to a single round of 3D classification (with C1 symmetry). Particles belonging to the best
645 classes were re-extracted unbinned in a 320-pixel box, 3D auto-refined (with C1 or C3 symmetry) and
646 post-processed. Iterative rounds of per particle defocus estimation, 3D auto-refinement and post-
647 processing were used to account for the 30-degree stage tilt used during data collection. When CTF
648 refinement did not yield any further improvement in resolution, Relion's Bayesian polishing procedure
649 was performed on the particle stacks, with all movie frames included, followed by 3D auto-refinement
650 and post-processing. Subsequently, additional rounds of per particle defocus estimation, 3D auto-
651 refinement and post-processing were performed on the polished particles until no further
652 improvement in resolution or map quality was observed. The nominal resolution for each map was
653 determined according to the 'gold standard' Fourier shell correlation (FSC) criterion (FSC = 0.143) and
654 local resolution estimations were performed using Relion. Map sharpening was performed using
655 DeepEMhancer[65] as implemented in COSMIC2[66]. To improve the quality of the mono-DARPin R2 density
656 in the fully open spike reconstruction, a focused 3D classification approach was employed. Briefly, each
657 particle contributing to the final C3-symmetry–imposed reconstruction was assigned three orientations
658 corresponding to its symmetry related views using the "relion_particle_symmetry_expand" tool. A soft
659 mask was placed over the map to isolate the mono-DARPin R2-bound RBD, and the symmetry-
660 expanded particles were subjected to masked 3D classification without alignment using a regularization
661 parameter ('T' number) of 20. Particles corresponding to the 3D class with the best resolved DARPin
662 density were re-extracted in a 200-pixel box and centered on the mask used for focused classification.
663 In conjunction with this, the signal for the protein outside the masked was subtracted. The re-extracted
664 particles were then 3D auto-refined (with C1 symmetry) using local angular searches (1.8 degrees) and
665 sharpened using DeepEMhancer[65]. Three copies of the locally refined map were aligned to the globally
666 refined map using the UCSF Chimera 'fit in map' tool and resampled using the 'vop resample' command.

667 Finally, a composite map was generated using the "vop add" command. An overview of the image
668 processing workflows is shown in supplementary Figure 2A.

669 *Molecular modeling of mono and multivalent DARPin molecules*

670 Homology models of monovalent DARPin molecules R1, R2 and R3 were generated with Rosetta[67-69].
671 The consensus designed ankyrin repeat domain PDB ID:2XEE was used as template. Mutations were
672 introduced with RosettaRemodel with fixed backbone, and the structure was refined with RosettaRelax.
673 Forty refined structures were clustered using RosettaCluster with 0.3 Å radius, and the lowest-energy
674 model from the largest cluster served as the final model. The UCSF Chimera 'fit in map' tool was used
675 to fit the monovalent DARPin R2 model into the cryo-EM map produced from focused refinement. This
676 fitted model of DARPin R2, together with the RBD domain (PDB ID:6M0J) was further refined with
677 Rosetta. The structure was pre-relaxed for docking and served as input for local, high-resolution docking
678 with RosettaDock with fixed backbone. Five hundred models were generated and clustered with 1 Å
679 radius (RosettaCluster). Two largest clusters were inspected and the lowest-energy model from more
680 conserved group (i.e., with lower rigid-body perturbation from the input structure) was taken further
681 for additional all-atom refinement with RosettaRelax, with protocol optimized for interfaces
682 (InterfaceRelax2019). Fifty models were generated, and the lowest scoring model was selected. This
683 model was used to describe the interactions between DARPin R2 and the RBD. The PDB file with the
684 coordinates of the trimer of DARPin R2:RBD was used as an input structure for the conceptual modeling
685 of ensovibep bound to the spike ectodomain as shown in Figure 1G. The linkers were generated using
686 Rosetta modeling tools. Figures were generated using LigPlot[70], UCSF Chimera[63], UCSF ChimeraX[71],
687 PyMOL (The PyMOL Molecular Graphics System, Version 2.0, Schrödinger, LLC) and BioRender
688 (BioRender.com).

689 *Generation of monoclonal antibodies*

690 Publicly available sequences of variable domains from monoclonal antibodies were used to synthetize
691 the corresponding cDNA fragments and cloned into a proprietary expression vector at Evitria AG
692 (Schlieren, Switzerland). Generated vectors containing the constant immunoglobulin chains were used
693 for transfection in Chinese hamster ovary cells by Evitria. Sterile filtered cell supernatants were purified
694 via affinity purification with HiTrap MabSelect column followed by a size exclusion chromatography
695 using HiLoad 26/600 Superdex 200 column in PBS pH7.4. Selected fractions were pooled and quality
696 controlled (by SDS-PAGE, size exclusion chromatography and endotoxin measurement) before use in
697 assays.

698 *VSV-SARS-CoV-2 pseudotype mutation-vector generation*

699 Plasmid pCAGGS containing the spike protein of SARS-CoV-2[31] was used as template for generation of
700 single and multiple spike protein mutants. Forward and reverse complementary primers encoding the
701 mutation were synthesized by Microsynth (Balgach, Switzerland). High-fidelity Phusion polymerase
702 (New England Biolabs, USA) was used for all DNA amplification.

703 Single mutations of the spike protein were generated via two PCR fragments of the spike ORF using
704 high-fidelity Phusion polymerase (New England Biolabs, USA). The first fragment was generated via a
705 generic forward primer (pCAGGS-5) annealing upstream of the spike ORF and the specific reverse
706 primer encoding the mutation. The second fragment was generated using the specific forward primer
707 encoding the mutation and a reverse primer (rbglobpA-R). The two fragments were gel-purified and
708 used as input for an assembly PCR without addition of flanking primers.

709 For multi-mutation spike proteins, a complementary pair of primers (forward and reverse) encoding
710 each mutation was designed. Fragment 1 was generated with forward primer pCAGGS-5 and reverse
711 primer encoding mutation 1. Fragment 2 was generated using forward primer encoding mutation 1 and
712 reverse primer encoding mutation 2. All subsequent fragments were generated analogously. DNA
713 fragments were gel-purified and mixed in equimolar amounts. This mix was used for re-assembly of the
714 full spike ORF using outer primers pCAGGS-5 and rbglobpA-R.

715 For both single as well as multi-mutation spike protein, the full-length spike ORF was isolated from an
716 agarose gel, digested by restriction enzymes NheI/EcoRI and inserted into the pCAGGS vector
717 backbone. The correct sequence was verified via sequencing the whole ORF of the spike protein by
718 Microsynth (Balgach, Switzerland).

719 *VSV-SARS-CoV-2 pseudotype neutralization assay for mutational analysis*

720 The pseudotype viral system was based on the recombinant VSV*ΔG-Luc vector in which the
721 glycoprotein gene (G) had been deleted and replaced with genes encoding green fluorescent protein
722 and luciferase[72]. Pseudoviruses were generated as reported previously[73,74]. For the neutralization assay,
723 an initial dilution of the compounds was followed by three-fold dilutions in quadruplicates in DMEM-2
724 % [vol/vol] FCS supplemented with 20 µM human serum albumin (CSL Behring). The mixture was mixed
725 with an equal volume of DMEM-2 % FCS containing 250 infectious units (IU) per well of SARS-CoV-2
726 pseudoviruses and incubated for 90 min at 37°C. The mix was inoculated onto Vero E6 cells[75,76] in a
727 clear bottom white walled 96-well plate during 90 min at 37°C. The inoculum was removed and fresh
728 medium added, and cells further incubated at 37°C for 16 h. Cell were lysed according to the ONE-Glo™
729 luciferase assay system (Promega, Madison, US) and light emission was recorded using a Berthold®

730 TriStar LB941 luminometer. The raw data (relative light unit values) were exported to GraphPad Prism
731 v8.4.3, and the % neutralization values were normalized to the untreated PsV signal. IC_{50} with 95%
732 confidence interval were estimated by model of nonlinear regression fit with settings for log (inhibitor)
733 vs normalized response curves. Data points are plotted by the mean ± SEM (standard error of mean).

734 SARS-CoV-2 lentivirus-based pseudovirus neutralization assay

735 The neutralizing activity of therapeutic antibodies against SARS-COV-2 variants was measured using
736 lentiviral particles pseudotyped with spike proteins of SARS-COV-2 variants, as previously described[77].
737 Briefly, pseudoviruses bearing the spike proteins and carrying a firefly luciferase [78] reporter gene were
738 produced in 293T cells by co-transfection of pCMVΔR8.2, pHR'CMVLuc and pCDNA3.1-spike variants.
739 Plasmids encoding human codon-optimized spike genes with the desired mutations were purchased
740 (GenScript, Piscataway, NJ). Supernatants containing pseudoviruses were collected 48 h post-
741 transfection, filtered through a 0.45 µm low protein binding filter, and stored at -80°C. Pseudovirus
742 titers were measured by infecting 293T-ACE2.TMPRSS2s cells for 48 h prior to measuring luciferase
743 activity (luciferase assay reagent, Promega, Madison, WI). For neutralization assays, pseudoviruses with
744 titers of approximately 10^6 relative luminescence units (RLU)/ml were incubated with serially diluted
745 antibodies for two h at 37°C before adding the pseudovirus and antibody mixtures (100 µL) onto 96
746 well plates pre-seeded one day earlier with 3.0 x 10^4 293T-ACE2.TMPRSS2s cells/well. Pseudovirus
747 infection was scored 48 h later by measuring luciferase activity. The therapeutic concentration causing
748 a 50% reduction of RLU compared to control (ID_{50}) was reported as the neutralizing antibody titer. Titers
749 were calculated using a nonlinear regression curve fit (GraphPad Prism software Inc., La Jolla, CA). The
750 ratio of the neutralizing antibody titer of the variant compared to the neutralizing antibody titer of wild
751 type was calculated. The mean titer from at least two independent experiments with intra-assay
752 duplicates was reported as the final titer. This work was performed independently by investigators at
753 the US Food and Drug Administration, Center for Biologics Evaluation and Research as part of
754 Therapeutics Research Team for the US government COVID-19 response efforts.

755 *Cells and pathogenic virus*

756 Vero E6 cells (kindly provided by Prof. Volker Thiel, University of Bern, Switzerland) were passaged in
757 Minimum Essential Medium (MEM) (Cat N° M3303) containing 10% fetal bovine serum (FBS) and
758 supplements (2 mM L-Glutamine, 1% Non-essential amino acids, 100 units/ml Penicillin, 100 µg/ml
759 Streptomycin, 0.06% Sodium bicarbonate, all from Bioswisstec, Schaffhausen, Switzerland) at 37°C,
760 >85% humidity and 5% CO_2. Vero E6/TMPRSS2 cells[75,76] obtained from the Centre For AIDS Reagents
761 (National Institute for Biological Standards and Control) were passaged in Dulbecco's Modified Eagle
762 Medium (DMEM) (Cat N° M1452) containing 10% fetal bovine serum (FBS) and supplements (2 mM L-

763 Glutamine, 1% Non-essential amino acids, 100 U/mL Penicillin, 100 µg/mL Streptomycin, 0.06% Sodium
764 bicarbonate and 2% Geneticin G418, all from Bioswisstec, Schaffhausen, Switzerland) at 37°C, >85%
765 humidity and 5% CO_2.

766 SARS-CoV-2 (2019-nCoV/IDF0372/2020), kindly provided by Dr. Sylvie van der Werf from the National
767 Reference Centre for Respiratory Viruses hosted by Institut Pasteur (Paris, France) was propagated in
768 Vero E6 cells in MEM containing 2% FBS and supplements (2%-FBS-MEM) at 37°C, >85% humidity and
769 5% CO_2. SARS-CoV-2 variants (B.1.1.7, B.1.351 and P.1) were provided from University Hospital of
770 Geneva, Laboratory of Virology [25] and propagated in Vero E6/TMPRSS2 cells in DMEM containing 2%
771 FBS and supplements (2%-FBS-DMEM) at 37°C, >85% humidity and 5% CO_2. Viral titer was determined
772 by standard plaque assay, by incubating 10-fold serial dilutions of the virus for 1 h at 37°C on a confluent
773 24-well plate with Vero E6 cells. Then inoculum was removed and 1 mL overlay medium (20 ml
774 Dulbecco's Modified Eagle's Medium, 5 ml FBS, 100 U/mL Penicillin, 100 µg/mL Streptomycin, and 25
775 ml Avicel rc581) was added. After 3 days incubation at 37°C the overlay was removed and the plates
776 stained with crystal violet solution (spatula tip (~4 mg) crystal violet powder (Sigma Aldrich) solved in
777 30 ml 37% formalin and 120 mL PBS (Sigma Aldrich).

778 *Viral passaging experiment with authentic SARS-CoV-2*

779 Virus escape studies were adapted from a previously published protocol by Baum et al.[27]. Briefly, 1:5
780 serial dilutions of DARPin molecules and monoclonal antibodies from 100 µg/mL to 0.032 µg/mL were
781 prepared in Minimum Essential Medium (MEM) containing 2% FBS, supplements and 10 µM human
782 serum albumin (HSA; CSL Behring, Switzerland; 2%-FBS-MEM + HSA). 500 µL of virus suspension
783 containing 1.5 x 10^6 plaque forming units (pfu) SARS-CoV-2 in 2%-FBS-MEM + HSA were mixed with 500
784 µL of serially diluted DARPin molecules or monoclonal antibodies and subsequently incubated for 1
785 hour at 37°C. The mixtures were then transferred to confluent Vero E6 cells in 12 well plates and
786 incubated for 4 days at 37°C, >85% humidity and 5% CO_2. Each culture well was assessed for cytopathic
787 effect (CPE) by microscopy. Supernatant was removed from wells with the highest DARPin or antibody
788 concentrations showing significant CPE (≥20%) and used for total RNA extraction and further passaging.
789 For subsequent rounds of passaging, remaining 900 µL supernatant of selected wells was diluted in 4
790 mL in 2%-FCS-MEM + HSA and from the 4.9 mL, 500 µL mixed with serial dilutions of DARPin molecules
791 or antibodies, incubated and the mixture transferred to 12-well plates with fresh Vero E6 cells as
792 described above. Cell culture wells were assessed for CPE again after 4 days and the supernatant of
793 wells with highest DARPin or antibody concentrations with evident viral replication (CPE) harvested and
794 used for additional passages. A total of 4 passages were performed this way.

795

796 Deep sequencing of viral passages

797 RNA of the cell culture supernatant was extracted using the RNeasy Universal Plus kit (Qiagen, Basel,
798 Switzerland) according to the manufacturer's protocol. 10.5 µL of the extract was reverse transcribed
799 using Superscript VILO (ThermoFisher Scientific, Reinach, Switzerland) following the manufacturer's
800 instructions. Barcoded libraries were prepared on the Ion Chef Instrument (ThermoFisher Scientific)
801 using the Ion AmpliSeq SARS-CoV-2 Research Panel (ThermoFisher Scientific). 8-16 barcoded samples
802 were pooled and loaded on one Ion 530 chip using the Ion Chef Instrument (ThermoFisher Scientific)
803 and sequenced on the Ion S5 System with 550 flows.

804 The resulting BAM files were converted to fastq format using Samtools 1.10[79] and subjected to adapter
805 and quality trimming using Trimmomatic 0.39[80] (options: ILLUMINACLIP:adapters.fasta:2:30.10,
806 LEADING: 3, TRAILING: 3, SIDINGWINDOW:4:15, MINLEN:36). Reads were aligned to the SARS-CoV-2
807 reference genome (NC_045512.2) using bwa 0.7.17[81] and variants were determined using LoFreq
808 v2.1.5[82]. Variants were filtered for a minimal depth (DP) of 400X and a minimal allele frequency (AF) of
809 3% using bcftools 1.10[79]. Functional annotation of the variants was performed using SNPEff 5.0[83].
810 Variants were visualized in R 3.6.1 using ComplexHeatmap 2.2[84].

811 *Virus neutralization of authentic wild type and variants of SARS-CoV-2 determined by Cell Titer-Glo*

812 Virus neutralization capacity of mono-valent DARPin candidate and multispecific DARPin molecules was
813 determined for 100 $TCID_{50}$ SARS-CoV-2 variants from lineage B.1.1.7 (H69_V70del, Y145del, N501Y,
814 A570D, D614G, P681H, T716I, S982A, D1118H), B.1.351 (L18F, D80A, D215G, L242_L244del, T302T,
815 K417N, E484K, N501Y, D571D,D614G, A701V) and P.1 (L18F, T20N, P26S, D138Y, R190S, K417T, E484K,
816 N501Y, D614G, H655Y, T1027I, V1176F) in reference to a wild-type French isolate (with the following
817 differences to the Wuhan wild-type: V367F; E990A) by measuring ATP levels of protected cells in a cell
818 viability assay. DARPin molecules were serially diluted 1:4 from 40 nM to 2.4 pM (in triplicates) in 100
819 µL cell culture medium (2%-FBS-DMEM) supplemented with 10 µM HSA in 96 well plates. The diluted
820 DARPin antivirals were mixed with 100 $TCID_{50}$ SARS-CoV-2 in 100 µL 2%-FBS-MEM + HSA and incubated
821 for 1 h at 37°C. DARPin/virus mixtures (200 µL) were transferred onto confluent Vero E6/TMPRSS2 cells.
822 The controls consisted of cells exposed to virus suspension only, to determine maximal cytopathic
823 effect and of cells incubated with medium only, to determine baseline cell viability. The plates were
824 incubated for 3 days at 37°C, >85% humidity and 5% CO_2. Cell viability was determined by removing
825 100 µL supernatant from all wells and adding 100 µL CellTiter-Glo reagent to the cells as described in
826 the manufacturers protocol (CellTiter-Glo® Luminescent Cell Viability Assay, Promega, Madison, USA).
827 After 2 minutes shaking on an orbital shaker, lysis of the cells during 10 min and transfer to an opaque-
828 walled plate at room temperature, luminescence was read using a GloMax instrument (Promega).

829 *Surface plasmon resonance (SRP) affinity determination of ensovibep and individual RBD-binding*
830 *domains*

831 SPR assays were used to determine the binding affinity of monovalent DARPin as well as multivalent
832 DARPin molecules to the spike protein of SARS-CoV-2. All SPR data were generated using a Bio-Rad
833 ProteOn XPR36 instrument with PBS-T (0.005% Tween20) as running buffer. A new neutravidin sensor
834 chip (NLC) was air-initialized and conditioned according to Bio-Rad manual.

835 Monovalent DARPin molecules R1, R2, R3: Chemically biotinylated (via lysines) SARS-CoV-2 spike
836 protein 20 (Sino Biologics) was captured to ~3400 RUs (30 µg/mL, 30 µL/min, 300 s). Two buffer
837 injections (100 µL/min, 60 s) followed by two 12.5 mM NaOH regeneration steps (100 µL/min, 18 s)
838 were applied before the first injections. Mono-domain DARPin proteins were injected (at
839 50/16.7/5.6/1.9/0.6 nM) for 180 s at 100 µL/min for association and dissociation was recorded for
840 3600 s (at 100 µL/min). The ligand was regenerated with a 12.5 mM NaOH pulse (100 µL/min, 18 s).
841 The data was double referenced against the empty surface and a buffer injection and fitted according
842 to the 1:1 Langmuir model.

843 Multivalent DARPin molecules: Avi-tagged biotinylated SARS-CoV-2 S protein (Acro Biosystems) was
844 captured to ~1200 RUs (1.33 ug/mL, 30 µl/min, 300 s) on a precoated neutravidin chip (NLC). Two
845 buffer injections (100 µL/min, 60 s) followed by three 12.5 mM NaOH regeneration steps (100 µL/min,
846 18s) were applied before the first injections. One single concentration of 20 nM of ensovibep was
847 injected for 180 s at 100 µL/min for association and dissociation was recorded for 36'000 s (at
848 100 µL/min). The data was double referenced against the empty surface and a buffer injection. Due to
849 avidity gain, no significant dissociation could be recorded during the measured time.

850 *Surface plasmon resonance (SRP) affinity determination of wt-RBD and RBD F486V to ACE2*

851 SPR assays were used to determine the binding affinity of wt-RBD as well as RBD-F486V human ACE2
852 protein. SPR data were generated using a Bruker Sierra SPR-32 Pro instrument with PBS-T (0.005%
853 Tween20) as running buffer. A Bruker biotin tag capture sensor chip (BTC) was initialized and
854 conditioned according to Bruker manual.

855 Avi-tagged biotinylated monomeric human ACE2 (Acro Biosystems) was captured to ~170 RUs
856 (3.3 µg/mL, 10 µL/min, 60 s). SARS-CoV-2 S protein RBD (wt, Acro biosystems, 500nM-0.229nM,
857 threefold dilution series) and SARS-CoV-2 S protein RBD-F486V (in-house produced, 1500nM-0.229nM,
858 threefold dilution series) were injected for 240 s at 25 µL/min for association and dissociation was
859 recorded for 300 s (at 25 µL/min). After each injection, a 15min pause was performed to ensure full

860 dissociation of analyte from the ligand. The data was double referenced against the empty surface and
861 a buffer injection and fitted according to the 1:1 Langmuir model.

862 *Roborovski dwarf hamster model for the assessment of antiviral potency of ensovibep on wild type SARS-*
863 *CoV-2 and the B.1.1.7 (alpha) variant*

864 Materials and Methods

865 1. Cells and viruses

866 For in vivo experiments, SARS-CoV-2 isolates BetaCoV/Germany/BavPat1/2020[85] and
867 BetaCoV/Germany/ChVir21652/2020 (B.1.1.7) were grown on Vero E6 cells and whole genome
868 sequenced prior to infection experiments to confirm genetic integrity. Particularly the presence and
869 integrity of the furin cleavage site in the majority of the virus population was confirmed. All virus stocks
870 were titrated on Vero E6 cells prior to infection.

871 2. Animals and infection

872 A total of 120 female and male Roborovski dwarf hamsters (Phodopus roborovskii) was used for
873 infection experiments. Animals were housed in groups of 3 to 6 animals of the same sex in individually
874 ventilated GR900 cages (Tecniplast, Buguggiate, Italy) and provided with food and water ad libitum and
875 bountiful enrichment (Carfil, Oud-Turnhout, Belgium). Infection was performed by intranasal
876 administration of $1x10^5$ pfu SARS-CoV-2 in 20 µL cell culture medium under general anesthesia[38]. All
877 animal procedures were performed in accordance with relevant institutional and legal regulations and
878 approved by the responsible state authority, Landesamt für Gesundheit und Soziales Berlin, Germany,
879 permit number G 0086/20.

880 3. Treatment

881 DARPin molecules and monoclonal antibodies were administered intraperitoneally in sterile PBS. The
882 final drug concentration was adjusted based on the desired dose and respective animal weight to a 100
883 µL injection volume. For intraperitoneal administration the animal was fixed by grasping the neck skin
884 and the back skin between thumb and fingers. Subsequently, the hand was turned over so that the
885 animal rests with its back in the palm of the hand. The head of the animal was kept downwards to
886 prevent injection/damage in/of the organs and the needle was inserted left of the median line in the
887 groin area, between the 4th and the 5th mammary gland/nipple. Finally, the needle was removed in a
888 smooth motion. All animals in this study were treated once at the indicated time point, 0, 6 or 24 hours
889 post infection.

890

891 4. Experimental groups

892 From a total of 120 Roborovski dwarf hamsters, 54 were used to determine dose and time dependency
893 of treatment success. In these cohorts, 6 animals per group were infected with $1x10^5$ pfu SARS-CoV-2
894 WT (BetaCoV/Germany/BavPat1/2020) and treated with either 3, 10 or 20 mg/kg ensovibep at the time
895 of infection, with 1 or 20 mg/kg 6 h post infection, or with 10 mg/kg 24h post infection, a placebo (PBS)
896 treatment group with 6 animals was also included in each of three studies performed for this purpose.
897 (Suppl. Figure 7)

898 To compare efficacy of ensovibep and Regeneron antibody cocktail treatment, 60 animals were
899 infected with $1x10^5$ pfu SARS-CoV-2 variant B.1.1.7 (BetaCoV/Germany/ChVir21652/2020). Subjects
900 were divided into groups of 12 animals and treated with 10 mg/kg ensovibep, 10 mg/kg Regeneron
901 mAb cocktail or a placebo (PBS) at the time of infection or with 10 mg/kg ensovibep or 10 mg/kg
902 Regeneron mAb cocktail 24 h post infection. An additional 6 animals served as non-infected control
903 group.

904 In all animal experiments performed in this study, half of each respective group was scheduled for take
905 out at 3 dpi, the other half was to be terminated at 5 dpi. In some of the experiments, several animals
906 had to be terminated at time points other than these for humane reasons. Defined humane endpoints
907 included a body temperature < 33°C, body weight loss > 15% together with signs of respiratory distress,
908 body weight loss > 20% or a combination of these factors. Animals were monitored at least twice a day
909 to prevent any prolonged suffering.

910 5. Virological analysis

911 RNA was extracted from throat swabs and lung tissue using the innuPREP Virus DNA/RNA Kit (Analytic
912 Jena, Jena, Germany). Viral RNA was quantified using a one-step RT qPCR reaction with the NEB Luna
913 Universal Probe One-Step RT-qPCR (New England Biolabs, Ipswich, MA, USA) and the 2019-nCoV RT-
914 qPCR primers and probe (E_Sarbeco)[86] on a StepOnePlus RealTime PCR System (Thermo Fisher
915 Scientific, Waltham, MA, USA) according to the manufacturer's instructions. Standard curves for
916 absolute quantification were generated from serial dilutions of SARS-CoV-2 DNA obtained from a full-
917 length virus genome cloned as a bacterial artificial chromosome and propagated in E. coli. Duplicate
918 10-fold serial dilutions were used to determine replication competent virus titers on confluent layers
919 of Vero E6 cells. To this end, serial dilutions of lung tissue homogenates were made and incubated on
920 Vero E6 monolayers for 2 hours at 37 °C. Cells were washed and overlaid with semi-solid cell culture
921 medium containing 1.5% microcrystalline cellulose (Avicel) and incubated for 48 h at 37 °C after which
922 plates were fixed with 4% formalin and stained with 0.75% crystal violet for plaque counting.

923 6. Histology

924 For histopathology, the left lung lobe was carefully removed, immersion-fixed in formalin, pH 7.0, for
925 48 h, embedded in paraffin, and cut in 2 µm sections. Slides were stained with hematoxylin and eosin
926 (HE) after dewaxing in xylene and rehydration in decreasing ethanol concentrations. Lung sections were
927 microscopically evaluated in a blinded fashion by a board-certified veterinary pathologist to assess the
928 character, distribution and severity of pathologic lesions using lung-specific inflammation scoring
929 parameters as described for other lung infection models before. Three different scores were used that
930 included the following parameters: (1) lung inflammation score including severity of (i) interstitial
931 pneumonia (ii) bronchiolitis, (iii) necrosis of bronchial and alveolar epithelial cells, and (iv) hyperplasia
932 of alveolar epithelial type II cells as well as (v) hyperplasia of bronchial epithelial cells; (2) immune cell
933 infiltration score taking into account the presence of (i) neutrophils, (ii) macrophages, and (iii)
934 lymphocytes in the lungs as well as (iv) perivascular lymphocytic cuffing; and (3) edema score including
935 (i) alveolar edema and (ii) perivascular edema. HE-stained slides were analyzed and images were taken
936 using an Olympus BX41 microscope with a DP80 Microscope Digital Camera and the cellSens™ Imaging
937 Software, version 1.18 (Olympus Corporation, Münster, Germany). For the display of overviews of
938 whole lung lobe sections, slides were automatically digitized using the Aperio CS2 slide scanner (Leica
939 Biosystems Imaging Inc., Vista, CA, USA), and image files were generated using the Image Scope
940 Software (Leica Biosystems Imaging Inc.). The percentages of lung tissues affected by inflammation
941 were determined histologically by an experienced board certified experimental veterinary pathologist
942 (O.K.) as described previously [87]. Lung inflammation scores were determined as absent, (1) mild, (2)
943 moderate or (3) severe and quantified as described previously [87]. Immune cell influx scores and edema
944 scores were rated from absent to, (1) mild, (2) moderate, or (3) severe.

945 7. Whole genome sequencing of SARS-CoV-2 isolated from treated hamsters

946 Following RNA extraction from swabs and lung samples, libraries were prepared and sequenced using
947 Illumina technology (Illumina, San Diego, California, USA). For library preparation, a multiplexed
948 amplicon-based whole-viral-genome approach using the NEBNext® ARTIC SARS-CoV-2 Library Prep Kit
949 (Illumina®) was employed (New England Biolabs, Ipswich, Massachussets, USA). Briefly, this approach
950 relies on cDNA synthesis from total RNA and amplification of target SARS-CoV-2 cDNA using the V3
951 ARTIC primers; these amplicons then undergo the usual library preparation steps for Illumina
952 sequencing (end repair, adaptor ligation and PCR enrichment). Quantification of enriched sequencing
953 libraries was performed using the NEBNext® Library Quant Kit for Illumina® (New England Biolabs,
954 Ipswich, Massachussets, USA). Libraries were then pooled and sequenced on an Illumina Miseq System
955 (Illumina, San Diego, California, USA).

956 The generated Illumina sequencing data were processed with Trimmomatic v.0.39[80] and mapped
957 against genome reference MT270101.1, using the Burrows-Wheeler aligner v.0.7.17[81]. Mapping
958 statistics were generated using Samtools v1.10[88] and alignments were visualized using IGV v2.9.4 for
959 Linux[89]. For detection of single-nucleotide polymorphisms (SNPs), Freebayes, a Bayesian genetic variant
960 detector was used. All SNPs with a minimum mapping quality of 5, minimum count of 3 and minimum
961 fraction of 0.01 were considered. Consensus sequences for each sample were obtained using BCFtools.
962 All SNP-containing open reading frame (ORFs) sequences were extracted from these consensus
963 genomes and translated using the Expasy[908]. Translate tool. The resulting protein sequences were then
964 aligned to the corresponding reference protein sequences using the Expasy[8] SIM Protein Alignment
965 tool. For SNPs that resulted in amino acid substitutions, their possible effect on protein function was
966 gauged using two predictors: PROVEAN Protein[91 92] and SIFT[93]. Results from both predictors were taken
967 into account, except on instances where the SIFT predictor could not resolve the proposed substitution
968 or made "low confidence" predictions, then PROVEAN's prediction was prioritized as its protein
969 database is larger and newer.

970 *Hamster pharmacokinetic study*

971 Single intraperitoneal injections of 10 mg/kg were administered to female hamsters. Fifteen animals
972 were enrolled in each study (n=3 per time point). Blood was sampled from individual animals at 2 h,
973 24 h, 48 h, 72 h and 168 h post administration and processed to serum. MP0420 serum
974 concentrations were determined by sandwich ELISA using an anti-DARPin antibody as capture reagent
975 and biotinylated RBD and HRP conjugated Streptavidin as detection reagent and quantified against a
976 standard curve. Serum concentrations for detection of both antibodies REGN10933 and REGN10987
977 were determined by sandwich ELISA using an anti-IgG antibody as capture reagent and biotinylated
978 RBD and HRP conjugated Streptavidin as detection reagent and using a standard curve.
979 Pharmacokinetic parameters were determined with non-compartmental analyses using the software
980 Phoenix WinNonLin (Certara, Princeton, USA) or GraphPadPrism (GraphPad Software, La Jolla,USA).
981 For the *in vivo* efficacy study, terminal bleed samples were collected at 2, 3 or 5 days p.i. according to
982 study description.

983 Supplementary Figures

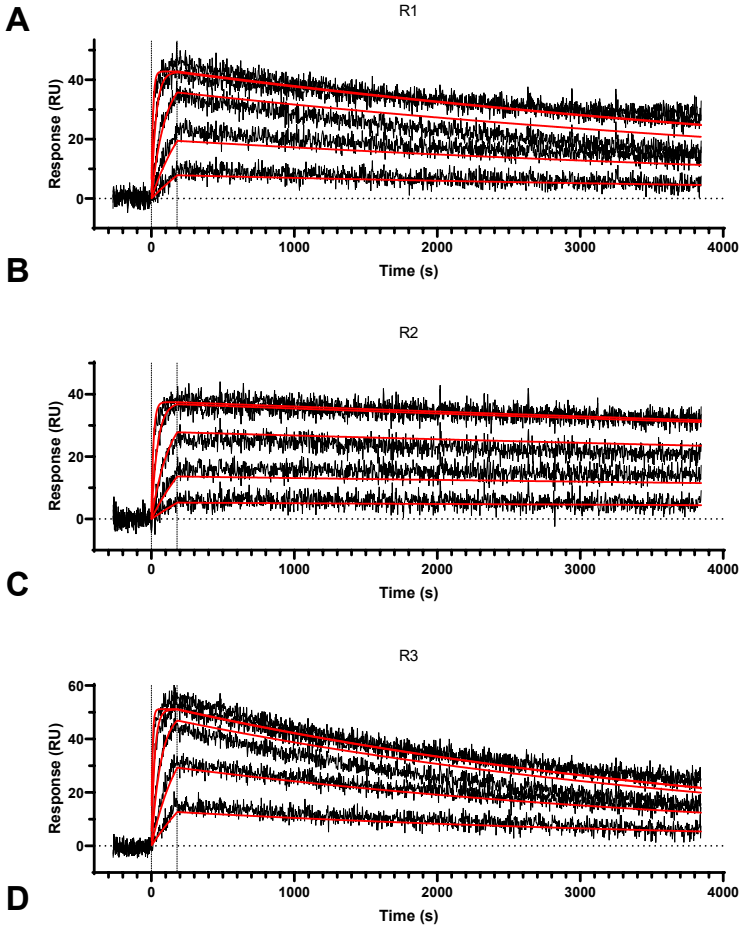

984

985

986

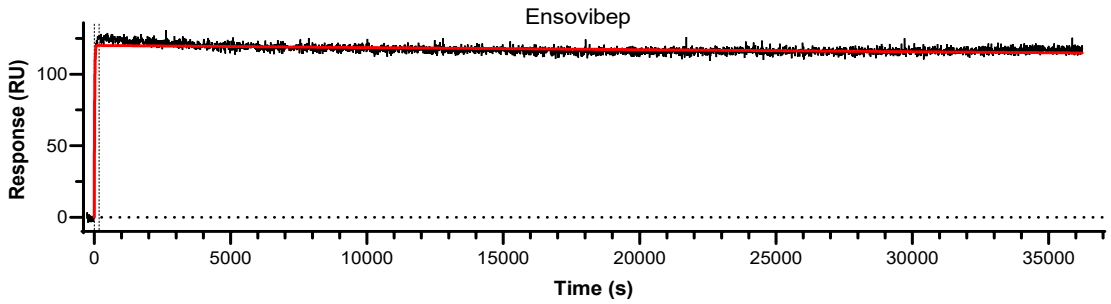

987

988 ***Supplementary Figure 1****: A-C) Surface plasmon resonance (SPR) sensorgrams of the*
989 *monovalent DARPin modules (R1, R2, R3), incorporated in ensovibep binding to immobilized*
990 *trimeric spike protein. DARPin concentrations for A-C: 50/16.67/5.56/1.85/0.62 nM.*
991 *Determined* K_D *values: A) 80 pM, B) 30 pM, C) 90 pM. D) SPR sensorgram of ensovibep*
992 *binding to immobilized spike protein. Off-rate was measured over 10 h and no physical off-*
993 *rate could be determined by SPR due to very strong avidity of the three interlinked RBD*
994 *binding modules.*

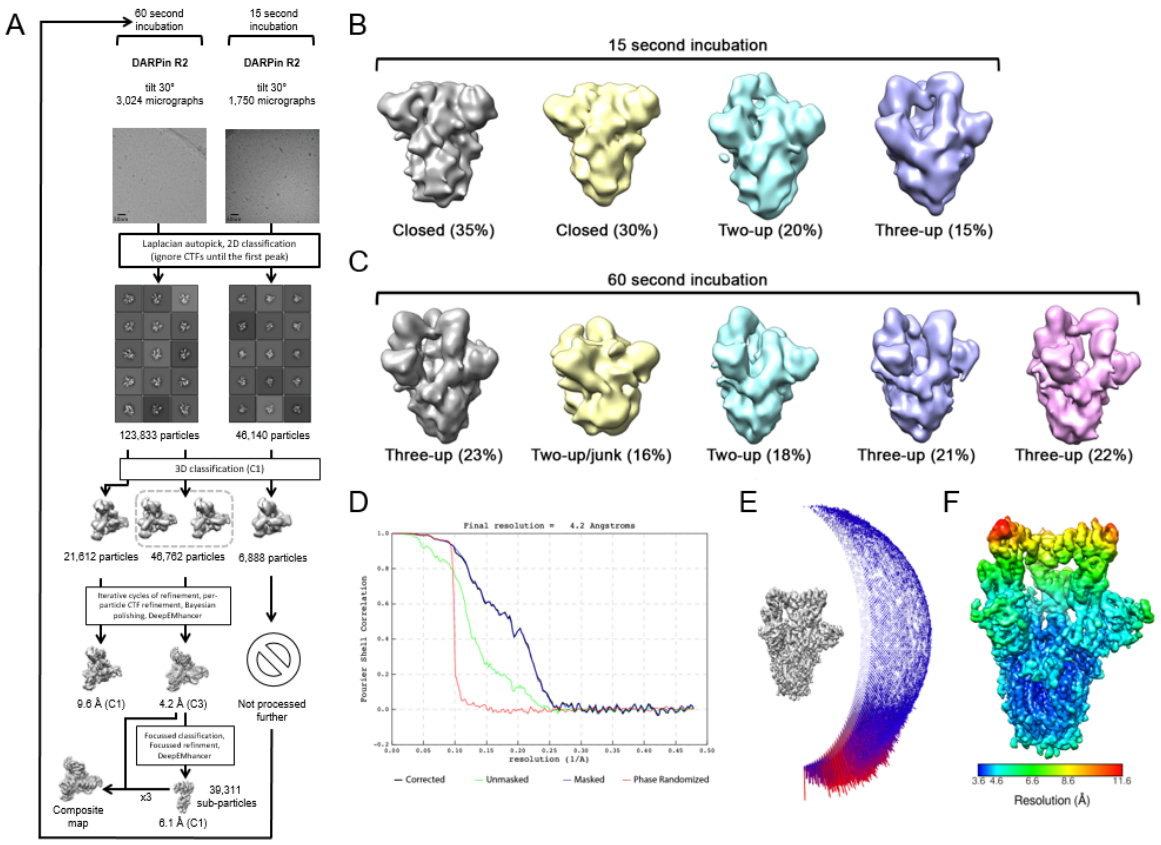

Supplementary Figure 2: Single-particle cryo-EM data processing. A) Single-particle cryo-EM image processing workflow for the monovalent DARPin R2 data collections. B) 3D classes obtained from spike ectodomains incubated with monovalent DARPin R2 for 15 seconds, and C) for 60 seconds. D) Gold-standard Fourier shell correlation (FSC) curve generated from the independent half maps contributing to the 4.2 Å resolution density map. E) Angular distribution plot of the final C3 refined EM density map. F) The EM density map of the spike ectodomain bound to three copies of monovalent DARPin R2, colored according to local resolution.

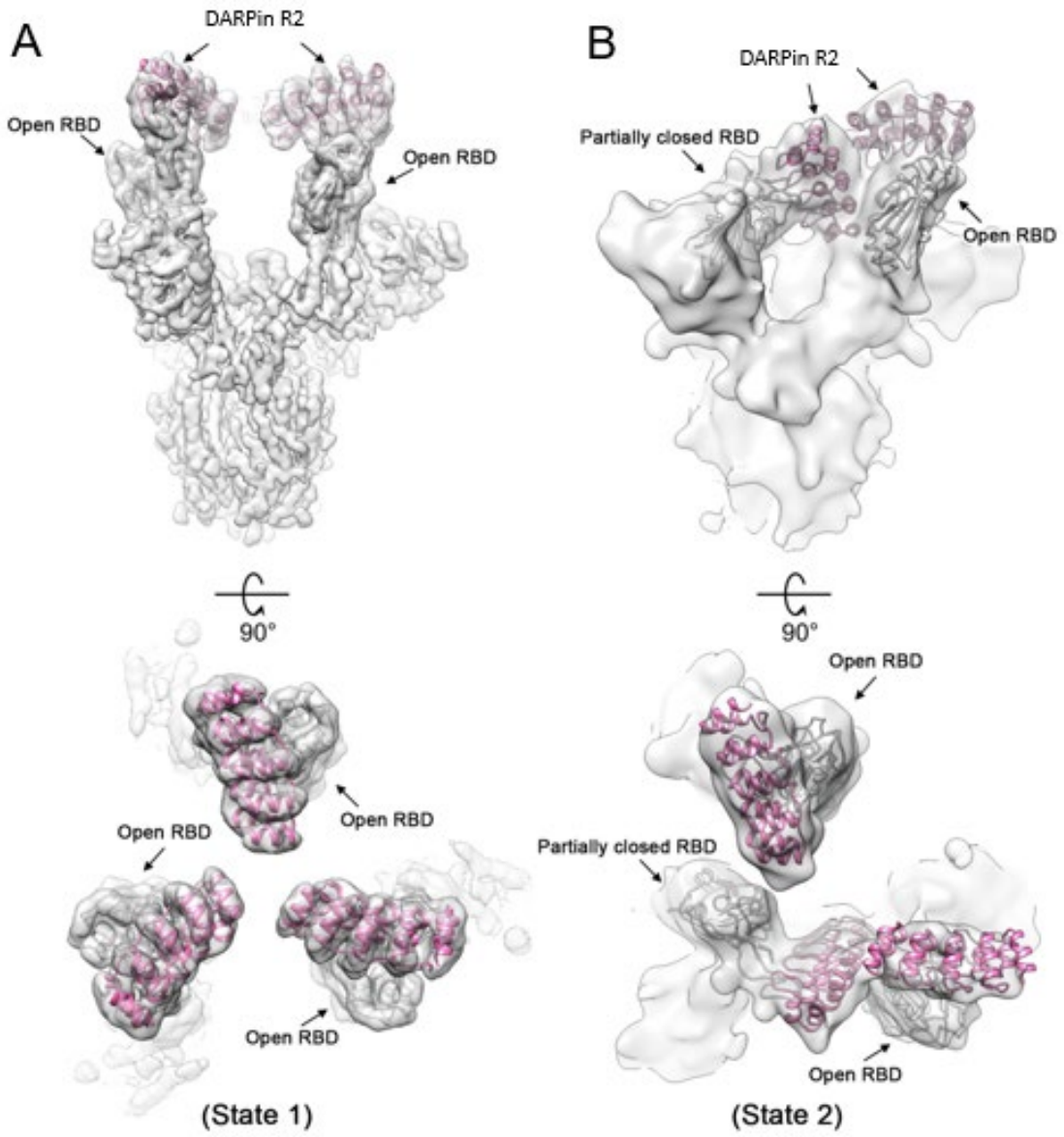

1005

1006 **Supplementary Figure 3: Monovalent DARPin R2 prevents full closure of the RBD.** A)
1007 Cryo-EM density for state 1 and B) state 2 of the SARS-CoV-2 spike ectodomain in complex
1008 with the RBD targeting monovalent DARPin R2, shown as two orthogonal views. The pseudo-
1009 atomic model of monovalent DARPin R2 in complex with RBD, derived from molecular docking
1010 experiments, is fitted in each of the spike protomers and colored grey and pink, respectively.

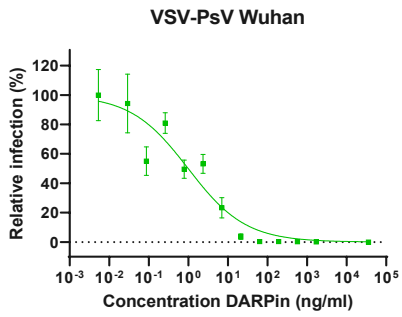
VSV-PsV Wuhan
Relative infection (%)
Concentration DARPin (ng/ml)

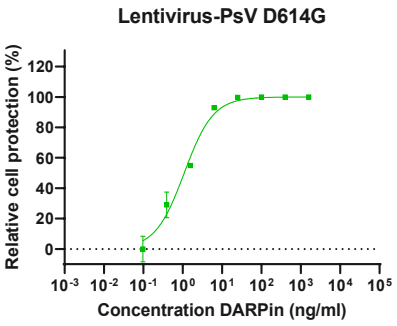
Lentivirus-PsV D614G
Relative cell protection (%)
Concentration DARPin (ng/ml)

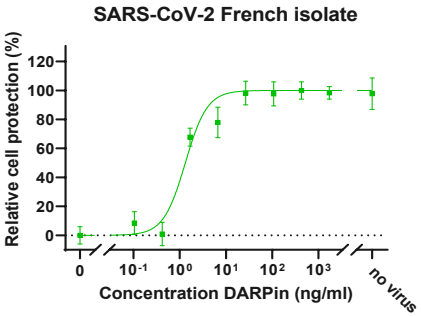
SARS-CoV-2 French isolate
Relative cell protection (%)
Concentration DARPin (ng/ml)
no virus

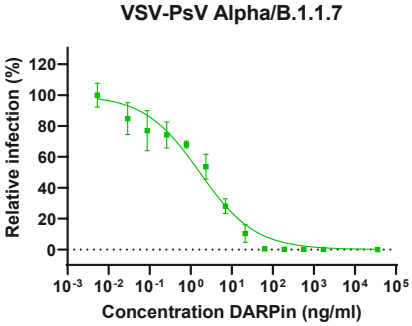
VSV-PsV Alpha/B.1.1.7
Relative infection (%)
Concentration DARPin (ng/ml)

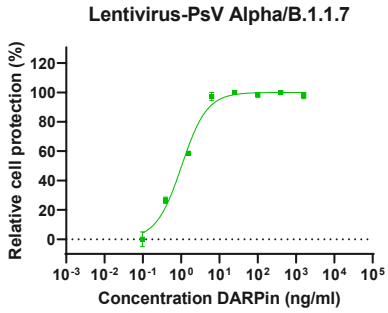
Lentivirus-PsV Alpha/B.1.1.7
Relative cell protection (%)
Concentration DARPin (ng/ml)

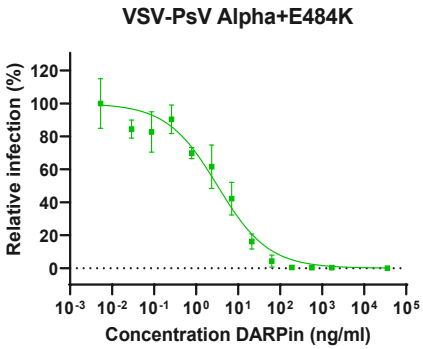
VSV-PsV Alpha+E484K
Relative infection (%)
Concentration DARPin (ng/ml)

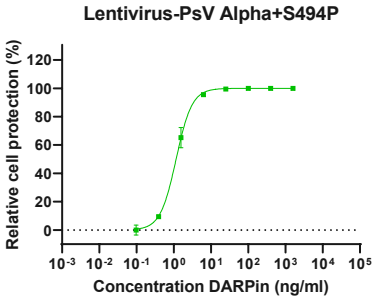
Lentivirus-PsV Alpha+S494P
Relative cell protection (%)
Concentration DARPin (ng/ml)

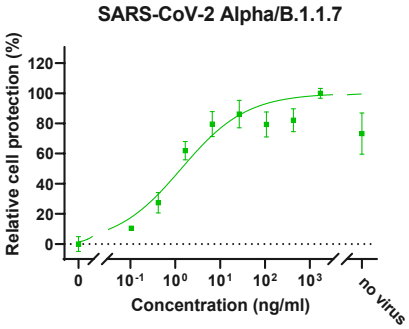
SARS-CoV-2 Alpha/B.1.1.7
Relative cell protection (%)
Concentration (ng/ml)
no virus

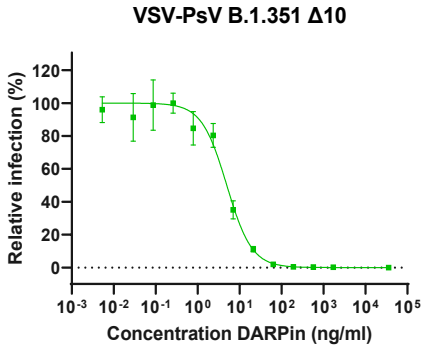

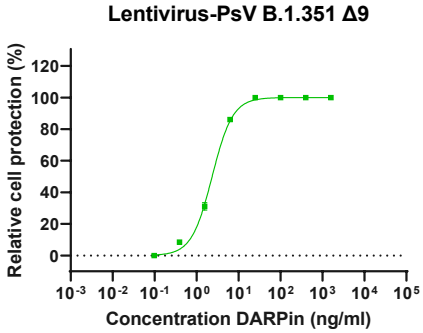

1015

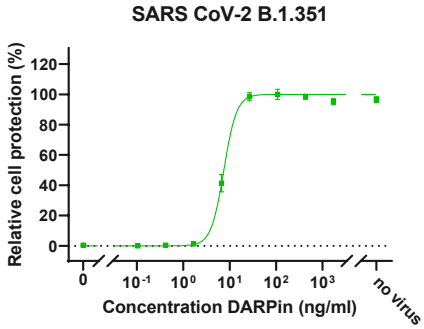

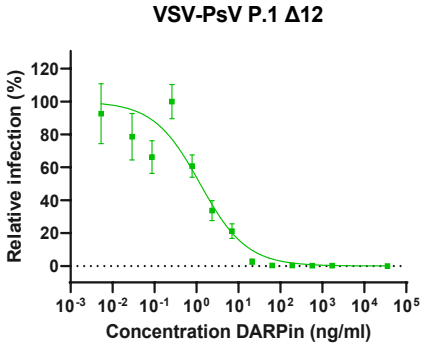

1016

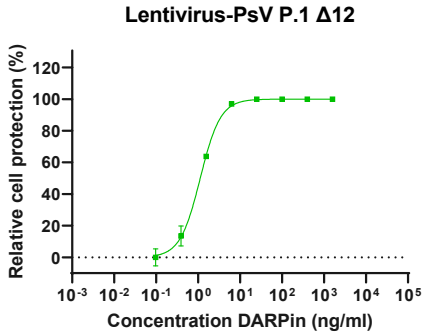

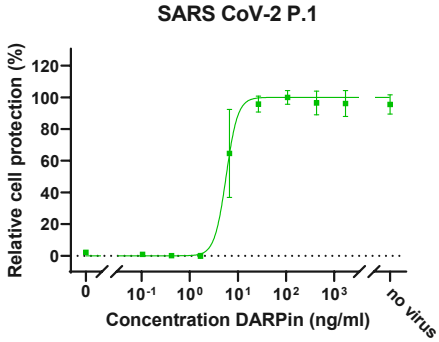

1017

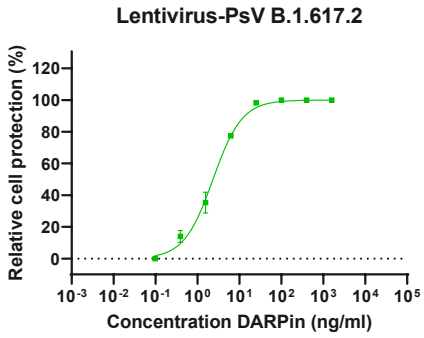

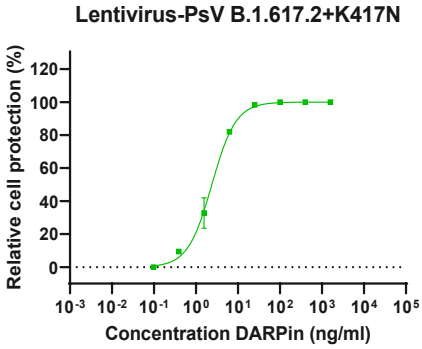

1018

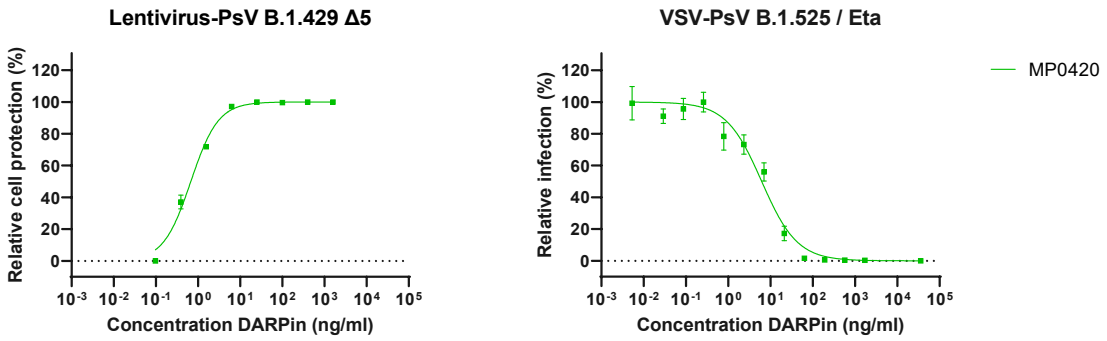

1019

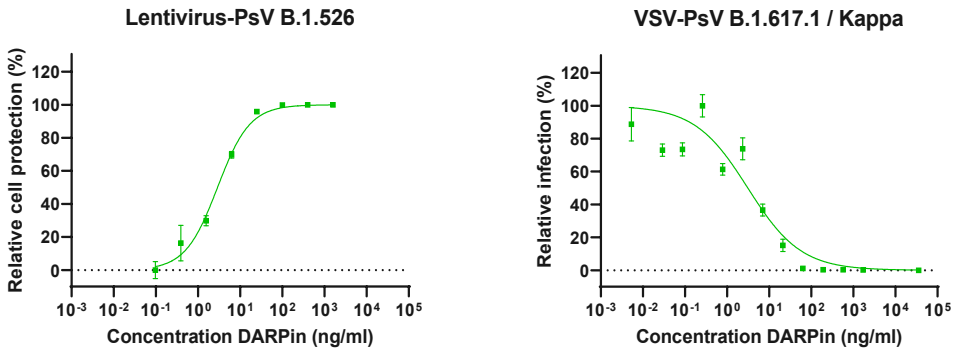

1020

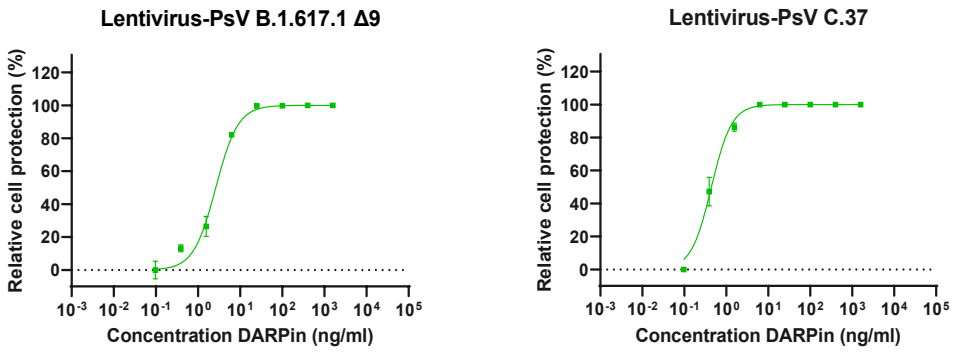

1021

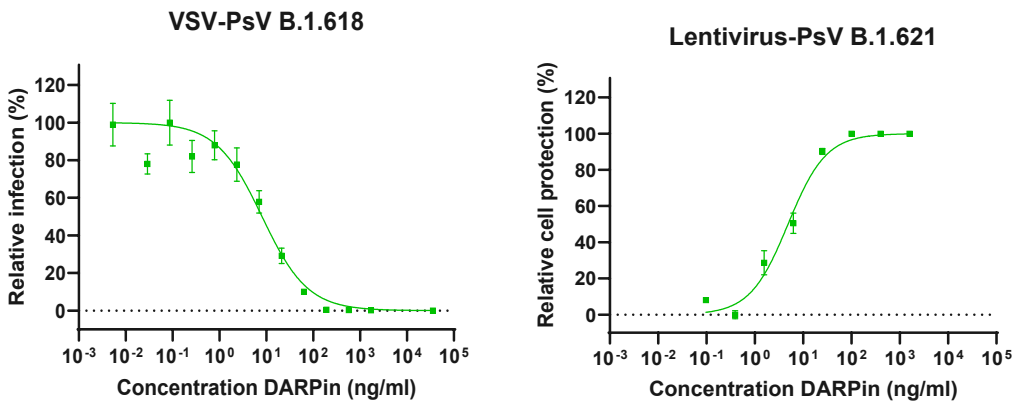

1022

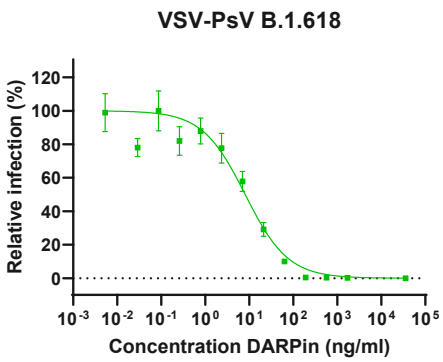

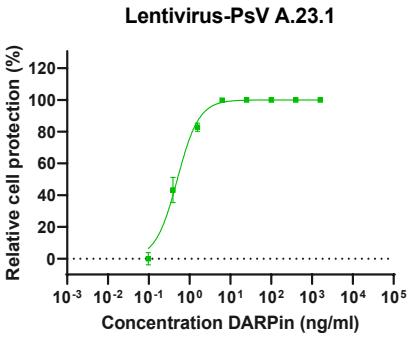

1023

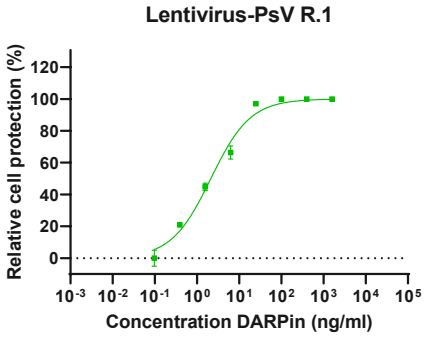

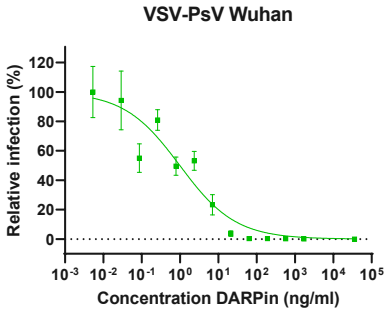

1024

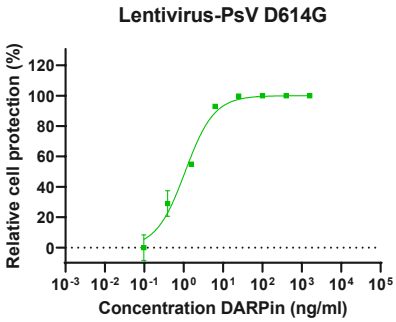

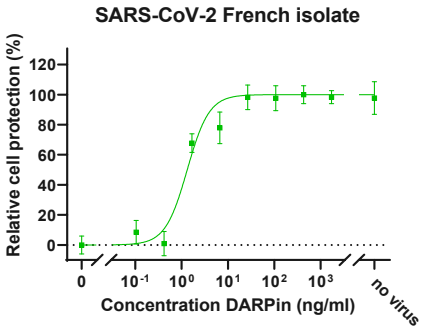

1025

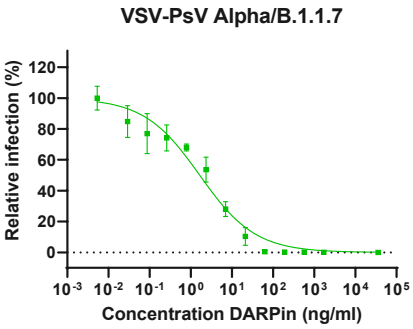

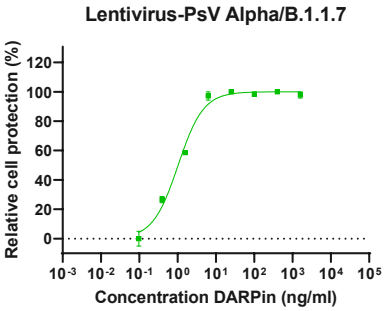

1026

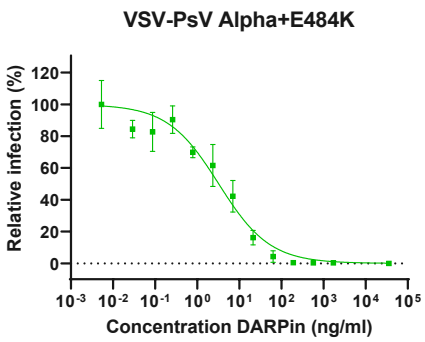

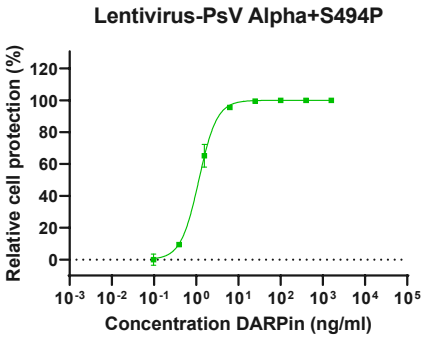

1027

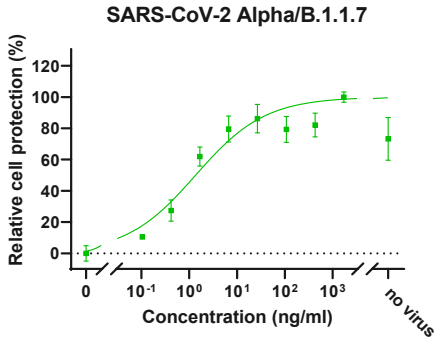

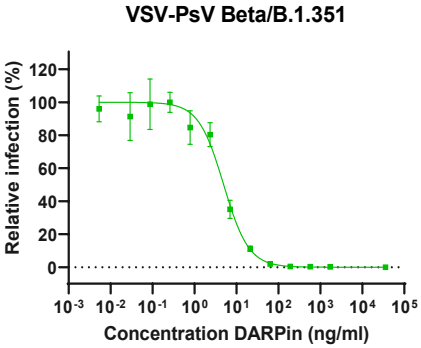

1028

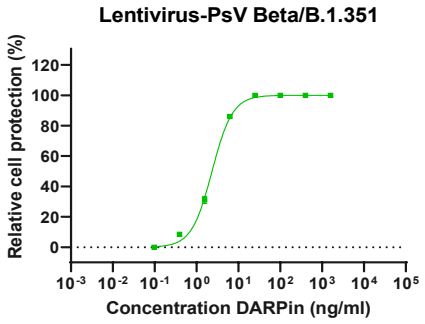

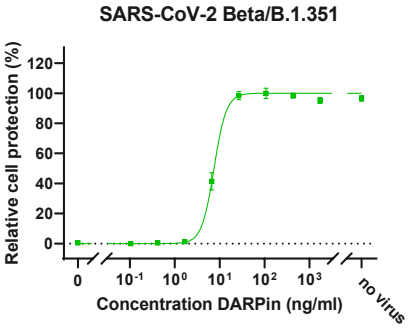

1029

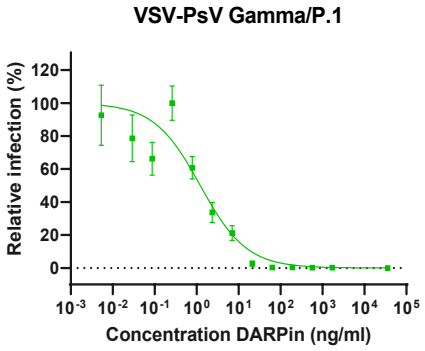

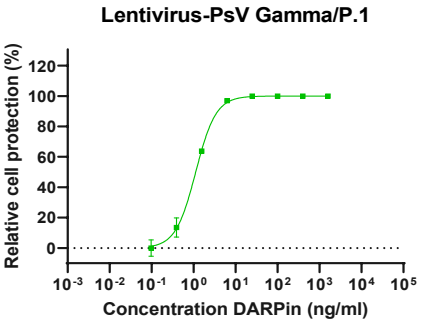

1030

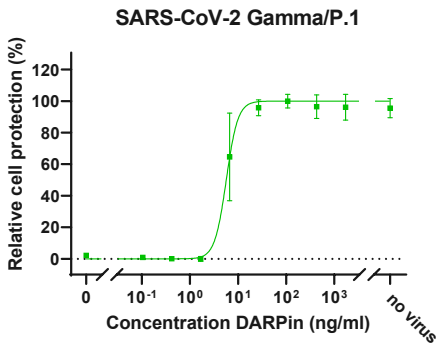

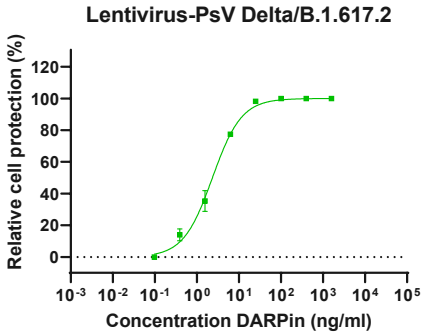

1031

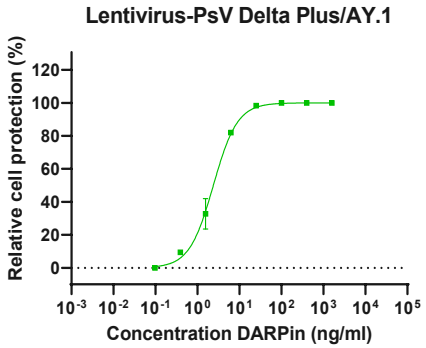

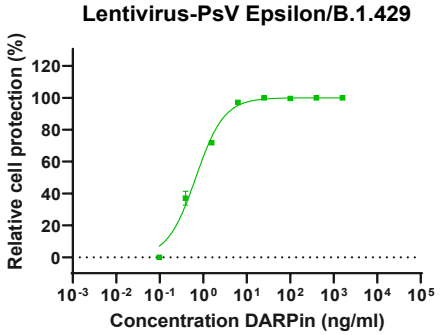

1032

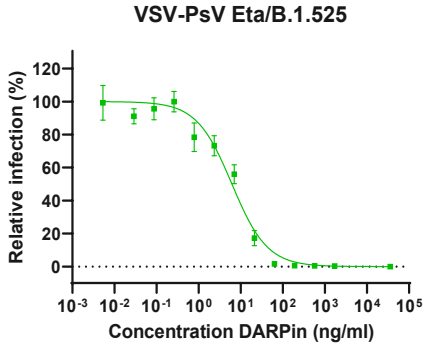

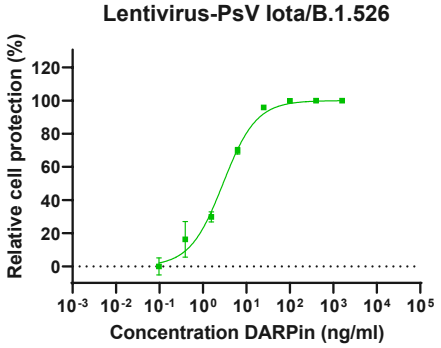

1033

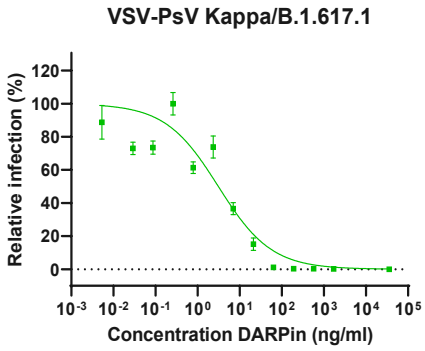

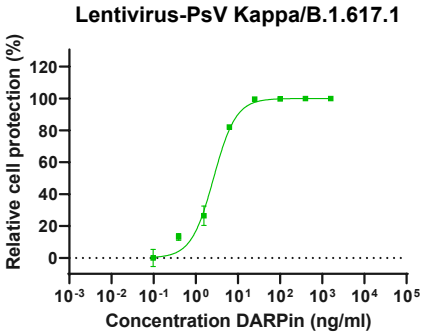

1034

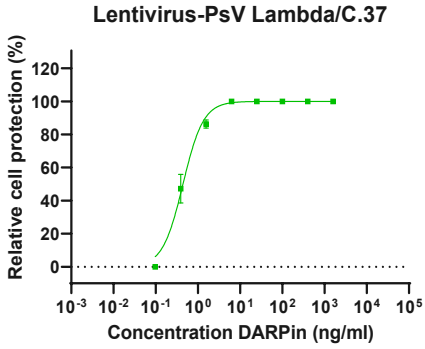

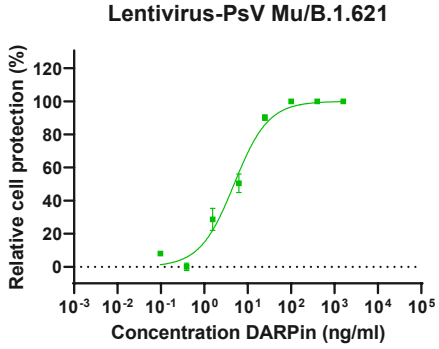

1035

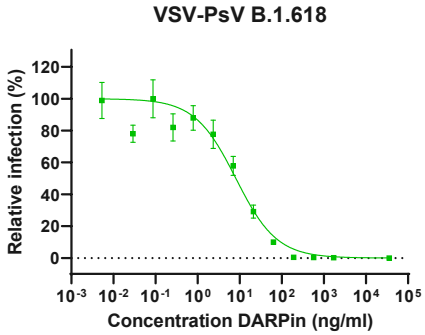

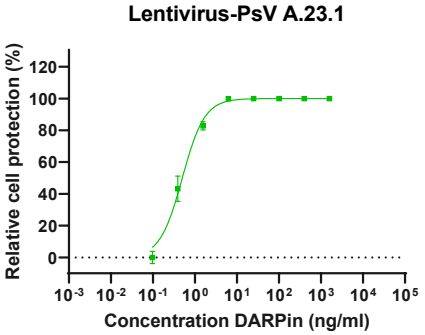

1036

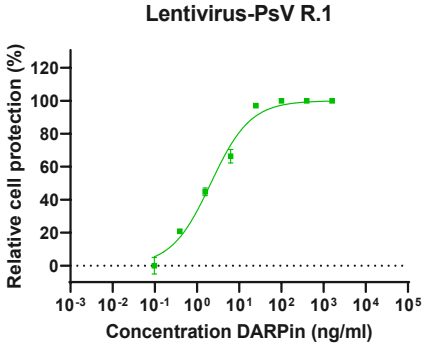

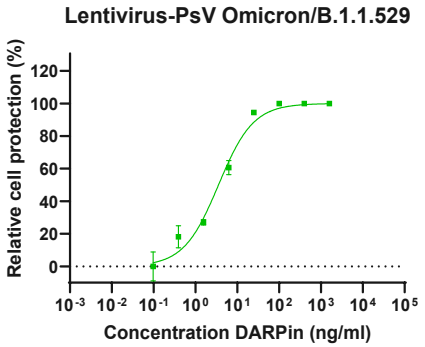

1037

1038

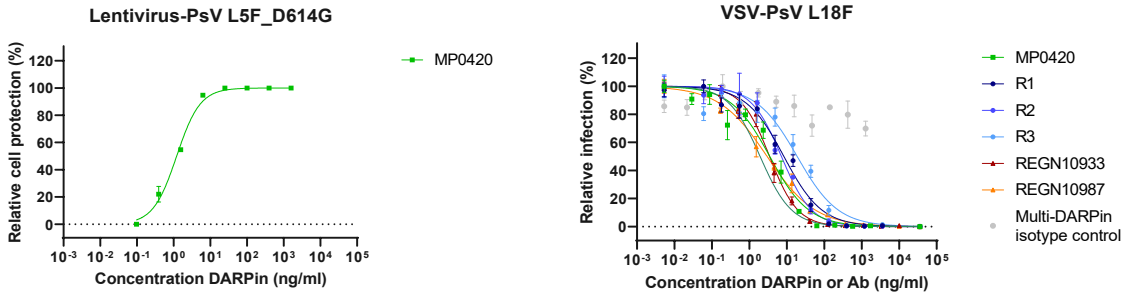

1039

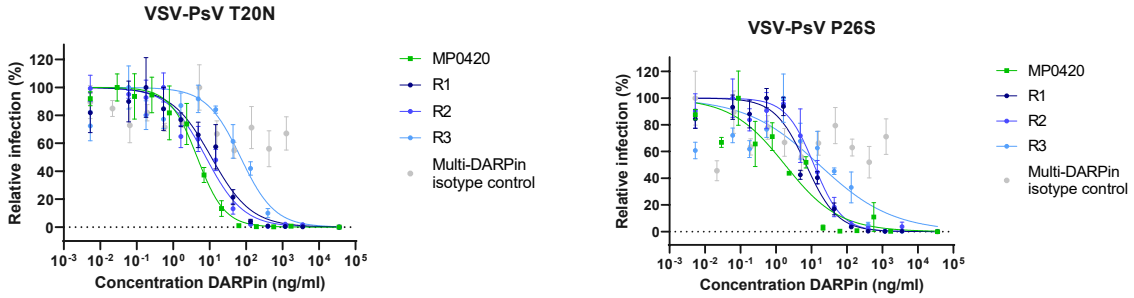

1040

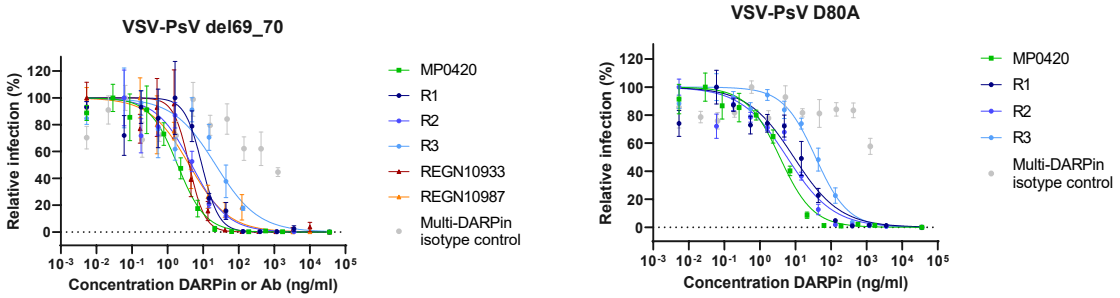

1041

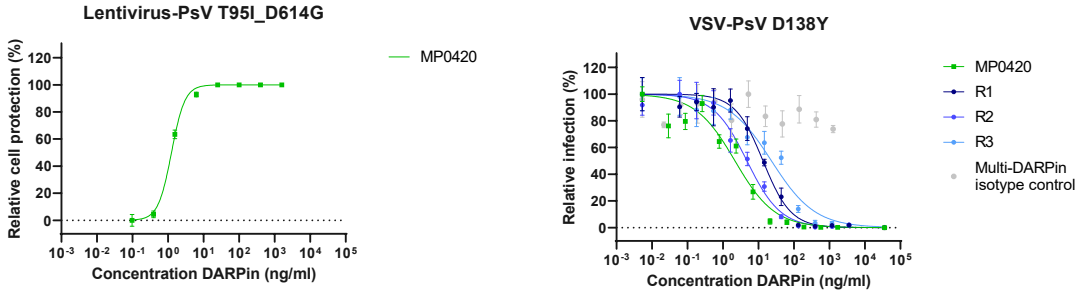

1042

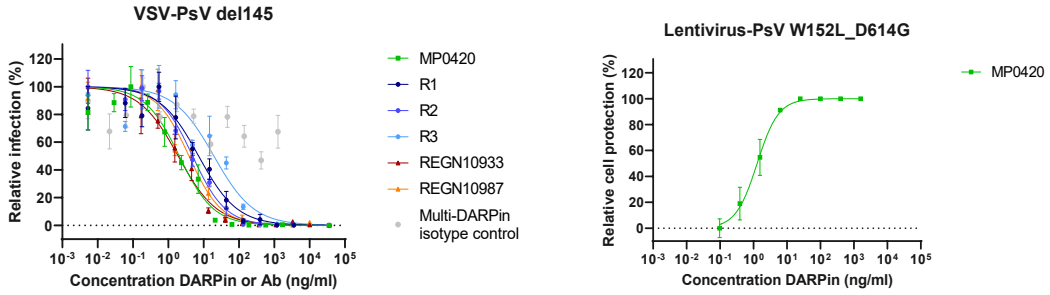

1043

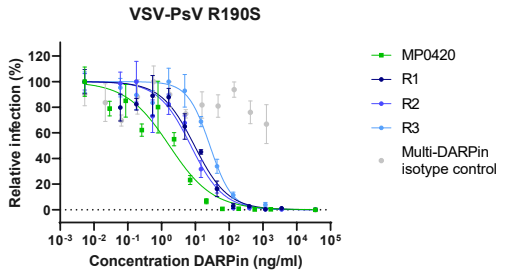

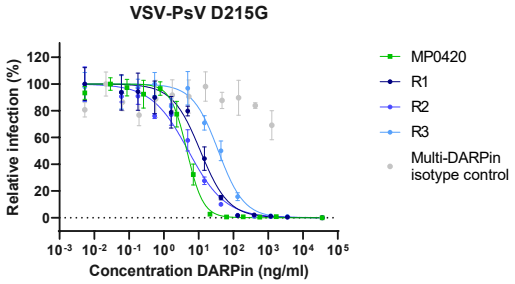

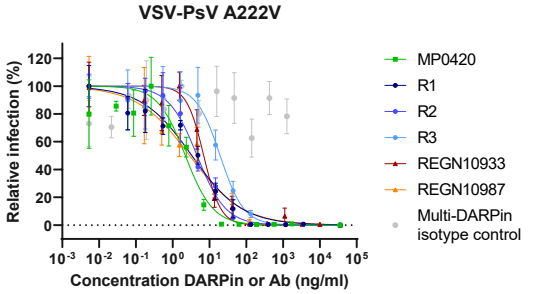

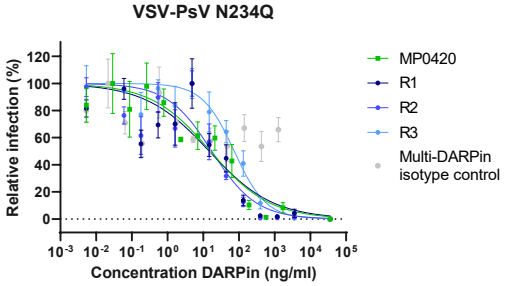

1045

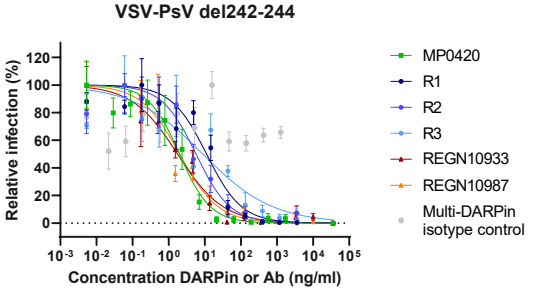

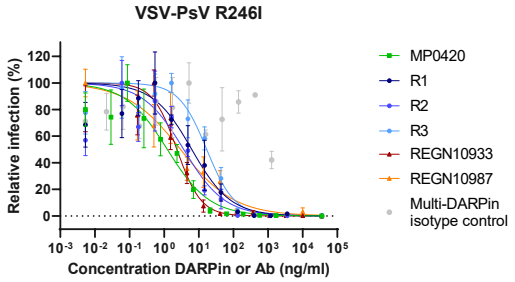

1046

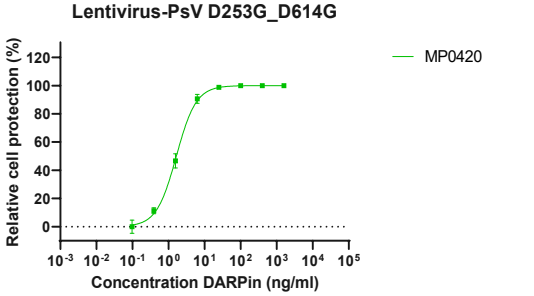

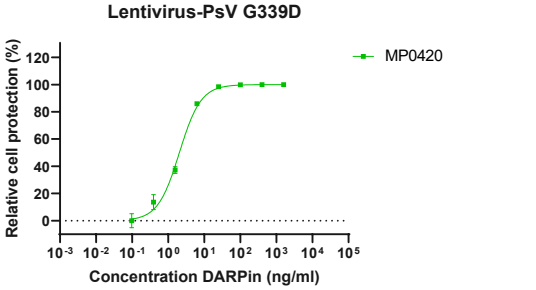

1047

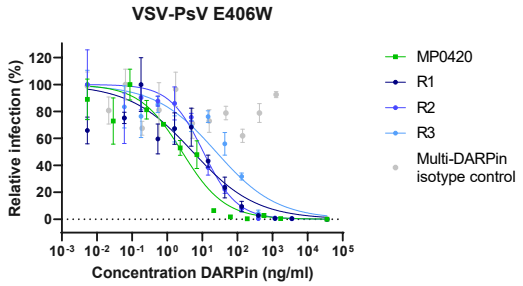

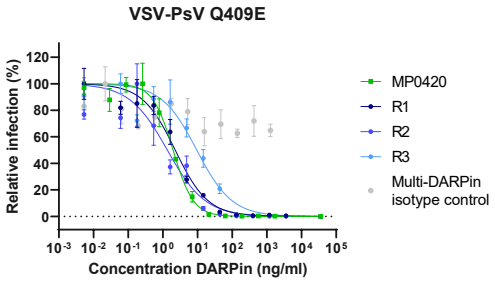

1048

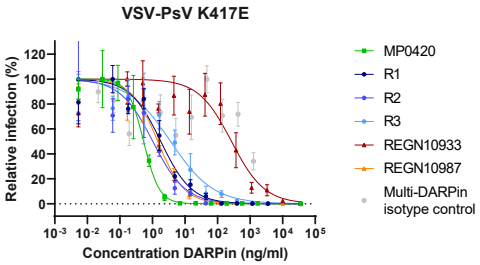

1049

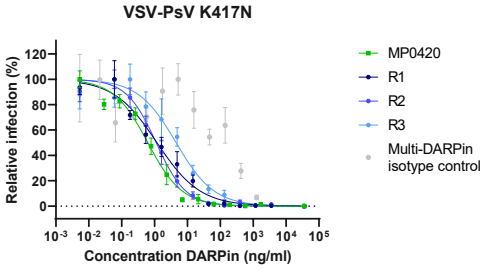

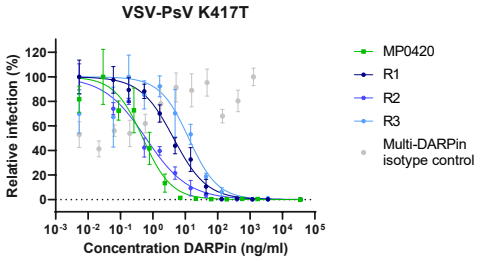

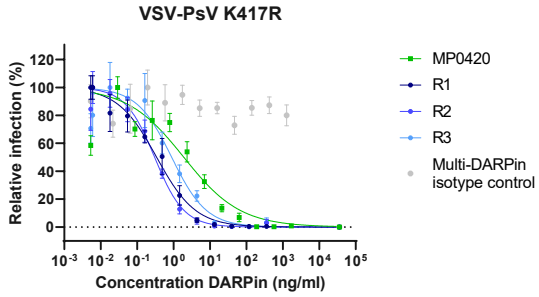

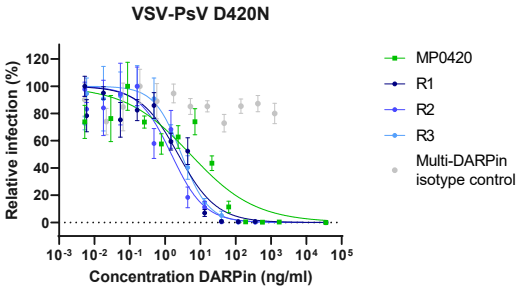

1051

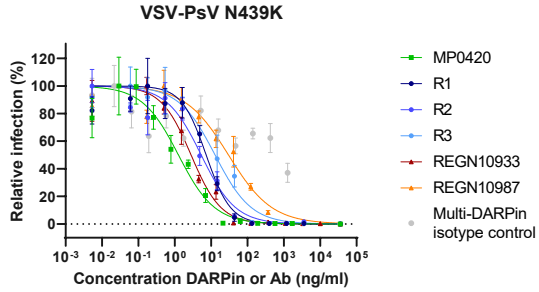

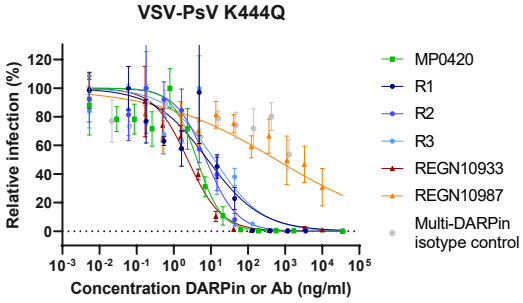

1052

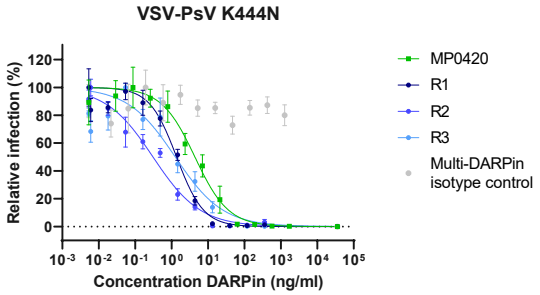

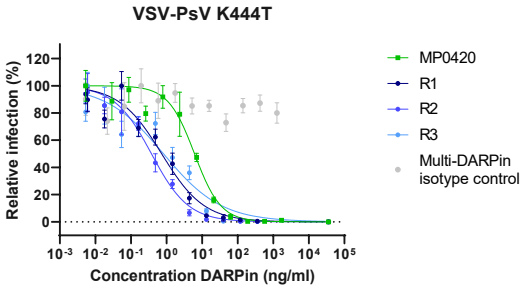

1053

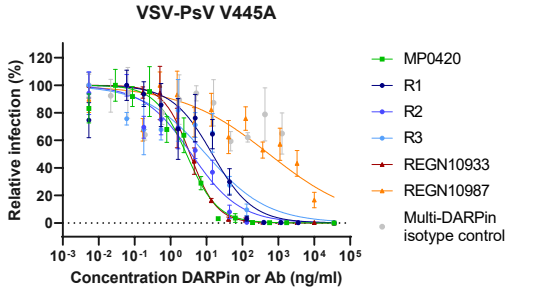

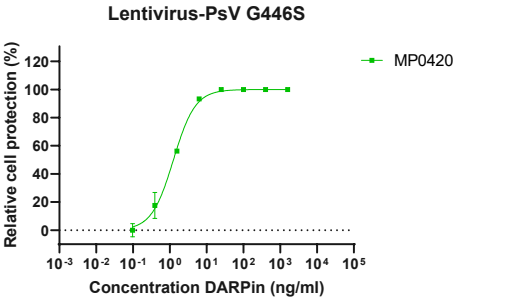

1054

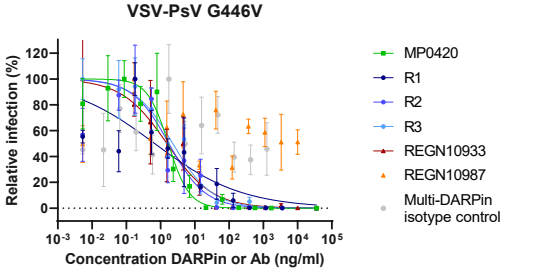

1055

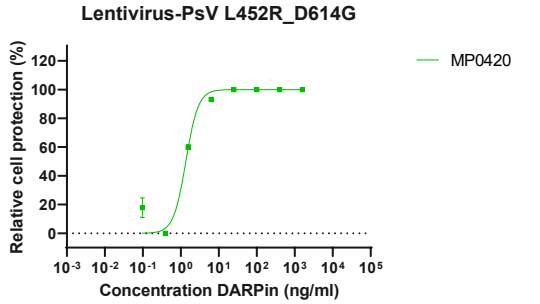

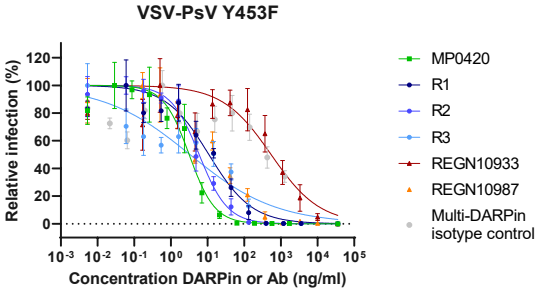

1056

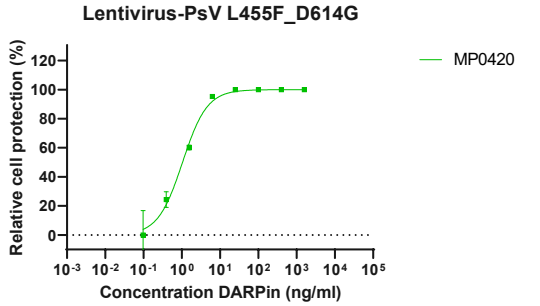

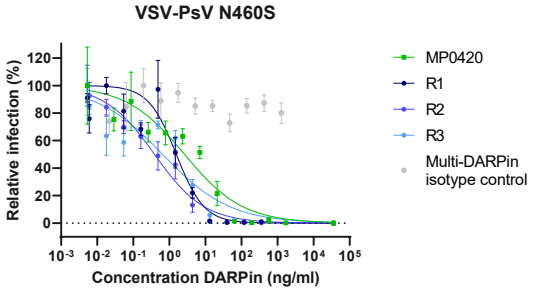

1057

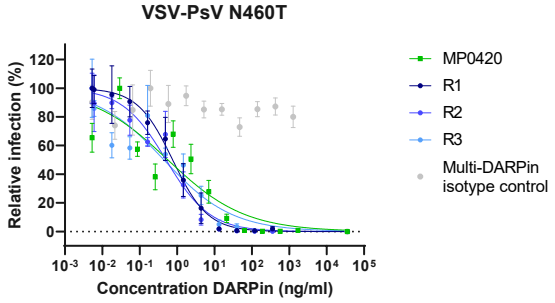

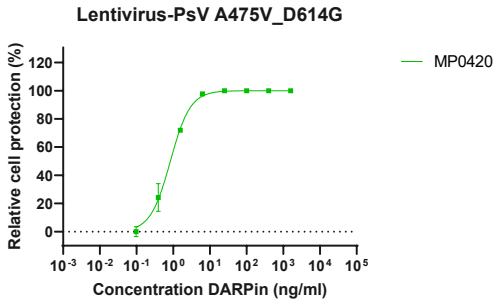

1058

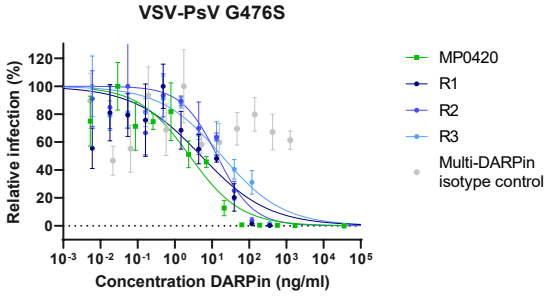

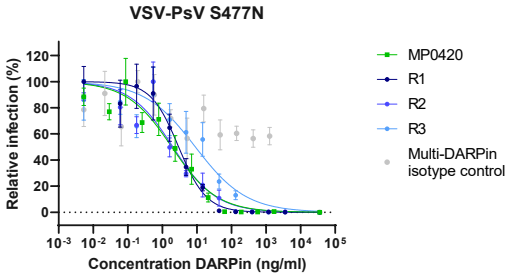

1059

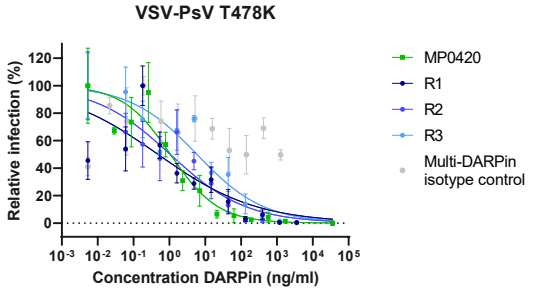

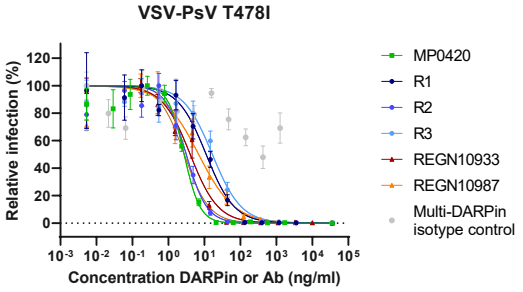

1060

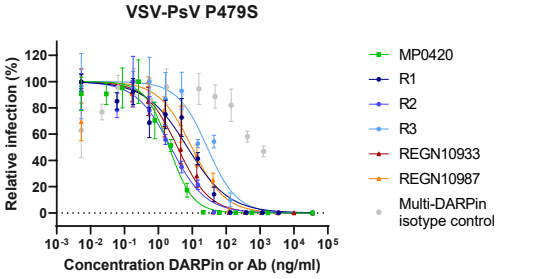

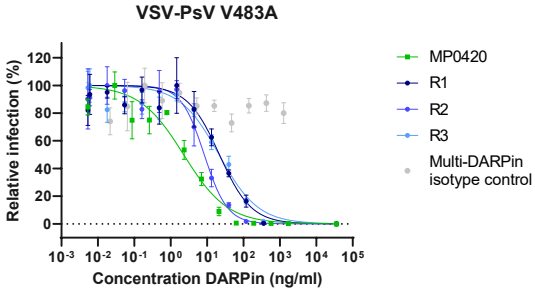

1061

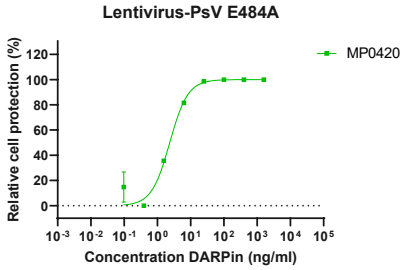

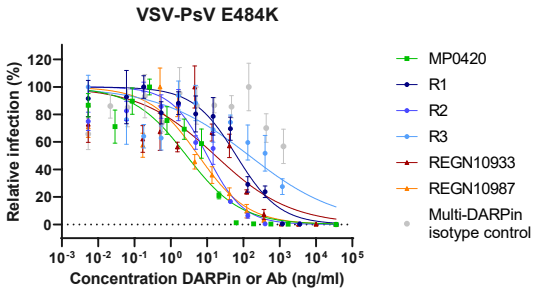

1062

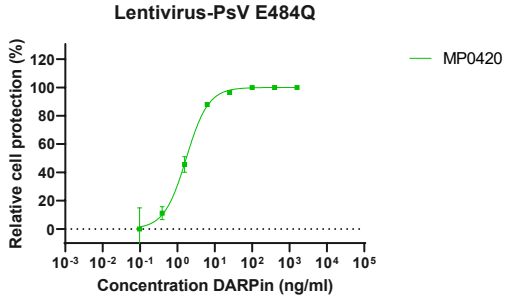

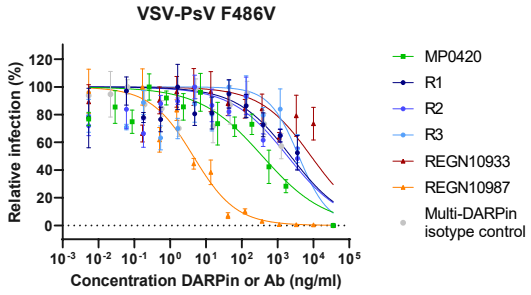

1063

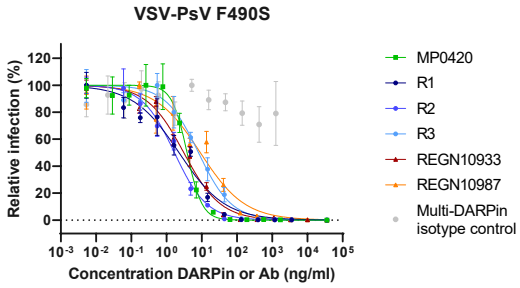

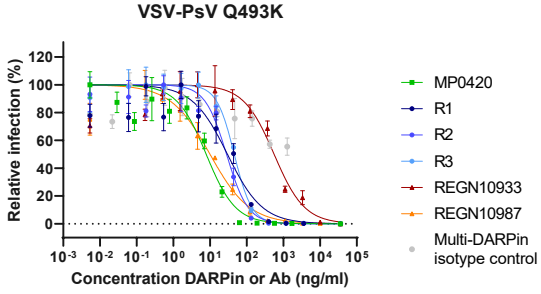

1064

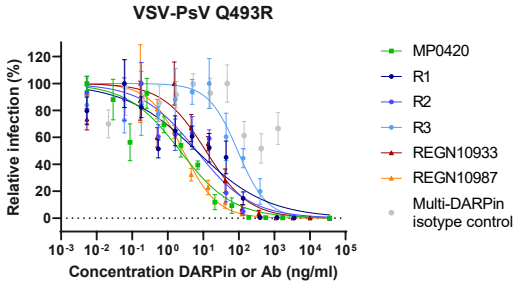

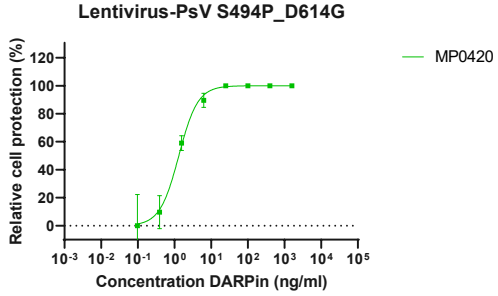

1065

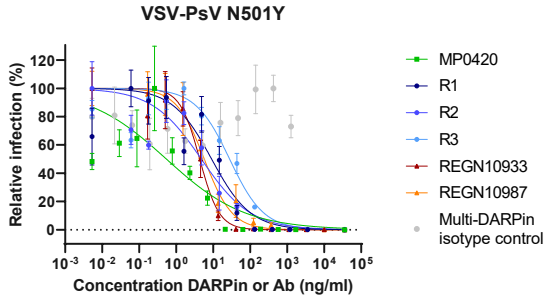

1066

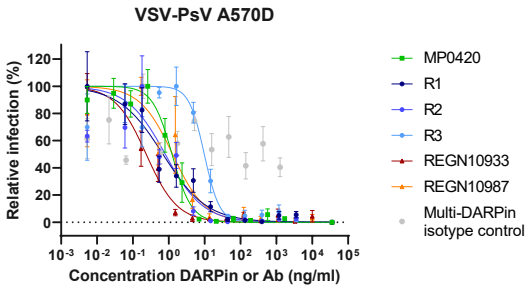

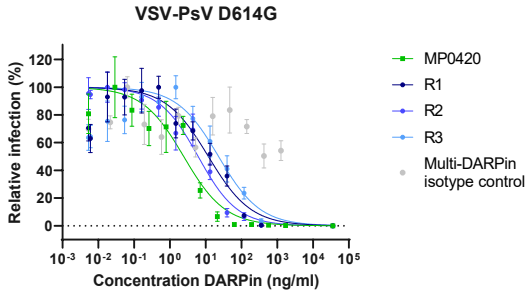

1067

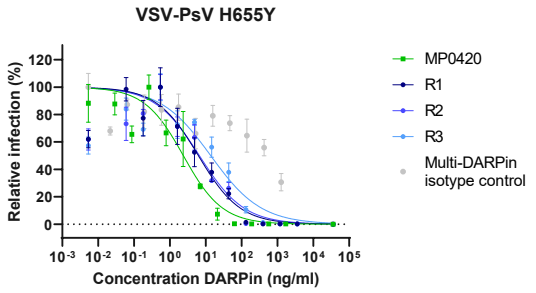

1068

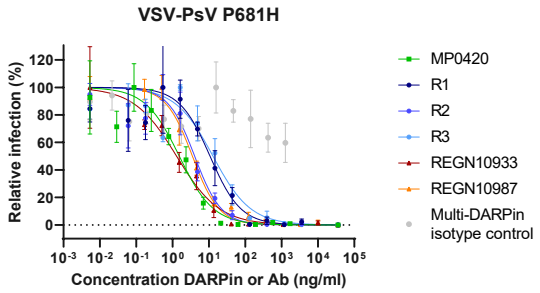

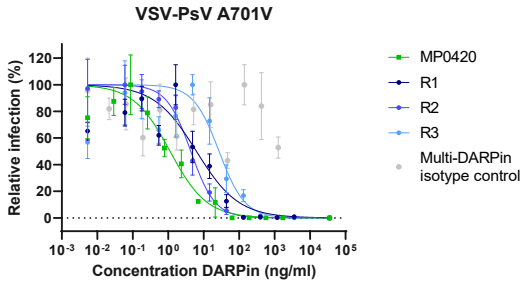

1069

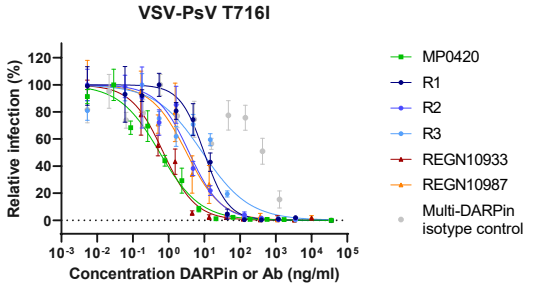

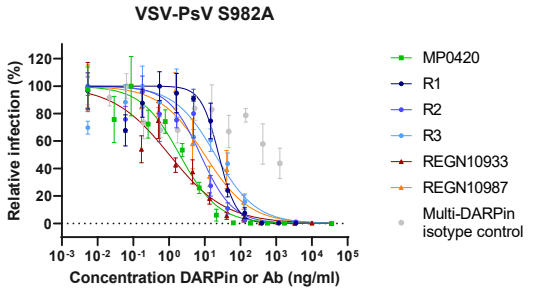

1070

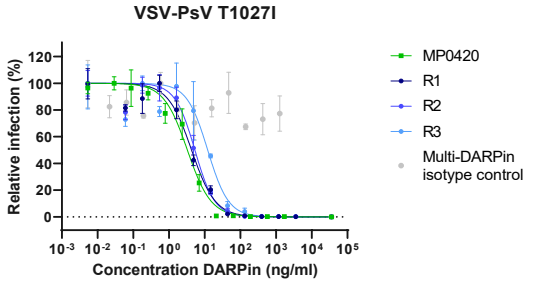

1071

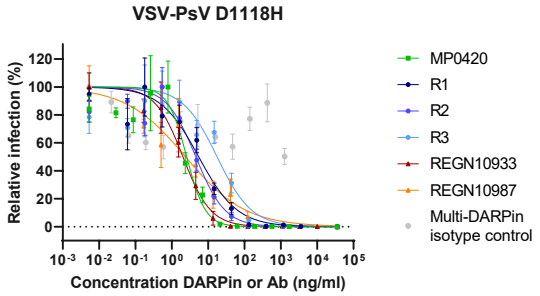

1072

1073 ***Supplementary Figure 4:*** *Titration curves for ensovibep (MP0420) and its RBD-binding*
1074 *domains (i.e. R1, R2 and R3), REGN10933 and REGN10987 to determine* IC_{50} *neutralization*
1075 *potencies on multiple spike mutants or only for ensovibep (MP0420) on the variants, which*
1076 *are summarized in Figure 2. Reported is the mean +/− SEM (standard error of the mean).*

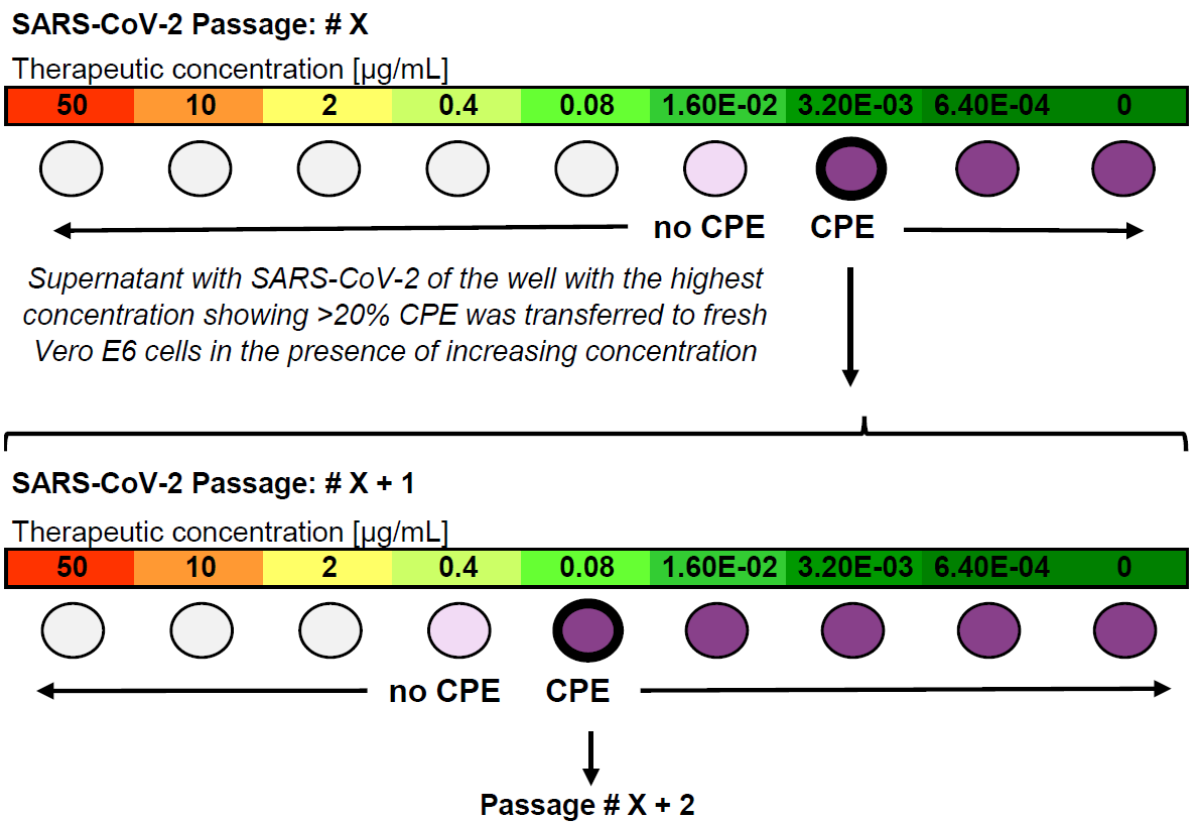

CPE: Cytopathic effect; no CPE: no or minor (<20%) cytopathic effect (by crystal violet staining)

***Supplementary Figure 5: Overview of the experimental protocol for viral passaging**: A patient SARS-CoV-2 isolate from early 2020 (1.5 ×10^6 pfu) was incubated in presence of increasing concentrations of DARPin candidate or antibody for 4 days on Vero E6 cells and virus-induced cytopathic effects (CPE) were determined by microscopy. For each DARPin and antibody condition, cultures showing significant cytopathic effect (≥20%) under the greatest selective pressure were selected and virus-containing supernatant collected to start a new culture passage on Vero E6 cells (bold circle), again under increasing concentrations of the corresponding DARPin candidate or antibody condition. Passaging of virus containing supernatant was continued in the same manner for a total of 4 passages.*

1088 **A** **B**

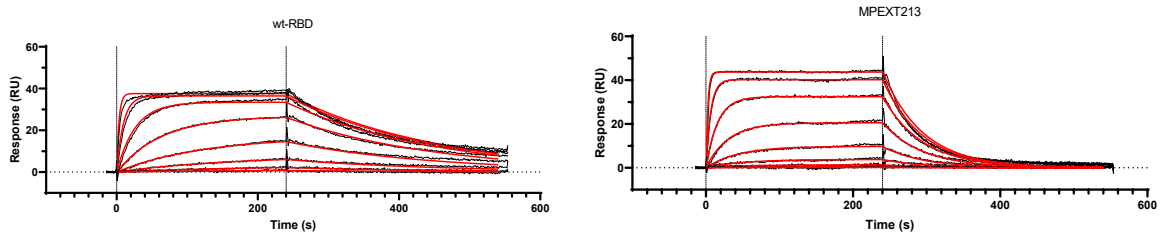

1089

1090 **C** **D**

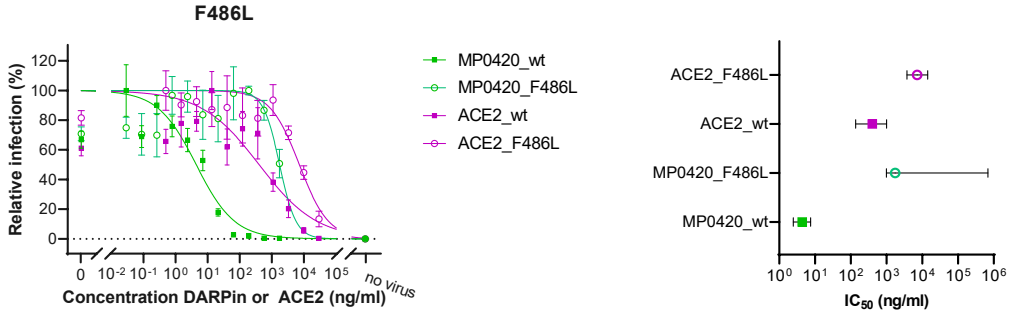

1091

1092 ***Supplementary Figure 6: Impact of mutation F486L in the RBD on ACE2 binding and***
1093 ***neutralization potency of ACE2 or ensovibep (MP0420) in a pseudotype assay***

1094 *A, B) Binding kinetics for different concentrations of ACE2 was determined by SPR (surface*
1095 *plasmon resonance) with A) immobilized wild type RBD and B) immobilized RBD with the*
1096 *substitution F486L (MPEXT213). Consequently, a drop in affinity was observed upon tested*
1097 *substitution from a KD of 7.8 nM (wild type) to a KD of 68.1 nM (F486L).*
1098 *C, D) Titration of ACE2 and ensovibep (MP0420) for neutralization of a VSV pseudotype with*
1099 *SARS-CoV-2 wild type spike protein compared to F486L substituted in the spike protein. D)*
1100 *IC_{50} values with 95% confidential interval for the titrations shown in C) demonstrating the loss*
1101 *of potency for ACE2 and ensovibep due to the F486L substitution. In accordance with the SPR*
1102 *measurement, a >10-fold drop in neutralization potency was observed in a VSV pseudotype*
1103 *assay, when ACE2 was used as a competitor. In relation, a >100-fold drop in potency was*
1104 *observed for ensovibep based on the F486L substitution.*
1105 *Shown experiments further underlines the reduction in binding of ACE2 to the F486L*
1106 *substitution and the importance of F486 for the SARS-CoV-2 virus to maintain the interaction*
1107 *with the human ACE2 receptor. So far, based on the global SARS-CoV-2 database sequences*
1108 *published in GISAID, mutations in position F486 (the core RBD-interaction residue for*
1109 *ensovibep) occur at very low frequencies.*

1110 **A**

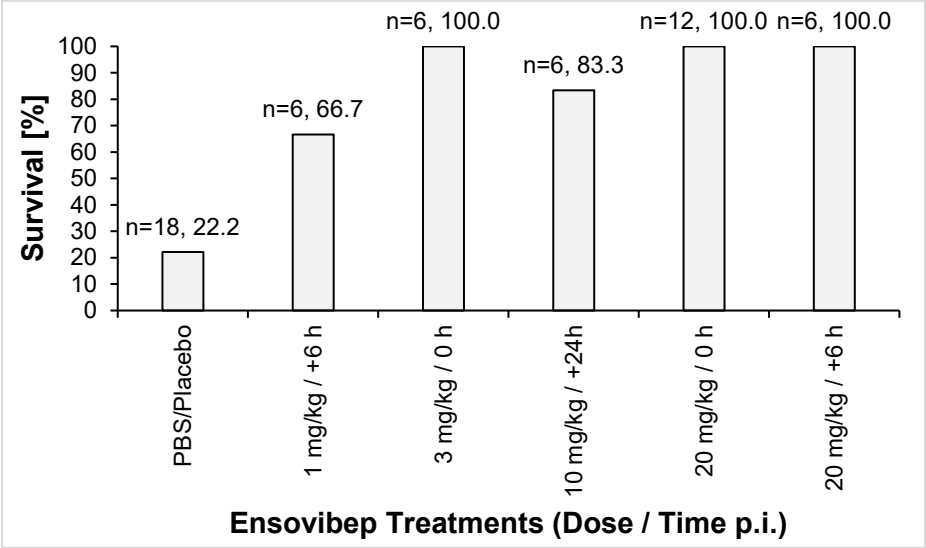

1111

1112 **B**

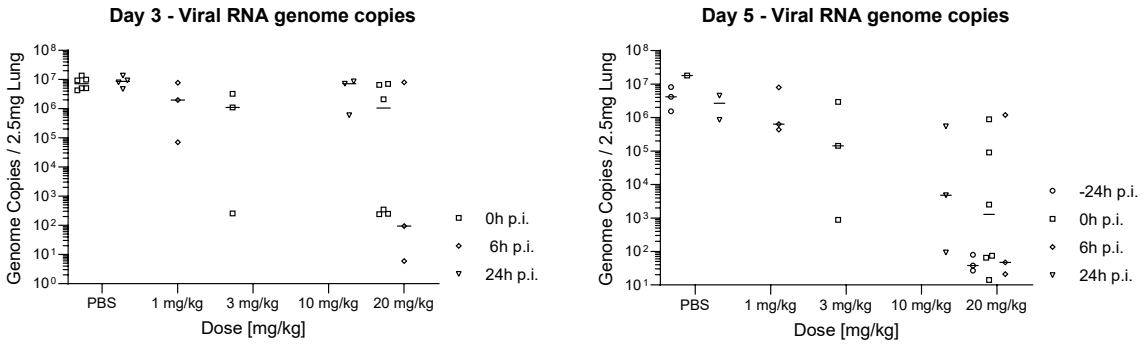

1114 **C**

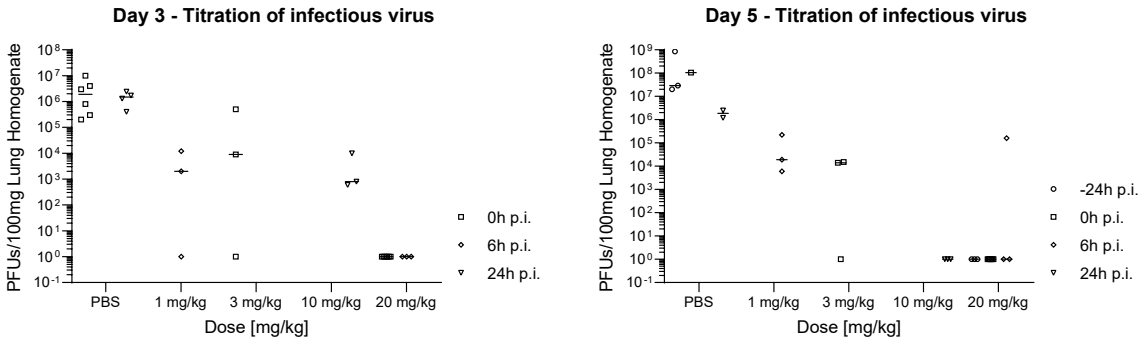

1116 ***Supplementary Figure 7:*** *Summarized previous in vivo studies with Roborovski dwarf*
1117 *hamster infected with WT SARS-CoV-2 and treated with ensovibep at various doses and*
1118 *administration time points. A) Animal survival, end-point analysis, animals that had to be*
1119 *euthanized according to score sheet criteria were considered non-survived, animals that*
1120 *reached their respective defined take-out at day 3 or 5 post infection were considered*

1121 *survived. B) qPCR analysis of virus gRNA copy numbers in oropharyngeal swabs and lung*
1122 *homogenates at day 3 or day 5 post infection C) Titration of replication competent virus from*
1123 *lung homogenates as plaque assay on Vero E6 cells at day 3 or day 5 post infection.*

1124 **A**

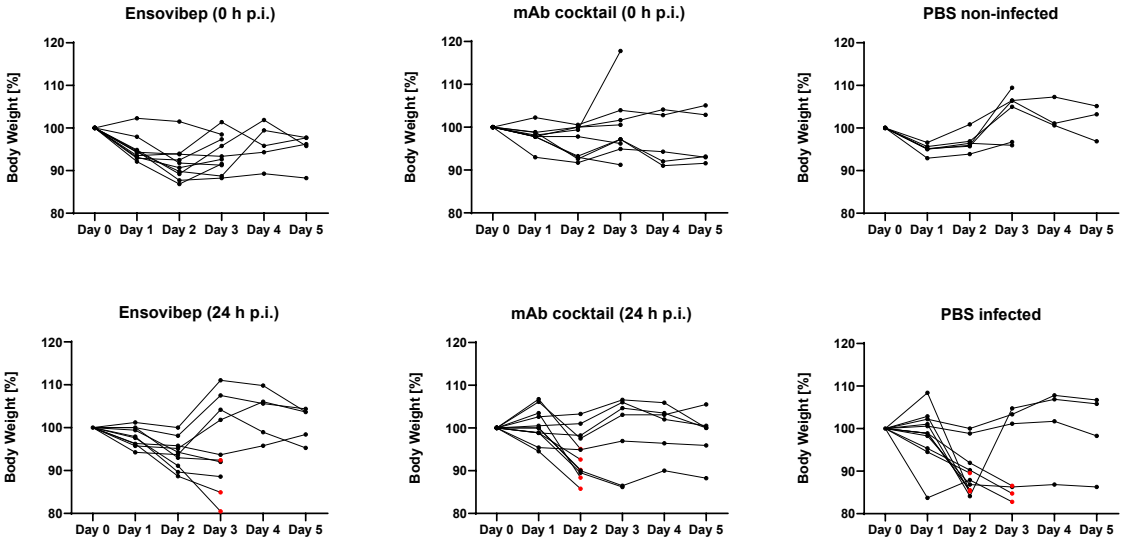

1125

1126 **B**

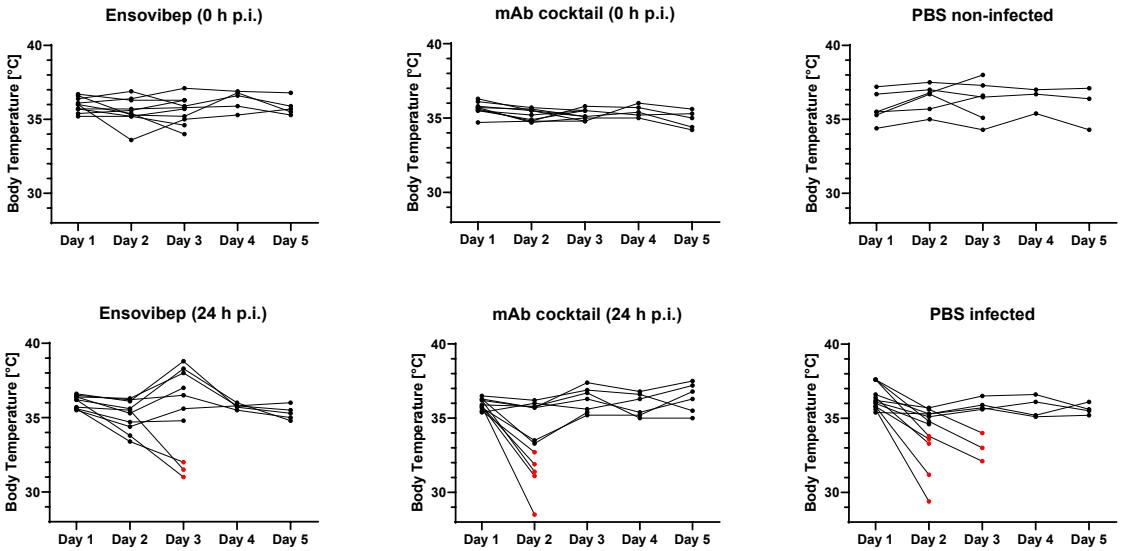

1127

1128 ***Supplementary Figure 8: Clinical Parameters of individuals over the course of***
1129 ***infection, (mean +/- SD presented in Figure 5C)*** *A) Body weight changes of individual*
1130 *hamsters B) Body temperatures of individual hamsters. Animals that had to be euthanized*
1131 *based on score sheet criteria are marked in red.*

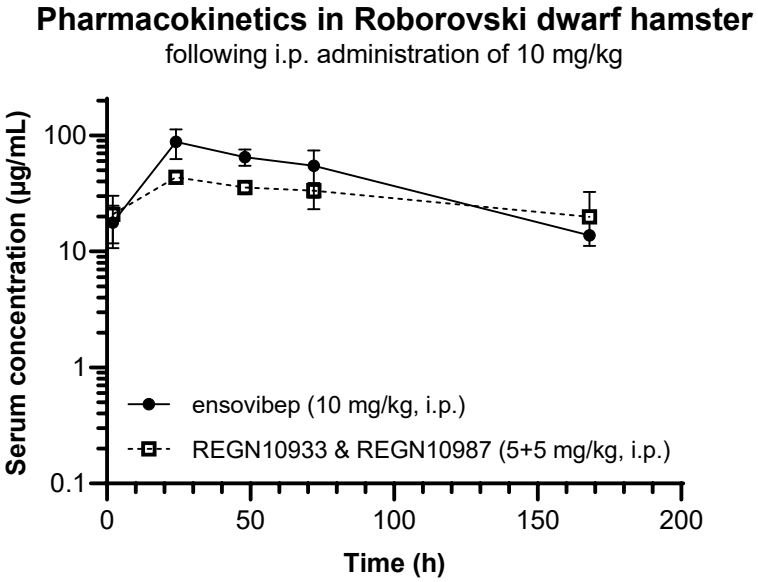

Supplementary Figure 9: *Pharmacokinetics profiles of non-infected Roborovski dwarf hamsters injected i.p. with either 10 mg/kg of ensovibep or the cocktail of REGN10933 and REGN10987 at 5 mg/kg for each of the monoclonal antibodies. Three animals were sacrificed for determination of the therapeutic concentration in the serum of the terminal bleeds. Obvious outliers due to likely a failure of the intraperitoneal injection were removed from the evaluation. Pharmacokinetic parameters for ensovibep:* $T_{1/2}$*: 52.0 h;* C_{max}*: 87.8 µg/mL;* T_{max}*: 24 h. Pharmacokinetic parameters for the cocktail of REGN10933 and REGN10987:* $T_{1/2}$*: 139 h;* C_{max}*: 43.5 µg/mL;* T_{max}*: 24h.*

1141 **Supplementary Table 1:** Cryo-EM data collection and image processing information.

Incubation time (seconds)	**60**	**60**	**15**
Magnification	75,000	75,000	92,000
Voltage [94]	300	300	200
Electron exposure (e-/Å^2)	40	40	40
Defocus range (μm)	1.25-2.5	1.25-2.5	1.25-2.5
Pixel size (Å)	1.045	1.045	1.1
Symmetry imposed	C3	C1	N/A
Initial particle images (no.)	123,833	123,833	46,140
Final particle images (no.)	46,762	21,612	6,888
Map resolution (Å)	4.2	9.6	N/A
FSC threshold	0.143	0.143	N/A
Map resolution range (Å)	3.6-14.1	8.2-26	N/A

1142

1143 ***Supplementary Table 2:*** *In vitro protection against emerging SARS-CoV-2 variants for*
1144 *ensovibep*

Variant	Substitutions / Deletions	Assay Type	Neutralizing IC_{50} [ng/mL]
References	Wuhan wild type	VSV pseudotype	1
	D614G background	Lentivirus pseudotype	1.1
	French isolate: V367F; E990A	Authentic virus	1.3
Alpha / B.1.1.7	69-70 del, del145, N501Y, A570D, D614G, P681H, T716I, S982A, D1118H	VSV	1.7
	69-70 del, del145, E484K, N501Y, A570D, D614G, P681H, T716I, S982A, D1118H	VSV	3.2
	69-70 del, del145, N501Y, A570D, D614G, P681H, T716I, S982A, D1118H	Lentivirus pseudotype	0.9
	69-70 del, del145, S494P, N501Y, A570D, D614G, P681H, T716I, S982A, D1118H	Lentivirus pseudotype	0.8
	H69_V70del, Y145del, N501Y, A570D, D614G, P681H, T716I, S982A, D1118H	Authentic	1.3
Beta / B.1.351	D80A, D215G, E484K, N501Y, A701V	VSV	5.5
	L18F, D80A, D215G, Del242-244, R246I, K417N, E484K, N501Y, D614G, A701V	VSV	5
	L18F, D80A, D215G, Del242-244, K417N, E484K, N501Y, D614G, A701V	Lentivirus pseudotype	1.2
	L18F, D80A, D215G, L242_L244del, T302T, K417N, E484K, N501Y, D571D,D614G, A701V	Authentic	7.5
Gamma / P.1	L18F, T20N, P26S, D138Y, R190S, K417T, E484K, N501Y, D614G, H655Y, T1027I	VSV	1.2
	L18F, T20N, P26S, D138Y, R190S, K417T, E484K, N501Y, D614G, H655Y, T1027I, V1176F	Lentivirus pseudotype	0.7
	L18F, T20N, P26S, D138Y, R190S, K417T, E484K, N501Y, D614G, H655Y, T1027I, V1176F	Authentic	5.7
Delta/DeltaPlus / B.1.617.2	T19R, G142D, E156GI, F157del, R158del, L452R, T478K, D614G, P681R, D950N	Lentivirus pseudotype	2.4
	T19R, T95I, G142D, E156G, F157del, R158del, W258L, K417N, L452R, T478K, D614G, P681R, D950N	Lentivirus pseudotype	2.6
Epsilon/B.1.429	S13I, W152C, L452R, D614G	Lentivirus pseudotype	0.9
	S13I, P26S, W152C, L452R, D614G	Lentivirus pseudotype	0.5
Iota/B.1.526	L5F, T95I, D253G, E484K, D614G, A701V	Lentivirus pseudotype	3.0
Kappa / B.1.617.1	T95I, G142D, E154K, L452R, E484Q, D614G, P681R, Q1071H	Lentivirus pseudotype	2.0
	G142D, E154K, V382L, L452R, E484Q, D614G, P681R, Q1071H, D1153Y	Lentivirus pseudotype	1.9
Lambda / C37	G75V, T76I, R246del, S247-G252del, D253N, L452Q, F490S, D614G, T859N	Lentivirus pseudotype	0.4

Mu / B.1.621	T95I, Y144S, Y145N, R346K, E484K, N501Y, D614G, P681H, D950N	Lentivirus pseudotype	6.1
Omicron / B.1.1.529	A67V, Δ69-70, T95I, G142D, Δ143-145, Δ211, L212I, ins214EPE, G339D, S371L, S373P, S375F, K417N, N440K, G446S, S477N, T478K, E484A, Q493R, G496S, Q498R, N501Y, Y505H, T547K, D614G, H655Y, N679K, P681H, N764K, D796Y, N856K, N969K, L981F	VSV pseudotype	2.2
	A67V, Δ69-70, T95I, G142D, Δ143-145, Δ211, L212I, ins214EPE, G339D, S371L, S373P, S375F, K417N, N440K, G446S, S477N, T478K, E484A, Q493K, G496S, Q498R, N501Y, Y505H, T547K, D614G, H655Y, N679K, P681H, N764K, D796Y, N856K, Q954H, N969K, L981F	VSV pseudotype	2.1
	A67V, Δ69-70, T95I, G142D, Δ143-145, Δ211, L212I, ins214EPE, G339D, S371L, S373P, S375F, K417N, N440K, G446S, S477N, T478K, E484A, Q493R, G496S, Q498R, N501Y, Y505H, T547K, D614G, H655Y, N679K, P681H, N764K, D796Y, N856K, Q954H, N969K, L981F	Lentivirus pseudotype	3.6
R.1	W152L, E484K, D624G, G769V	Lentivirus pseudotype	2.4
A.23.1	F157L, V367F, Q613H, D614G, P681R	Lentivirus pseudotype	0.3

1145

1146 ***Supplementary Table 3:*** In vitro *protection against SARS-CoV-2 spike protein substitutions*
1147 *or deletions for ensovibep.*

Amino acid position	Substitution / deletion	Assay Type	Neutralizing IC_{50} [ng/mL]
L18	F	VSV	3.5
T20	N	VSV	4.6
P26	S	VSV	1.8
69-70	del	VSV	1.9
D80	A	VSV	3.6
T95	I	Lenti	0.9
D138	Y	VSV	2.2
145	del	VSV	2.1
W152	L	Lenti	1.2
R190	S	VSV	1.7
A222	V	VSV	2.2
N234	Q	VSV	16.2
242-244	del	VSV	2.0
G339	D	Lenti	2.0
E406	Q	Lenti	1.5
	W	VSV	2.7
Q409	E	VSV	2.0
K417	E	VSV	0.5
	N	VSV	0.6
	R	VSV	2.1
	T	VSV	0.5
D420	N	VSV	5.6
N439	K	VSV	1.3
K444	E	Lenti	0.8
	N	VSV	4.4
	Q	Lenti	1.3
	T	VSV	6.1
V445	A	Lenti	1.3
G446	V	VSV	1.7
	S	Lenti	1.3
N450	D	Lenti	0.9
L452	R	Lenti	0.4
Y453	F	VSV	3.2

L455	F	Lenti	1.1
N460	S	VSV	2.6
	T	VSV	0.6
A475	V	Lenti	0.9
G476	S	VSV	1.5
S477	N	VSV	1.9
T478	I	VSV	2.7
	K	Lenti	1.5
P479	S	VSV	2.1
V483	A	VSV	2.3
E484	A	Lenti	2.4
	K	VSV	2.7
	Q	Lenti	2.3
G485	D	VSV	28.5
F486	V	VSV	>100
	L	VSV	>100
F490	S	VSV	3.8
Q493	K	VSV	7.9
	R	VSV	2.2
S494	P	Lenti	1.3
N501	Y	VSV	0.6
A570	D	VSV	1.2
D614	G	VSV	2.4
H655	Y	VSV	2.4
P681	H	VSV	1.5
A701	V	VSV	1.1
T716	I	VSV	0.6
S982	A	VSV	2.0
T1027	I	VSV	3.3
D1118	H	VSV	2.6

Supplementary Table 4: drug exposure levels in serum at day of euthanization. *Animals with drug exposure levels below 10% of the group average were removed from the study analysis (depicted in bold).*

Ensovibep (10 mg/kg i.p.; 0 h p.i)		
#	Animal ID	Serum concentration [µg/mL]
1	DN5_1	86.9
2	**DN5_2**	**2.7**
3	DN5_3	169.7
4	DN5_4	44.5
5	DN5_5	92.9
6	DN5_6	39.2
7	**DN5_7**	**1.5**
8	DN5_8	109.4
9	DN5_9	51.8
10	DN5_10	127.9
11	DN5_11	70.2
12	DN5_12	38.6

Ensovibep (10 mg/kg i.p.; 24 h p.i)		
#	Animal ID	Serum concentration [µg/mL]
1	DN5_25	17.0
2	**DN5_26**	**1.8**
3	DN5_27	39.1
4	DN5_28	N/A
5	DN5_29	48.0
6	**DN5_30**	**5.7**
7	DN5_31	225.1
8	DN5_32	27.3
9	DN5_33	66.6
10	DN5_34	109.5
11	DN5_35	128.4
12	DN5_36	78.3

REGN10933 & REGN10987 (5 + 5 mg/kg i.p.; 0 h p.i)		
#	Animal ID	Serum concentration [µg/mL]
1	DN5_13	29.0
2	**DN5_14**	**0.3**
3	DN5_15	26.5
4	**DN5_16**	**1.1**
5	DN5_17	34.0
6	**DN5_18**	**1.4**
7	DN5_19	41.9
8	DN5_20	30.3
9	DN5_21	43.5
10	DN5_22	38.0
11	DN5_23	28.1
12	DN5_24	32.7

REGN10933 & REGN10987 (5 + 5 mg/kg i.p.; 24 h p.i)		
#	Animal ID	Serum concentration [µg/mL]
1	DN5_37	72.0
2	DN5_38	60.9
3	DN5_39	42.8
4	DN5_40	32.6
5	DN5_41	46.7
6	DN5_42	41.9
7	DN5_43	43.7
8	DN5_44	45.3
9	DN5_45	46.1
10	DN5_46	61.9
11	DN5_47	37.2
12	DN5_48	41.8

N/A: Not available due to low amount of serum extracted from terminal bleeds

Bold: animals removed from the study data due to low therapeutic exposure

Red: animals taken out at 2 dpi

Blue: animals taken out at 3 dpi

Green: animals taken out at 5dpi

1149

1150

***Supplementary Table 5**: Identification of escape mutations by deep sequencing of SARS-CoV-2 Alpha variant B.1.1.7 in animals at day 5 p.i., which indicated remaining viral titers. As a control, three non-treated animals were also deep sequenced. Deep Sequencing was performed from either swab (S) or lung (L) extracted RNA.*

Treatment group	Animal identifier	Throat swab (S) or lung homogenate (L)	Identified spike protein amino acid substitution	Potential Impact
Ensovibep 0 dpi	DN5_2	L	-	-
		S	-	-
	DN5_4	L	-	-
		S	K1034M	Neutral / outside ensovibep epitope
antibody cocktail 0 dpi	DN5_15	L	-	-
		S	-	-
	DN5_24	L	-	-
		S	-	-
Ensovibep 1 dpi	DN5_30	L	-	-
		S	-	-
Placebo group	DN5_50	L	-	-
		S	R671L	At furin cleavage site
	DN5_52	L	-	-
		S	R671L	At furin cleavage site
	DN5_53	L	-	-
		S	-	-

1151

1152

***Supplementary Table 6** : Histopathology data table*

Stimulus	Necropsy day post infection	Inflammation Parameters					Bronchi			Alveoli			Vasculature		
		% affected	Degree of inflammation	Lymphocytes	Macrophages	Neutrophils	Broncho-epithelial necroses	Bronchitis	Broncho-epithelial hyperplasia	Alveolar epithelium necroses	Alveolar edema	Typ II Hyperplasia	Perivascular lymphocyte cuffs	Perivascular edema	Endotheliitis
PBS / non-infected - bleeding from lung preparation	3	20	1	0	1	1	0	1	0	0	1	0	0	1	0
PBS / non-infected - bleeding from lung preparation	3	<5	0	0	0	0	0	0	0	0	0	0	0	0	0
PBS / non-infected - bleeding from lung preparation	5	<5	0	0	0	0	0	0	0	0	0	0	0	0	0
PBS / non-infected - bleeding from lung preparation	5	<5	0	0	0	0	0	0	0	0	0	0	0	0	0
PBS / non-infected - bleeding from lung preparation	5	10	1	1	1	1	0	0	1	0	0	1	0	1	0
PBS / non-infected - bleeding from lung preparation	3	90	2	2	2	2	0	1	0	1	2	0	3	2	0
PBS / Infected	2	80	1	0	1	1	1	1	1	1	2	0	0	3	0
PBS / Infected	2	80	3	1	3	3	1	2	1	1	3	0	0	2	0
PBS / Infected	2	80	3	1	2	3	1	2	1	1	2	0	0	2	0
PBS / Infected	2	70	1	1	1	1	1	1	0	1	2	0	0	2	0
PBS / Infected	3	70	3	1	3	3	1	3	1	0	2	1	0	2	0
PBS / Infected	3	70	2	2	2	2	1	2	0	0	3	1	2	2	0
PBS / Infected	3	20	1	1	1	1	1	2	0	1	2	0	0	1	0
PBS / Infected	5	40	3	2	2	2	0	2	1	0	0	2	0	1	0
PBS / Infected	5	60	3	2	2	2	0	2	0	0	1	2	2	1	0
PBS / Infected	5	50	2	2	1	1	0	1	2	0	0	2	2	1	0
PBS / Infected	5	30	1	2	1	1	0	1	1	0	0	2	1	1	0
PBS / Infected - very diseased animal	2	100	0	0	0	0	0	0	1	0	0	0	0	0	0
ensovibep 10mg/kg (0dpi)	3	50	2	1	2	2	1	1	1	0	1	2	4	1	1
ensovibep 10mg/kg (0dpi)	3	40	3	1	2	3	1	2	2	1	2	0	0	1	2
ensovibep 10mg/kg (0dpi)	3	40	3	1	2	2	1	3	1	1	2	1	1	1	0
ensovibep 10mg/kg (0dpi)	3	5	1	0	0	1	1	0	0	0	1	0	0	0	0
ensovibep 10mg/kg (0dpi)	3	5	±	0	0	0	0	0	0	0	0	0	0	0	0
ensovibep 10mg/kg (0dpi)	5	90	3	1	3	3	1	2	2	1	2	3	2	1	0
ensovibep 10mg/kg (0dpi)	5	50	2	1	2	2	1	2	2	0	1	3	1	1	0
ensovibep 10mg/kg (0dpi)	5	15	1	1	1	1	1	1	1	0	1	2	4	0	0
ensovibep 10mg/kg (0dpi)	5	50	3	1	2	2	1	2	2	0	1	2	1	1	0
ensovibep 10mg/kg (0dpi)	5	<5	0	0	0	0	0	0	0	0	0	0	0	0	0
ensovibep 10mg/kg (1dpi)	3	100	1	0	1	1	0	0	0	3	2	0	0	3	0
ensovibep 10mg/kg (1dpi)	3	20	1	1	1	1	1	1	3	0	1	1	0	0	0
ensovibep 10mg/kg (1dpi)	3	<5	0	0	0	0	0	0	0	0	0	0	0	0	0
ensovibep 10mg/kg (1dpi)	3	100	1	0	1	1	1	1	0	2	2	1	0	3	0
ensovibep 10mg/kg (1dpi)	3	80	2	0	2	2	1	2	2	2	1	1	0	2	1
ensovibep 10mg/kg (1dpi)	5	<5	0	0	0	0	0	0	0	0	0	0	0	0	0
ensovibep 10mg/kg (1dpi)	5	20	1	1	1	1	0	1	1	0	0	1	1	1	0
ensovibep 10mg/kg (1dpi)	5	100	2	1	2	2	3	1	1	3	3	0	0	1	0
ensovibep 10mg/kg (1dpi)	5	80	2	1	2	2	1	2	1	1	2	2	1	0	0
ensovibep 10mg/kg (1dpi)	5	<5	1	0	1	1	0	0	0	0	0	1	0	0	0
mAb cocktail 10mg/kg (0dpi)	3	70	3	2	2	2	1	1	2	1	1	1	2	1	2
mAb cocktail 10mg/kg (0dpi)	3	90	2	1	2	2	1	1	1	0	0	1	0	1	1
mAb cocktail 10mg/kg (0dpi)	3	30	1	1	1	1	0	1	1	0	0	1	0	1	0
mAb cocktail 10mg/kg (0dpi)	3	50	2	1	2	2	1	2	2	0	2	1	0	1	1
mAb cocktail 10mg/kg (0dpi)	5	<5	0	0	0	0	0	0	0	0	0	0	0	0	0
mAb cocktail 10mg/kg (0dpi)	5	50	3	1	3	3	1	3	1	1	2	1	1	1	1
mAb cocktail 10mg/kg (0dpi)	5	10	1	1	1	1	0	1	1	0	0	1	0	0	0
mAb cocktail 10mg/kg (0dpi)	5	<5	1	0	1	1	0	0	0	0	0	0	0	0	0
mAb cocktail 10mg/kg (0dpi)	5	30	1	1	1	1	0	1	2	0	0	1	0	1	0
mAb cocktail 10mg/kg (1dpi)	2	50	3	1	3	3	1	3	1	2	3	0	0	1	0
mAb cocktail 10mg/kg (1dpi)	2	90	3	0	3	3	1	3	1	1	2	0	0	2	1
mAb cocktail 10mg/kg (1dpi)	2	90	3	1	3	3	1	1	0	1	1	0	2	3	0
mAb cocktail 10mg/kg (1dpi)	2	90	3	0	3	3	1	2	1	1	3	0	0	3	0
mAb cocktail 10mg/kg (1dpi)	2	20	2	0	2	2	1	2	1	1	1	0	0	2	0
mAb cocktail 10mg/kg (1dpi)	3	60	3	0	3	3	1	2	0	1	3	1	1	2	0
mAb cocktail 10mg/kg (1dpi)	5	40	1	1	1	1	0	1	3	0	0	3	0	1	0
mAb cocktail 10mg/kg (1dpi)	5	80	1	1	1	1	0	1	3	0	1	3	0	1	0
mAb cocktail 10mg/kg (1dpi)	5	70	1	1	1	1	0	0	1	0	1	3	0	1	0
mAb cocktail 10mg/kg (1dpi)	5	10	1	1	0	0	0	0	1	0	0	1	0	1	0
mAb cocktail 10mg/kg (1dpi)	5	10	1	1	1	1	0	0	0	0	0	1	0	1	0
mAb cocktail 10mg/kg (1dpi)	5	<5	1	1	1	1	0	0	2	0	0	1	0	1	0

References

1 Zhou, P. *et al.* A pneumonia outbreak associated with a new coronavirus of probable bat origin. *Nature* **579**, 270-273, doi:10.1038/s41586-020-2012-7 (2020).

2 Shang, J. *et al.* Structural basis of receptor recognition by SARS-CoV-2. *Nature* **581**, 221-224, doi:10.1038/s41586-020-2179-y (2020).

3 Tortorici, M. A. & Veesler, D. Structural insights into coronavirus entry. *Adv Virus Res* **105**, 93-116, doi:10.1016/bs.aivir.2019.08.002 (2019).

4 Letko, M., Marzi, A. & Munster, V. Functional assessment of cell entry and receptor usage for SARS-CoV-2 and other lineage B betacoronaviruses. *Nat Microbiol* **5**, 562-569, doi:10.1038/s41564-020-0688-y (2020).

5 Walls, A. C. *et al.* Structure, Function, and Antigenicity of the SARS-CoV-2 Spike Glycoprotein. *Cell* **181**, 281-292 e286, doi:10.1016/j.cell.2020.02.058 (2020).

6 Walls, A. C. *et al.* Cryo-electron microscopy structure of a coronavirus spike glycoprotein trimer. *Nature* **531**, 114-117, doi:10.1038/nature16988 (2016).

7 Walls, A. C. *et al.* Tectonic conformational changes of a coronavirus spike glycoprotein promote membrane fusion. *Proc Natl Acad Sci U S A* **114**, 11157-11162, doi:10.1073/pnas.1708727114 (2017).

8 Hoffmann, M. *et al.* SARS-CoV-2 Cell Entry Depends on ACE2 and TMPRSS2 and Is Blocked by a Clinically Proven Protease Inhibitor. *Cell* **181**, 271-280 e278, doi:10.1016/j.cell.2020.02.052 (2020).

9 Jun Zhang1, Yongfei Cai1,2†, Tianshu Xiao1,2, Jianming Lu3, Hanqin Peng1, Sarah M. Sterling4,5, Richard M. Walsh Jr.4,5, Sophia Rits-Volloch1, Haisun Zhu6, Alec N. Woosley6, Wei Yang6, Piotr Sliz1,2,5, Bing Chen1,2*. Structural impact on SARS SoV-2 spike protein by D614G substitution. *Science* (2021).

10 Garcia-Beltran, W. F. *et al.* Multiple SARS-CoV-2 variants escape neutralization by vaccine-induced humoral immunity. *Cell* **184**, 2372-2383 e2379, doi:10.1016/j.cell.2021.03.013 (2021).

11 Greaney, A. J. *et al.* Complete Mapping of Mutations to the SARS-CoV-2 Spike Receptor-Binding Domain that Escape Antibody Recognition. *Cell host & microbe* **29**, 44-57.e49, doi:10.1016/j.chom.2020.11.007 (2021).

12 Lusvarghi, S. *et al.* Key substitutions in the spike protein of SARS-CoV-2 variants can predict resistance to monoclonal antibodies, but other substitutions can modify the effects. *bioRxiv*, 2021.2007.2016.452748, doi:10.1101/2021.07.16.452748 (2021).

13 Starr, T. N. *et al.* Deep Mutational Scanning of SARS-CoV-2 Receptor Binding Domain Reveals Constraints on Folding and ACE2 Binding. *Cell* **182**, 1295-1310.e1220, doi:10.1016/j.cell.2020.08.012 (2020).

14 Thomson, E. C. *et al.* Circulating SARS-CoV-2 spike N439K variants maintain fitness while evading antibody-mediated immunity. *Cell* **184**, 1171-1187.e1120, doi:10.1016/j.cell.2021.01.037 (2021).

15 Wang, P. *et al.* Increased Resistance of SARS-CoV-2 Variants B.1.351 and B.1.1.7 to Antibody Neutralization. *bioRxiv*, doi:10.1101/2021.01.25.428137 (2021).

16 Yi, C. *et al.* Key residues of the receptor binding motif in the spike protein of SARS-CoV-2 that interact with ACE2 and neutralizing antibodies. *Cell Mol Immunol* **17**, 621-630, doi:10.1038/s41423-020-0458-z (2020).

17 Liu, Z. *et al.* Identification of SARS-CoV-2 spike mutations that attenuate monoclonal and serum antibody neutralization. *Cell host & microbe* **29**, 477-488.e474, doi:10.1016/j.chom.2021.01.014 (2021).

18 Zhou, D. *et al.* Evidence of escape of SARS-CoV-2 variant B.1.351 from natural and vaccine-induced sera. *Cell* **184**, 2348-2361.e2346, doi:https://doi.org/10.1016/j.cell.2021.02.037 (2021).

19 Gobeil, S. M.-C. *et al.* Effect of natural mutations of SARS-CoV-2 on spike structure, conformation, and antigenicity. *Science* **373**, eabi6226, doi:doi:10.1126/science.abi6226 (2021).

20 Tegally, H. *et al.* Emergence and rapid spread of a new severe acute respiratory syndrome-related coronavirus 2 (SARS-CoV-2) lineage with multiple spike mutations in South Africa. *medRxiv*, doi:10.1101/2020.12.21.20248640 (2020).

21 Voloch, C. M. *et al.* Novel circulating lineage of SARS-CoV-2 in the state of Rio de Janeiro Brazil originated from B.1.1.28 lineage. *medRxiv*, doi:10.1101/2020.12.23.20248598 (2020).

22 Cele, S. *et al.* SARS-CoV-2 Omicron has extensive but incomplete escape of Pfizer BNT162b2 elicited neutralization and requires ACE2 for infection. *medRxiv*, 2021.2012.2008.21267417, doi:10.1101/2021.12.08.21267417 (2021).

23 Thomson, E. C. *et al.* The circulating SARS-CoV-2 spike variant N439K maintains fitness while evading antibody-mediated immunity. *bioRxiv*, doi:10.1101/2020.11.04.355842 (2020).

24 Laffeber, C., de Koning, K., Kanaar, R. & Lebbink, J. H. G. Experimental Evidence for Enhanced Receptor Binding by Rapidly Spreading SARS-CoV-2 Variants. *Journal of Molecular Biology* **433**, 167058, doi:10.1016/j.jmb.2021.167058 (2021).
25 Planas, D. *et al.* Reduced sensitivity of SARS-CoV-2 variant Delta to antibody neutralization. *Nature* **596**, 276-280, doi:10.1038/s41586-021-03777-9 (2021).
26 Ledford, H. The race to make COVID antibody therapies cheaper and more potent. *Nature* **587**, 18, doi:10.1038/d41586-020-02965-3 (2020).
27 Baum, A. *et al.* Antibody cocktail to SARS-CoV-2 spike protein prevents rapid mutational escape seen with individual antibodies. *Science* **369**, 1014-1018, doi:10.1126/science.abd0831 (2020).
28 Copin, R. *et al.* The monoclonal antibody combination REGEN-COV protects against SARS-CoV-2 mutational escape in preclinical and human studies. *Cell* **184**, 3949-3961.e3911, doi:10.1016/j.cell.2021.06.002 (2021).
29 Ku, Z. *et al.* Molecular determinants and mechanism for antibody cocktail preventing SARS-CoV-2 escape. *Nat Commun* **12**, 469, doi:10.1038/s41467-020-20789-7 (2021).
30 Binz, H. K. *et al.* High-affinity binders selected from designed ankyrin repeat protein libraries. *Nat Biotechnol* **22**, 575-582, doi:10.1038/nbt962 (2004).
31 Walser, M. *et al.* Highly potent anti-SARS-CoV-2 multivalent DARPin therapeutic candidates. *bioRxiv* (2020).
32 Stumpp, M. T., Dawson, K. M. & Binz, H. K. Beyond Antibodies: The DARPin((R)) Drug Platform. *BioDrugs* **34**, 423-433, doi:10.1007/s40259-020-00429-8 (2020).
33 Binz, H. K. *et al.* Design and characterization of MP0250, a tri-specific anti-HGF/anti-VEGF DARPin(R) drug candidate. *MAbs* **9**, 1262-1269, doi:10.1080/19420862.2017.1305529 (2017).
34 Fiedler, U. *et al.* MP0250, a VEGF and HGF neutralizing DARPin((R)) molecule shows high anti-tumor efficacy in mouse xenograft and patient-derived tumor models. *Oncotarget* **8**, 98371-98383, doi:10.18632/oncotarget.21738 (2017).
35 Steiner, D. *et al.* Half-life extension using serum albumin-binding DARPin(R) domains. *Protein Eng Des Sel* **30**, 583-591, doi:10.1093/protein/gzx022 (2017).
36 Copin, R. *et al.* In vitro and in vivo preclinical studies predict REGEN-COV protection against emergence of viral escape in humans. *bioRxiv*, doi:10.1101/2021.03.10.434834v3 (2021).
37 Cathcart, A. *et al.* The dual function monoclonal antibodies VIR-7831 and VIR-7832 demonstrate potent in vitro and in vivo activity against SARS-CoV-2. *bioRxiv*, doi:10.1101/2021.03.09.434607v1 (2021).
38 Trimpert, J. *et al.* The Roborovski Dwarf Hamster Is A Highly Susceptible Model for a Rapid and Fatal Course of SARS-CoV-2 Infection. *Cell reports* **33**, 108488, doi:10.1016/j.celrep.2020.108488 (2020).
39 Walls, A. C. *et al.* Unexpected Receptor Functional Mimicry Elucidates Activation of Coronavirus Fusion. *Cell* **176**, 1026-1039 e1015, doi:10.1016/j.cell.2018.12.028 (2019).
40 Corti, D., Purcell, L. A., Snell, G. & Veesler, D. Tackling COVID-19 with neutralizing monoclonal antibodies. *Cell* **184**, 3086-3108, doi:10.1016/j.cell.2021.05.005 (2021).
41 Falsey, A. R. *et al.* SARS-CoV-2 Neutralization with BNT162b2 Vaccine Dose 3. *N Engl J Med*, doi:10.1056/NEJMc2113468 (2021).
42 Hoffmann, M. *et al.* SARS-CoV-2 variants B.1.351 and P.1 escape from neutralizing antibodies. *Cell* **184**, 2384-2393.e2312, doi:10.1016/j.cell.2021.03.036 (2021).
43 Pulliam, J. R. C. *et al.* Increased risk of SARS-CoV-2 reinfection associated with emergence of the Omicron variant in South Africa. *medRxiv*, 2021.2011.2011.21266068, doi:10.1101/2021.11.11.21266068 (2021).
44 Casalino, L. *et al.* Beyond Shielding: The Roles of Glycans in the SARS-CoV-2 Spike Protein. *ACS Cent Sci* **6**, 1722-1734, doi:10.1021/acscentsci.0c01056 (2020).
45 Andreano, E. *et al.* SARS-CoV-2 escape in vitro from a highly neutralizing COVID-19 convalescent plasma. *bioRxiv*, doi:10.1101/2020.12.28.424451 (2020).
46 Osterrieder, N. *et al.* Age-Dependent Progression of SARS-CoV-2 Infection in Syrian Hamsters. *Viruses* **12**, doi:10.3390/v12070779 (2020).
47 Nouailles, G. *et al.* Temporal omics analysis in Syrian hamsters unravel cellular effector responses to moderate COVID-19. *Nat Commun* **12**, 4869, doi:10.1038/s41467-021-25030-7 (2021).
48 Kumari, P. *et al.* Neuroinvasion and Encephalitis Following Intranasal Inoculation of SARS-CoV-2 in K18-hACE2 Mice. *Viruses* **13**, doi:10.3390/v13010132 (2021).
49 Schoof, M. *et al.* An ultrapotent synthetic nanobody neutralizes SARS-CoV-2 by stabilizing inactive Spike. *Science* **370**, 1473-1479, doi:10.1126/science.abe3255 (2020).

50 Cao, L. *et al.* De novo design of picomolar SARS-CoV-2 miniprotein inhibitors. *Science* **370**, 426-431, doi:10.1126/science.abd9909 (2020).
51 Linsky, T. W. *et al.* De novo design of potent and resilient hACE2 decoys to neutralize SARS-CoV-2. *Science* **370**, 1208-1214, doi:10.1126/science.abe0075 (2020).
52 Walter, J. D., Hutter, C. A. J., Garaeva, A. A., Scherer, M. & Zimmermann, I. Highly potent bispecific sybodies neutralize SARS-CoV-2. *bioRxiv* (2020).
53 Hunt, A. C. *et al.* Multivalent designed proteins protect against SARS-CoV-2 variants of concern. *bioRxiv*, doi:10.1101/2021.07.07.451375 (2021).
54 Jones, B. E. *et al.* LY-CoV555, a rapidly isolated potent neutralizing antibody, provides protection in a non-human primate model of SARS-CoV-2 infection. *bioRxiv*, doi:10.1101/2020.09.30.318972 (2020).
55 Pinto, D. *et al.* Cross-neutralization of SARS-CoV-2 by a human monoclonal SARS-CoV antibody. *Nature* **583**, 290-295, doi:10.1038/s41586-020-2349-y (2020).
56 Shi, R. *et al.* A human neutralizing antibody targets the receptor-binding site of SARS-CoV-2. *Nature* **584**, 120-124, doi:10.1038/s41586-020-2381-y (2020).
57 Starr, T. N. *et al.* Deep Mutational Scanning of SARS-CoV-2 Receptor Binding Domain Reveals Constraints on Folding and ACE2 Binding. *Cell* **182**, 1295-1310 e1220, doi:10.1016/j.cell.2020.08.012 (2020).
58 Zahradnik, J. *et al.* SARS-CoV-2 RBD in vitro evolution follows contagious mutation spread, yet generates an able infection inhibitor. *bioRxiv*, doi:10.1101/2021.01.06.425392v3 (2021).
59 Cao, Y. *et al.* B.1.1.529 escapes the majority of SARS-CoV-2 neutralizing antibodies of diverse epitopes. *bioRxiv*, 2021.2012.2007.470392, doi:10.1101/2021.12.07.470392 (2021).
60 Zivanov, J. *et al.* New tools for automated high-resolution cryo-EM structure determination in RELION-3. *Elife* **7**, doi:10.7554/eLife.42166 (2018).
61 Zheng, S. Q. *et al.* MotionCor2: anisotropic correction of beam-induced motion for improved cryo-electron microscopy. *Nat Methods* **14**, 331-332, doi:10.1038/nmeth.4193 (2017).
62 Zhang, K. Gctf: Real-time CTF determination and correction. *J Struct Biol* **193**, 1-12, doi:10.1016/j.jsb.2015.11.003 (2016).
63 Pettersen, E. F. *et al.* UCSF Chimera--a visualization system for exploratory research and analysis. *J Comput Chem* **25**, 1605-1612, doi:10.1002/jcc.20084 (2004).
64 Wrapp, D. *et al.* Cryo-EM structure of the 2019-nCoV spike in the prefusion conformation. *Science* **367**, 1260-1263, doi:10.1126/science.abb2507 (2020).
65 Sanchez-Garcia, R. *et al.* DeepEMhancer: a deep learning solution for cryo-EM volume post-processing. *bioRxiv*, doi:10.1101/2020.06.12.148296 (2020).
66 Cianfrocco, M. A., Wong, M., Youn, C. & Wagner, R. in *The Practice and Experience in Advanced Research Computing* (New Orleans, LA 2017).
67 Chaudhury, S. *et al.* Benchmarking and analysis of protein docking performance in Rosetta v3.2. *PLoS One* **6**, e22477, doi:10.1371/journal.pone.0022477 (2011).
68 Huang, P. S. *et al.* RosettaRemodel: a generalized framework for flexible backbone protein design. *PLoS One* **6**, e24109, doi:10.1371/journal.pone.0024109 (2011).
69 Leaver-Fay, A. *et al.* ROSETTA3: an object-oriented software suite for the simulation and design of macromolecules. *Methods Enzymol* **487**, 545-574, doi:10.1016/B978-0-12-381270-4.00019-6 (2011).
70 Laskowski, R. A. & Swindells, M. B. LigPlot+: multiple ligand-protein interaction diagrams for drug discovery. *J Chem Inf Model* **51**, 2778-2786, doi:10.1021/ci200227u (2011).
71 Goddard, T. D. *et al.* UCSF ChimeraX: Meeting modern challenges in visualization and analysis. *Protein Sci* **27**, 14-25, doi:10.1002/pro.3235 (2018).
72 Berger Rentsch, M. & Zimmer, G. A vesicular stomatitis virus replicon-based bioassay for the rapid and sensitive determination of multi-species type I interferon. *PLoS One* **6**, e25858, doi:10.1371/journal.pone.0025858 (2011).
73 Torriani, G. *et al.* Macropinocytosis contributes to hantavirus entry into human airway epithelial cells. *Virology* **531**, 57-68, doi:10.1016/j.virol.2019.02.013 (2019).
74 Torriani, G. *et al.* Identification of Clotrimazole Derivatives as Specific Inhibitors of Arenavirus Fusion. *J Virol* **93**, doi:10.1128/JVI.01744-18 (2019).
75 Matsuyama, S. *et al.* Enhanced isolation of SARS-CoV-2 by TMPRSS2-expressing cells. *Proc Natl Acad Sci U S A* **117**, 7001-7003, doi:10.1073/pnas.2002589117 (2020).
76 Nao, N. *et al.* Consensus and variations in cell line specificity among human metapneumovirus strains. *PLoS One* **14**, e0215822, doi:10.1371/journal.pone.0215822 (2019).

77 Neerukonda, S. N. *et al.* Establishment of a well-characterized SARS-CoV-2 lentiviral pseudovirus neutralization assay using 293T cells with stable expression of ACE2 and TMPRSS2. *PLoS One* **16**, e0248348, doi:10.1371/journal.pone.0248348 (2021).
78 Wollscheid, B. *et al.* Mass-spectrometric identification and relative quantification of N-linked cell surface glycoproteins. *Nat Biotechnol* **27**, 378-386, doi:10.1038/nbt.1532 (2009).
79 Li, H. *et al.* The Sequence Alignment/Map format and SAMtools. *Bioinformatics* **25**, 2078-2079, doi:10.1093/bioinformatics/btp352 (2009).
80 Bolger, A. M., Lohse, M. & Usadel, B. Trimmomatic: a flexible trimmer for Illumina sequence data. *Bioinformatics* **30**, 2114-2120, doi:10.1093/bioinformatics/btu170 (2014).
81 Li, H. & Durbin, R. Fast and accurate short read alignment with Burrows-Wheeler transform. *Bioinformatics* **25**, 1754-1760, doi:10.1093/bioinformatics/btp324 (2009).
82 Wilm, A. *et al.* LoFreq: a sequence-quality aware, ultra-sensitive variant caller for uncovering cell-population heterogeneity from high-throughput sequencing datasets. *Nucleic Acids Res* **40**, 11189-11201, doi:10.1093/nar/gks918 (2012).
83 Cingolani, P. *et al.* A program for annotating and predicting the effects of single nucleotide polymorphisms, SnpEff: SNPs in the genome of Drosophila melanogaster strain w1118; iso-2; iso-3. *Fly (Austin)* **6**, 80-92, doi:10.4161/fly.19695 (2012).
84 Gu, Z., Eils, R. & Schlesner, M. Complex heatmaps reveal patterns and correlations in multidimensional genomic data. *Bioinformatics* **32**, 2847-2849, doi:10.1093/bioinformatics/btw313 (2016).
85 Copin, R. *et al.* In vitro and in vivo preclinical studies predict REGEN-COV protection against emergence of viral escape in humans. doi:10.1101/2021.03.10.434834 (2021).
86 Corman, V. M. *et al.* Detection of 2019 novel coronavirus (2019-nCoV) by real-time RT-PCR. *Euro Surveill* **25**, doi:10.2807/1560-7917.ES.2020.25.3.2000045 (2020).
87 Gruber, A. D. *et al.* Standardization of Reporting Criteria for Lung Pathology in SARS-CoV-2-infected Hamsters: What Matters? *Am J Respir Cell Mol Biol* **63**, 856-859, doi:10.1165/rcmb.2020-0280LE (2020).
88 Danecek, P. *et al.* Twelve years of SAMtools and BCFtools. *GigaScience* **10**, doi:10.1093/gigascience/giab008 (2021).
89 Robinson, J. T. *et al.* Integrative genomics viewer. *Nat Biotechnol* **29**, 24-26, doi:10.1038/nbt.1754 (2011).
90 Duvaud, S. *et al.* Expasy, the Swiss Bioinformatics Resource Portal, as designed by its users. *Nucleic Acids Res* **49**, W216-w227, doi:10.1093/nar/gkab225 (2021).
91 Choi, Y., Sims, G. E., Murphy, S., Miller, J. R. & Chan, A. P. Predicting the functional effect of amino acid substitutions and indels. *PLoS One* **7**, e46688, doi:10.1371/journal.pone.0046688 (2012).
92 Choi, Y. in *Proceedings of the ACM Conference on Bioinformatics, Computational Biology and Biomedicine* 414–417 (Association for Computing Machinery, Orlando, Florida, 2012).
93 Sim, N. L. *et al.* SIFT web server: predicting effects of amino acid substitutions on proteins. *Nucleic Acids Res* **40**, W452-457, doi:10.1093/nar/gks539 (2012).
94 Friedrich, M. *et al.* Preclinical characterization of AMG 330, a CD3/CD33-bispecific T-cell-engaging antibody with potential for treatment of acute myelogenous leukemia. *Mol Cancer Ther* **13**, 1549-1557, doi:10.1158/1535-7163.MCT-13-0956 (2014).